Doctoral Dissertations   Student Theses and Dissertations

Fall 2018

Electrodeposited epitaxial cobalt oxides and copper metal

Caleb M. Hull

Recommended Citation

Hull, Caleb M., "Electrodeposited epitaxial cobalt oxides and copper metal" (2018). *Doctoral Dissertations*. 2721.

https://scholarsmine.mst.edu/doctoral_dissertations/2721

ELECTRODEPOSITED EPITAXIAL COBALT OXIDES AND COPPER METAL

by

CALEB MICHAEL HULL

A DISSERTATION

Presented to the Faculty of the Graduate School of the

MISSOURI UNIVERSITY OF SCIENCE AND TECHNOLOGY

In Partial Fulfillment of the Requirements for the Degree

DOCTOR OF PHILOSOPHY

in

CHEMISTRY

2018

Approved by:

Jay A. Switzer, Advisor
Amitava Choudhury
Nicholas Leventis
Jeffrey G. Winiarz
Michael S. Moats

PUBLICATION DISSERTATION OPTION

This dissertation contains the following three articles published in peer-reviewed journals as well as an original introduction and conclusion. Paper I (pages 17-30) was published in *Chemistry of Materials* 25(9): 1922-1926 (2013). Paper II (pages 31-51) was published in *Journal of Materials Research,* 31(21): 3324-3331 (2016). Paper III (pages 52-82) has been accepted for publication in *ACS Applied Materials & Interfaces.*

ABSTRACT

Electrochemical deposition methods are presented for the deposition of $Co(OH)_2$ and Cu metal. Paper I shows the deposition of β-$Co(OH)_2$ on Ti through electrochemical reduction of $[Co(en)_3]^{3+}$ to $[Co(en)_3]^{2+}$ in 2M NaOH. The catalytic properties of the deposited $Co(OH)_2$ towards water oxidation is found comparable to Co_3O_4, with the surface of the $Co(OH)_2$ converting to CoOOH during the reaction. Paper II gives the conditions suitable for epitaxial growth of $Co(OH)_2$ on Au(100), Au(110), and Au(111) following the same reduction mechanism as described in Paper I. The epitaxial films are converted to CoOOH electrochemically or to Co_3O_4 thermally, each retaining epitaxy to the Au substrate even through drastic structure changes. Epitaxial CoOOH and Co_3O_4 develop pores and cracks during conversion leading to an increase in the surface area with respect to the initially deposited $Co(OH)_2$ film. Paper III gives conditions for the deposition of epitaxial Cu(100) films on Si(100). This represents only the second metal in the literature to be electrodeposited epitaxially on Si. Cu films are deposited from a dilute pH 3 $CuSO_4$ electrolyte using a two potential step nucleation and growth method. Nucleation occurs at -1.5 $V_{Ag/AgCl}$, a potential negative of the Si oxidation potential, keeping the Si surface reduced and enabling epitaxial nuclei to form. The nuclei are grown at -0.5 $V_{Ag/AgCl}$, a potential positive of the Si oxidation potential, resulting in the concurrent undergrowth of SiO_x between the Cu film and Si substrate. Chemical etching of the SiO_x with 5% HF allows the Cu film to be separated from the Si substrate yielding a freestanding nanometer thick Cu single-crystal-like foil. Epitaxial Cu films and foils are potentially useful ordered substrates for integrated circuits or flexible electronics.

ACKNOWLEDGMENTS

TABLE OF CONTENTS

LIST OF ILLUSTRATIONS

LIST OF TABLES

1. INTRODUCTION

1.1 INORGANIC MATERIAL SYNTHESIS

Material synthesis has been an ever-present part of technological advancement. Entire archeological ages have been characterized by a single material, whose synthesis was the epoch for that age (e.g., bronze age, iron age). Although a single material may never encapsulate our current age, materials such as aluminum, silicon, and plastic have caused an explosion in new technology and goods that are daily a part of our lives. To continue our technological advance, new materials, and methods to incorporate these materials must continue to be developed. While the term material synthesis could, in theory, be applicable to any form of matter, it has become analogous to the production of an element, compound, or composite which is in the solid-state.

Materials are typically classified as either organic or inorganic with polymeric materials typically being organic, while metals and ceramics are typically inorganic. In inorganic material synthesis the traditional methods of production utilize high temperatures. Metals are refined through pyrometallurgical routes involving temperatures above the melting point of the metal,[1] while ceramics are formed by burning in air or solid-state reactions with temperatures often near or above 1000 °C.[2-3] These traditional high temperature methods are robust, and well suited for production of bulk materials, but are not particularly useful for the generation of thin films or coatings on technologically relevant substrates such as plastics or silicon.

In contrast to the traditional synthesis methods, electrodeposition is a low temperature material synthesis technique, perfectly suited for thin film growth.

Electrodeposition uses electricity to oxidize or reduce a solute. Typically the solvent is water, while the solute is a solvated or complexed metal ion. A conductive substrate is used as an electrode at which the relevant reduction or oxidation reaction occurs. Due to the use of an applied potential to drive the reaction, electrodeposition gives uniform coverage across the entire conductive surface, even when complex shapes are involved.[4] This is unique when compared to commonly utilized low temperature vacuum techniques of thermal evaporation, sputtering and molecular beam epitaxy which requires line-of-sight, or compared to sol-gel processes which rely on spin-coating on flat surfaces to achieve thin films.

Typical stratagem for the electrodeposition of both metals and ceramics, along with examples, will be described beginning with metal deposition. Metals have been electrodeposited for over a century, being employed in the industrial production of Pb, Cu, Zn, and Au, among others. Metals are typically deposited cathodically from acidic electrolytes containing a metal salt or complex. The relevant electrochemical reduction is shown by Equation 1.

$$M^{n+}(aq) + ne^- \rightarrow M^0(s) \tag{1}$$

This equation shows that for any metal ion (M^{n+}), the number of electrons (n) required for reduction is equal to the oxidation state of the metal ion (n+). Thus for Cu^0 to be deposited from a $CuSO_4$ electrolyte, two electrons must be supplied as shown in Equation 2.

$$Cu^{2+} + 2e^- \rightarrow Cu^0 \qquad E^0 = 0.34\,V \tag{2}$$
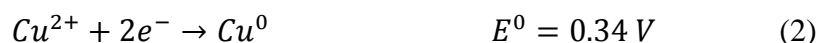
This principle allows the amount of material deposited to be calculated by measuring the number of electrons supplied. The quantitative relationship between charge passed and

mass of material deposited is called Faraday's Law of electrolysis (Equation 3), where

m is the mass of the material, Q is the charge passed, F is Faraday's constant, M is the

molecular weight of the material, and z is the number of electrons transferred.

$$m = \left(\frac{Q}{F}\right)\left(\frac{M}{z}\right) \tag{3}$$

However, this law holds true only if no other reactions are occurring at the electrode.

Reactions which occur simultaneously with the desired reaction are referred to as

parasitic reactions as they draw electrons away from formation of the desired product.

Parasitic reactions are primarily mitigated through electrode potential and solution

purification. Considering an acidic $CuSO_4$ electrolyte, there are three reductions which

are possible, Cu^{2+} to Cu^0, H^+ to H_2, and H_2O to H_2 and OH^-. (Table 1.1)

Table 1.1. Electrochemical Reductions for an Acidic $CuSO_4$ Electrolyte

Half Reaction	Standard Reduction Potential
$Cu^{2+} + 2e^- \rightarrow Cu^0$	0.304 V
$2H^+ + 2e^- \rightarrow H_2$	0.0000 V
$2H_2O + 2e^- \rightarrow H_2 + 2OH^-$	-0.8277 V

The desired reaction, Cu deposition, can be isolated from the two parasitic

hydrogen evolution reactions by depositing in the potential window above proton

reduction and below Cu^{2+} reduction (0 V to 0.304 V). If Cu is deposited at an electrode

potential within this window, it should occur with 100% Faradaic efficiency, *i.e.* follow

Faraday's Law. However, experimentally the reaction progresses at less than 100%,

even when sitting in this thermodynamically isolated region. This is due to impurities in

the solution which have standard reduction potentials greater than the standard reduction

potential of Cu^{2+}. Common impurities are Fe^{3+} and dissolved oxygen. As can be seen in

Table 1.2, both have reduction potentials which are more positive to Cu reduction. Thus

both reactions are thermodynamically permissible under all potentials for which Cu

deposition occurs. Therefore, these parasitic reactions cannot be controlled by electrode

potential and instead must be mitigated through solution purification.

Table 1.2. Reduction Potentials for Common Impurities in Acidic $CuSO_4$ Electrolytes.

Half Reaction	Standard Reduction Potential
$Fe^{3+} + e^- \rightarrow Fe^{2+}$	0.770 V
$O_2 + 4H^+ + 4e^- \rightarrow 2H_2O$	1.229 V
$O_2 + 2H^+ + 2e^- \rightarrow H_2O_2$	0.682 V

While Fe can be chemically precipitated and filtered out, dissolved O_2 is a

persistent impurity coming from the ambient atmosphere. However, by keeping the Cu^{2+}

concentration high compared to the O_2 concentration, high Faradaic efficiencies are

achievable, with efficiencies >92% regularly being achieved industrially.[5] In a typical Cu

electrowinning electrolyte there is approximately 0.5 M Cu^{2+} in solution[6] compared with

1.27 mM O_2 for a pH 1 solution saturated with dissolved oxygen.[7] This represents

roughly 400 times as much Cu^{2+} as oxygen to react, which for an air saturated solution is

closer to 2000 times as much Cu^{2+}. So even though O_2 reduction still occurs, its effects

on overall Faradaic efficiency is slight.

While the electrodeposition of a metal is a completely electrochemical

mechanism, the deposition of ceramics requires a coupled electrochemical-chemical

mechanism. To achieve deposition, two main stratagem exist. Stratagem (i) is similar to

the electrodeposition of metals, where the electrochemical step changes the oxidation

state of the metal.[8-12] Perturbation of the oxidation state creates an unstable metal ion that

reacts with a soluble species in the electrolyte, causing precipitation at the electrode. In

stratagem (ii), instead of perturbing the oxidation state of the metal ion, the pH at the

electrode is perturbed, generally through the electrochemical generation of base. The

change in pH causes the metal ion to be unstable and precipitate, usually as a metal oxide

or hydroxide. Many methods of electrochemical generation of base have been devised,

but commonly employed methods include nitrate reduction,[13-16] oxygen reduction, or

water reduction.[17-20] The half reactions with the standard reduction potential of each is

given in Table 1.3. A sampling of other methods for the electrochemical generation of

base are generation of superoxide,[21] reduction of alcohols,[21] and perchlorate reduction.[16]

Using these two stratagem many different ceramics have been deposited, for instance

TiO_2,[17] CeO_2,[18-19] ZrO_2,[13] RuO_2,[20, 22] IrO_x,[8-9] ZnO,[14-15] PbO_2,[10] $CdSe$,[12] and $Co(OH)_2$.[11]

Table 1.3 Half-Reactions for Electrochemical Generation of Base

Reduction	Standard Reduction Potential
$2H_2O + 2e^- \rightarrow H_2 + 2OH^-$	-0.8277
$NO_3^- + H_2O + 2e^- \rightarrow NO_2^- + 2OH^-$	0.01

Table 1.3 Half-Reactions for Electrochemical Generation of Base (cont.)

$O_2 + 2H_2O + 4e^- \rightarrow 4OH^-$	0.401

1.2 CONVERSION OF ELECTRODEPOSITED FILMS

In addition to being a standalone material synthesis technique, electrodeposition can be coupled with a secondary processing step to convert the deposited material into something else. Such conversions include metals to oxides, hydroxides to oxides, and more subtle changes like type conversion in a semiconductor. Coupling electrodeposition with a secondary processing step increases the breadth of materials which can be produced and scope of their use. Secondary processing steps of thermal conversion and electrochemical conversion are discussed.

1.2.1. Thermal Conversion. Thermal conversion applies the traditional ceramic technique to an electrodeposited film. Thermal conversion covers a wide range of procedures such as oxidation, selenization, sulfidization, doping or alloying, as well as dehydration and decomposition. Conversion is simply accomplished by placing the deposited film in a hot reactive atmosphere. One application of this method is in the production of mixed metal semiconductors useful for photovoltaics. Examples include copper indium gallium selenide,[23] copper zinc tin selenide (CZTSe),[24-25] and methyl ammonium lead iodide.[26] In these examples, a film is deposited followed by thermal conversion to give semiconducting materials having the correct elemental composition. In addition to producing semiconducting materials having the correct bulk elemental composition, thermal processing can be used to supply specific impurity atoms (dopants)

into the material, making the material more useful in a semiconducting device. Dopants

cause a rise in the number of free electrons (negative charge carriers, or n-type dopant) or

holes (positive charge carriers, or p-type dopants) by donating electrons or accepting

electrons from the bulk. Doping causes the Fermi level (chemical potential) of the

semiconductor to change, in addition to increasing the electrical conductivity. Often

electrodeposition methods give just a single type (n or p) material, while deposition of the

opposite type is difficult. For instance, while electrodeposition methods producing p-

type Cu_2O abound, depositions of n-type Cu_2O are few[27-29] and controversial.[30] Similarly

n-type ZnO is commonly electrodeposited, but deposition of p-ZnO is rare.[31-32]

However, type change has been accomplished by subjecting a deposited film to thermal

treatment.[33-36] While the examples given have focused on application of the

electrodeposition-thermal conversion route to produce photovoltaic materials, it has also

been applied to the synthesis of electrochromic materials,[37-38] catalysts,[39-42] and energy

storage materials.[43]

  1.2.2 Electrochemical Conversion. Electrodeposited films can also be

converted by electrochemical means. Conversion is similar to thermal conversion, in that

conversion mechanisms involve oxidation, dehydration, or decomposition. However,

electricity is used to drive the reaction instead of heat. This permits the use of thermally

labile substrates, which may be prohibited by the thermal route. In addition

electrochemical methods allow the formation of metastable materials such as

oxyhydroxides, which would otherwise form oxides under thermal conversion. First row

transition metal oxyhydroxides of FeOOH,[44-47] NiOOH,[48-50] and CoOOH,[51-52] and their

mixtures,[53-55] have garnered much interest as earth abundant catalysts, particularly toward

the water oxidation reaction. While oxyhydroxides can be electrodeposited directly, synthesis through electrodeposition and conversion has been shown to generate morphologies having increased surface area.[11, 52] As compared to traditional processing techniques, which incorporates a powdered catalyst with a binder to achieve adherence to the electrode, [56] the electrochemical route provides an adherent film directly. Thus the electrodeposition and electrochemical conversion route has the potential to produce electrodes and photoelectrodes having higher activity than those produced either traditionally or through electrodeposition alone, by giving increased surface area and better electrical conductivity.

1.3 ELECTRODEPOSITION OF EPITAXIAL FILMS

Another strength of the electrodeposition technique is the ability to tune the crystallographic relationship between the film and the substrate through simple variation of the deposition conditions. Variables such as electrode potential, current density, temperature, pH, and concentration can all be tuned such that epitaxy is achieved. Epitaxy refers to the crystallographic ordering of a film due to the underlying order of the substrate. Thus for epitaxial growth, ordered substrates like Au single crystals or single crystal Si wafers must be used. However, simply using a single crystal substrate does not guarantee the growth of an epitaxial film, as a host of thermodynamic and kinetic mechanisms are involved in film growth. A critical factor in achieving epitaxy is the lattice mismatch between the substrate and the growing film. This mismatch is calculated as a percentage by comparing the difference between the lattice parameter of the film (a_f) with the lattice parameter of the substrate (a_s) following Equation 4.

$$\% \ mismatch = \frac{a_f - a_s}{a_s} * 100 \tag{4}$$

The simplest example is to compare the mismatch for a cubic film on a cubic substrate.

For this case, two film geometries arise allowing the matching of a_f with a_s, a cube on

cube arrangement or a 45° rotation of the film on the substrate. In the cube on cube

arrangement, a_s is directly compared to a_f, while for the 45° rotated film, a coefficient of

√2 should be added to a_f. as depicted in Figure 1.1. For the calculation of percent

mismatch in a 45° rotated film the equation becomes:

$$\% \ mismatch = \frac{\sqrt{2}a_f - a_s}{a_s} * 100 \tag{5}$$
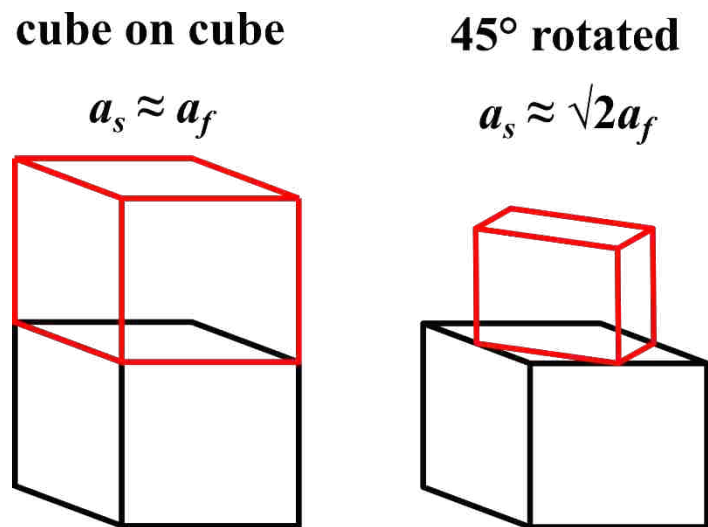
Figure 1.1. 3D depiction of geometric stacking of two cubic materials, one having a cube on cube orientation and the other having a 45° rotation.

In this geometric consideration and calculation of lattice matching a positive value

describes a film which has a lattice larger than the substrate, while a negative value

describes a film having a smaller lattice than the substrate. Coupling the work of Toda[57]

with the Frank-Van der Merwe model of epitaxial growth,[58-59] a critical misfit of -12% and 7% has been calculated.[60] The difference in value for a negative misfit versus a positive misfit arises from the preferential growth of misfit dislocations rather than growing under strain for a film having a positive misfit, while a film having a negative misfit prefers to grow under strain.[60] Performing this calculation for a Cu film ($a_f =$ 3.6150 Å) deposited on a Si substrate ($a_s = 5.4309$ Å), the cube on cube arrangement gives a mismatch is -33.43%, but the 45° rotated arrangement reduces the mismatch to -5.86%. This brings the mismatch below the critical misfit of -12%,[60] and is indeed how the film grows experimentally.[61-68] The interface model showing the lattice mismatch is given in Figure 1.2.
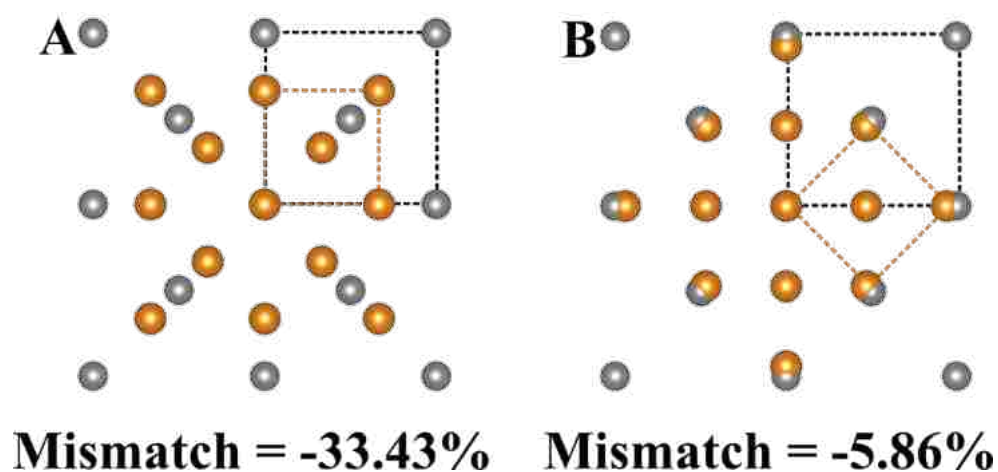
Figure 1.2. Interface models of Cu (100) (orange, $a_f = 3.6150$ Å) on Si (100) (grey, $a_s = 5.4309$ Å) with Cu rotated in plane by 0° (A) and 45° (B)

Experimentally, epitaxial films have been deposited on substrates having different crystal structures between film and substrate,[69-70] or have a percent mismatch larger than the critical misfit,[71-73] for instance Al(111) on Si(111).[74] To understand and explain how

these films grow epitaxially, the coincidence site lattice (CSL) has been used.[74-75] The idea of the CSL is to expand the original geometric lattice matching to include more than just a single lattice of film on substrate, rather finding an integral number of film lattices which match to an integral number of substrate lattices. This treatment seeks to minimize the mismatch using the smallest CSL possible. Epitaxial films which have been successfully electrodeposited within the Switzer group include $Ag(Ag_3O_4)_2NO_3$,[76] Tl_2O_3,[77] Cu_2O,[78-81] PbS,[82] Fe_3O_4,[83-86] ZnO,[87-89] PbO_2,[90] Prussian blue,[91] SnS,[92] CuO,[93] PbI_2,[26] Bi_2O_3,[94] Au,[95] $Co(OH)_2$,[11] and Cu.

Devices built on, and constructed of, epitaxial films should have higher efficiency compared to polycrystalline based devices just as devices built from single-crystals. This is due to the fact that in both single crystals and epitaxial films there is a lack of grain boundaries, which have increased concentration of defects that act as electron-hole recombination sites. The trend of increased efficiency with increased crystallinity is exemplified in the comparison of highest recorded efficiencies for silicon photovoltaic cells (Table 1.4).[96] In addition to increased device efficiency, epitaxial films are useful in creation of multilayer nanostacks which enable devices to incorporate quantum phenomena.[97-103]

Table 1.4. Photovoltaic Cell Efficiency by Substrate Crystallinity[96]

Substrate Crystallinity	Efficiency
Amorphous Silicon	14.0%
Polycrystalline Silicon	22.3%
Single Crystal Silicon	26.1%

1.3.1. Epitaxial Conversion. Using the before mentioned thermal or electrochemical conversion techniques, an initially deposited epitaxial film can be converted while retaining epitaxy. For instance, epitaxial films of Fe_2O_3, and Bi_2O_3 have both been electrochemically reduced yielding epitaxial films of Fe^{40} and $Bi.$[104] This is fascinating, as a large amount of atomic restructuring occurs concurrently, due to loss of oxygen during reduction. Atomic restructuring is exhibited in the change of crystal structure from a fcc-Fe_3O_4 to bcc Fe and fcc Bi_2O_3 to a rhombohedral Bi. Retention of epitaxy through conversion has also been observed in the oxidation of an epitaxial film of $Co(OH)_2$ to $CoOOH$[11] and similarly in the thermal conversion of $Co(OH)_2$ to $Co_3O_4.$[11]

1.3.2. Epitaxial Films on Silicon. The need for highly ordered substrates in the growth of epitaxial films leads one quickly to the silicon wafer. High quality single-crystal silicon wafers are inexpensive conductive substrates, as they are widely used for integrated circuits in electronic devices. In addition to being inexpensive, the benefits in electron transport gleaned from epitaxy could be immediately applicable to actual electronic devices. Growth of epitaxial films on silicon however, is not a trivial matter. This is in large part due to the reactivity of the silicon surface, prone to oxidation, forming a passivating layer of disordered amorphous SiO_x in air. Rigorous cleaning methods have been developed to produce clean, quasi-stable Si surfaces. Most methods utilize the two step RCA method (also called Standard Clean 1 and 2, or shortened to SC1/SC2 in the literature), which was developed by Werner Kern for Radio Corp of America.[105] The first step in this method removes organic contaminants utilizing an ammonium hydroxide and hydrogen peroxide solution, while the second step removes inorganic contaminants using a hydrochloric acid and hydrogen peroxide solution. After

cleaning, the wafer is then placed in an HF solution to etch and remove the SiO_x. In addition to etching of the SiO_x, HF and NH_4F etches have been shown to produce H terminated Si surfaces which are atomically smooth[106-110] and effective in preventing air oxidation for several days.[111-113] Once the Si is cleaned and H terminated, deposition of epitaxial films has primarily been accomplished through vacuum techniques of molecular beam epitaxy,[114-125] electron beam evaporation,[126-128] thermal evaporation,[129-132] pulsed laser deposition,[133-135] as well as RF magnetron sputtering[122, 136] and DC sputtering.[137-138]

Though few, electrodeposition of epitaxial films directly on Si has been accomplished. Electrodeposition carries an increased challenge compared to vapor deposition because the Si surface, even when H terminated, oxidizes in a much shorter time scale in water than in air.[113, 139-140] Again, oxidation produces a disordered amorphous SiO_x thereby preventing epitaxial growth of the film. Thus, few example of aqueous electrodeposition of epitaxial films on Si are seen in the literature. These examples are Au,[95, 141-142] Cu, and Cu_2O[80, 143-144]. To prevent the oxidation of the Si surface Au and Cu are deposited at a potential more negative than the Si oxidation potential, thereby preventing the disordered SiO_x from forming at the surface and allowing epitaxial deposition to occur.

1.3.3. Epitaxial Lift-Off of Single-Crystal-Like Foils. As has already been discussed, epitaxial films are particularly well suited for advanced electronics. However, the use of ordered single crystal substrates incurs a higher manufacturing cost than a polycrystalline substrate, and the single crystal substrates are typically rigid. Thus the burgeoning field of flexible electronics has largely centered on the use of polycrystalline metal foils and conductively coated plastics as substrates, foregoing the potential benefits

a single crystal or single-crystal-like substrate offers. This being said, efforts have been made to develop methods of producing inexpensive, flexible, ordered substrates. One method which produces single-crystal-like substrates is through thermomechanical rolling of a polycrystalline metal. This has been pioneered by Goyal and co-workers in a patented multi-step process of heating and rolling to produce single-crystal-like Ni and Cu ribbons or so called "rolling assisted biaxially textured substrates".[145-147] In addition to this fairly complex method, a simple electrochemical method has also been developed. In the electrochemical method an epitaxial film is deposited onto a sacrificial layer which is then be etched away to produce freestanding single-crystal-like foils. This process, termed "epitaxial lift-off," involving deposition, etching, and lift-off, can be repeated over and over again using the same single crystal substrate. This was demonstrated by Chason and co-workers when they synthesized a single-crystal-like Ni foils by selectively etching a sacrificial Cu layer away from an epitaxial electrodeposited Ni|Cu|Ni stack.[148] Similarly, Switzer and co-workers have produced Au[149] and Cu single-crystal-like foils through etching of a sacrificial SiO_x layer grown between an epitaxial metal layer and the Si substrate.

1.3.4. Characterization of Epitaxial Films and Single-Crystal-Like Foils.

Crystallographic order is often determined by x-ray diffraction. For powders, a simple symmetric 2θ scan is sufficient for material determination as it gives diffraction peaks and intensities characteristic of a certain material. These peaks positions and intensities can be compared to those which are theoretically calculated based on the materials composition and crystal structure. However, for a thin film or substrate which may be polycrystalline or single crystalline, the symmetric scan is insufficient to fully

characterize the material, because it probes only the planes which are parallel to the sample surface. To determine the orientation and whether a material is textured or single-crystalline, x-ray pole figures are acquired. A pole figure is a stereographic projection which plots the diffraction intensity from a certain atomic plane as a contour plot versus sample tilt (χ) and azimuthal angle (φ). The plane being probed is chosen by fixing the x-ray source and detector to satisfy the respective Bragg angle for that plane. To construct the pole figure a series of tilt (χ) scans is acquired step-wise (typically 0-90°, with 3° step), each scan being collected by rotating the sample from 0-360° azimuthally. Thus a pole figure shows all instances which satisfy the Bragg condition three dimensionally, representing this information on a 2D plot. For instance if a Cu(111) pole figure is to be acquired, the Bragg angle ($2\theta = 43.298°$ for a Cu $K_{\alpha 1}$ x-ray source) is set. Starting at $\chi = 0°$, the sample is rotated from $\varphi = 0$-360°, the scan stored, then the sample is tilted to $\chi = 3°$ and again rotated about φ and recorded. This process is repeated through $\chi = 90°$. For a single crystal, or single-crystal-like substrate, the pole figure would show a distinct spot pattern having a number of spots corresponding to the symmetry of the out-of-plane orientation located at a tilt angle equal to the angle between plane parallel to the surface of the sample and the plane being probed. In the case of a textured sample, this spot pattern would become a ring at the same tilt angle. For a polycrystalline sample a low intensity, noisy plot would be collected as the planes are randomly oriented in-plane and out-of-plane. Example patterns for Cu(111) pole on a Cu(100), Cu(110), and Cu(111) single crystal or textured sample can be seen in Figure 1.3.
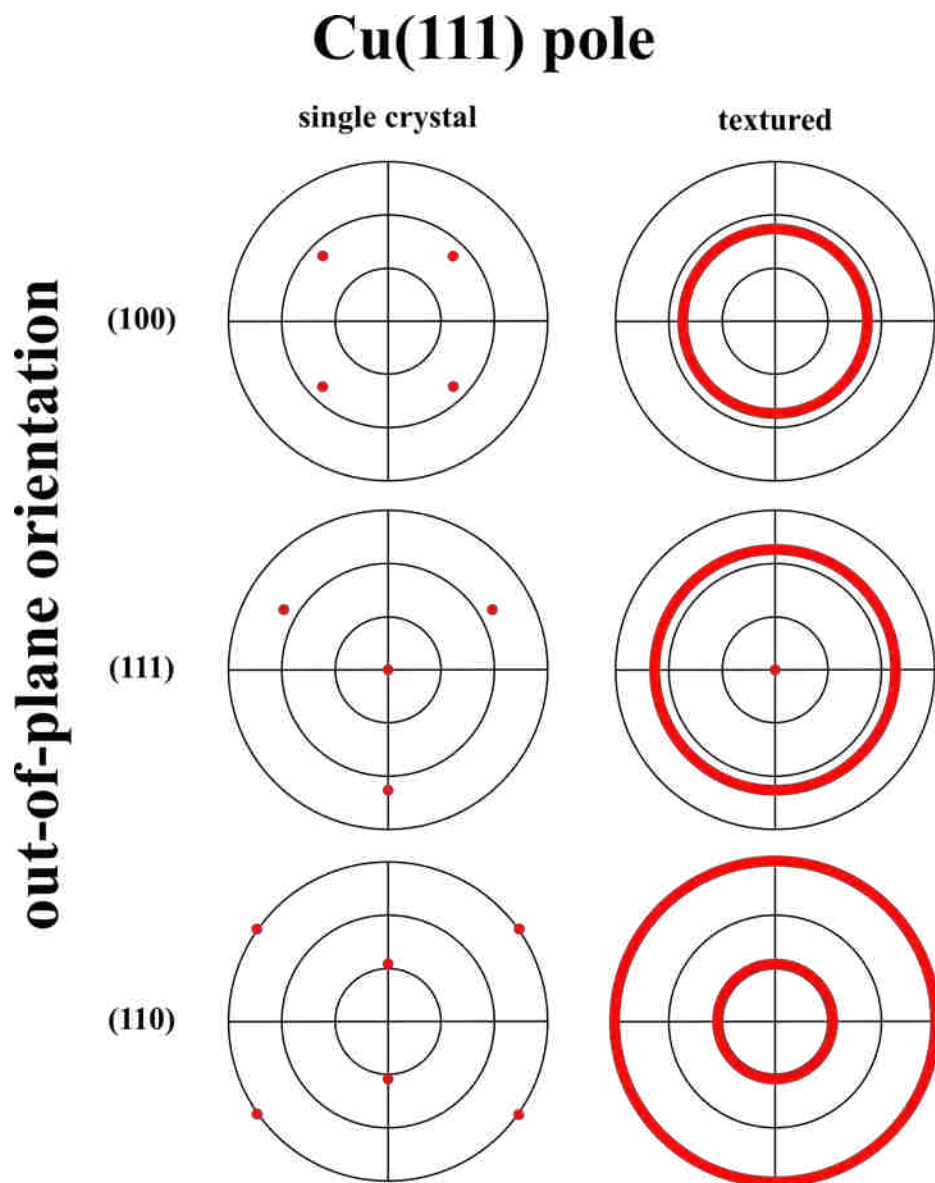
Cu(111) pole

Figure 1.3. Simulated Cu(111) pole figures for single crystal and textured Cu having an out-of-plane orientation of (100), (111), and (110). The concentric grid lines on the pole figures correspond to 30° increments of the tilt angle.

PAPER

I. DEPOSITION OF *β*-Co(OH)$_2$ FILMS BY ELECTROCHEMICAL REDUCTION OF TRIS(ETHYLENEDIAMINE)COBALT(III) IN ALKALINE SOLUTION

Jakub A. Koza, Caleb M. Hull, Ying-Chau Liu, and Jay A. Switzer*

Missouri University of Science and Technology, Department of Chemistry and Graduate Center for Materials Research, Rolla, MO 65409-1170, USA

ABSTRACT

Films of β-Co(OH)$_2$ with a dense microcone morphology are electrodeposited at room temperature by reducing tris(ethylenediamine)cobalt(III) in alkaline solution. The synthesis exploits the fact that the kinetically-inert Co(III) complex of ethylenediamine (en) is 35 orders of magnitude more stable than the kinetically-la2bile Co(II) complex. [Co(en)$_3$]$^{3+}$ is therefore stable in alkaline solution, but [Co(en)$_3$]$^{2+}$ reacts with excess hydroxide ion to produce β-Co(OH)$_2$. The electrodeposited β-Co(OH)$_2$ is an active catalyst for the oxygen evolution reaction. Raman spectroscopy suggests that the surface of β-Co(OH)$_2$ is converted to CoOOH at the potentials at which oxygen evolution occurs.
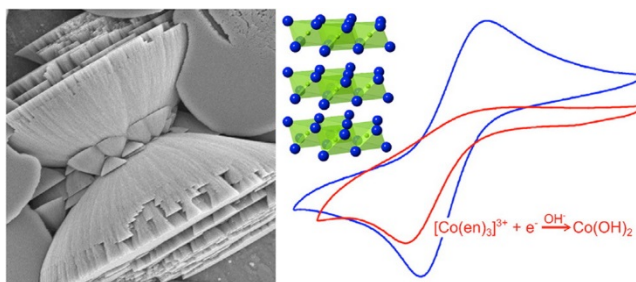
KEYWORDS: Co(OH)$_2$; cobalt hydroxide; electrodeposition; oxygen evolution catalyst; oxygen evolution reaction

1. INTRODUCTION

Cobalt hydroxide, β-Co(OH)$_2$, is a promising material for energy conversion and storage. It is a common additive in Ni-based rechargeable alkaline batteries.[1] Nanoarchitectured Co(OH)$_2$ pseudocapacitors have shown a specific capacity as high as 2800 F g^{-1} without significant deterioration upon cycling.[2] Co(OH)$_2$ is known as an earth-abundant catalyst for the oxygen reduction[3] and hydrogen evolution[4] reactions. It is also an active catalyst for ozone and p-chloronitrobenzene decomposition in water.[5] In addition, Co(OH)$_2$ exhibits the giant reversible magnetocaloric effect, which makes it a promising candidate for low-temperature magnetic refrigeration applications.[6] Co(OH)$_2$ can be oxidized electrochemically[1, 4] to CoOOH, which is an excellent oxygen evolution reaction (OER) catalyst,[4, 7] and it is used in room temperature CO sensors.[8] Several other groups have shown that Co(OH)$_2$ nanoplatelets can be electrodeposited using OH$^-$ that is generated by reduction of nitrate ions[3, 9-11] Here, we introduce a method to electrodeposit crystalline β-Co(OH)$_2$ films. Dense Co(OH)$_2$ microcones are electrodeposited potentiostatically from a solution of 45 mM [Co(en)$_3$]$^{3+}$ (en, ethylenediamine) in 2 M NaOH (pH $\approx$ 14) at room temperature. We also show that the electrodeposited Co(OH)$_2$ is an active OER catalyst.

2. EXPERIMENTAL SECTION

2.1. TRIS(ETHYLENEDIAMINE)COBALT(III) SYNTHESIS

[Co(en)$_3$]Cl$_3$ was synthesized using a literature procedure.[12] One solution was prepared by dissolving 12 g of CoCl$_2$·6H2O in 35 mL of water. Another solution was prepared by dissolving 6 mL of anhydrous ethylenediamine in 25 mL of water, cooled

down to 0 °C, and partially neutralized with 8.5 mL of 6 M HCl. Both solutions were

mixed together, and 10 mL of 30% H_2O_2 was added while stirring the solution. The

solution was boiled until it evaporated to a volume of approximately 60 mL. A volume of

60 mL of 12 M HCl was added, followed by addition of 120 mL of ethanol. The solution

was cooled to about 0 °C, and the precipitate, which is $[Co(en)_3]Cl_3 \cdot 1–3H_2O$, was filtered

and washed with ice-cold ethanol. The final product was dried in air.

2.2 DEPOSITION SOLUTION

The electrolyte used for deposition of $Co(OH)_2$ was prepared by dissolving the

appropriate amount of the as-synthesized $[Co(en)_3]Cl_3$ in 2 M NaOH to form a nominal

45 mM concentration.

2.3 ELECTROCHEMICAL METHODS

The electrodeposition experiments were performed in 125 mL of electrolyte at

room temperature in a standard three-electrode setup using a Brinkmann PGSTAT 30

Autolab potentiostat. The electrolyte was stirred at a rate of 200 rpm with a magnetic

stirrer. The in situ mass changes were monitored with a Stanford Research Systems

QCM200 electrochemical quartz crystal microbalance (EQCM). A Ti, an Au rotating disc

electrode (RDE), and an Au sputtered quartz were used as the working electrodes. A Pt

mesh served as the counter electrode. The Ti and Au-RDE substrates were mechanically

polished, sonicated in acetone, and rinsed with DI water prior to the experiments.

The catalytic properties of the films for the OER were investigated in 1 M KOH

solution at room temperature in a three-electrode cell using a Brinkmann PGSTAT 30

Autolab potentiostat. The deposit served as the working electrode and a Pt grid was the counter electrode. The OER experiments were performed on fresh layers immediately (after rinsing with DI water) after deposition. The potentials were corrected for the IR drop, which was determined by electrochemical impedance spectroscopy. All potentials are referred with respect to the Ag/AgCl/KCl$_{sat}$ reference electrode.

2.4 CHARACTERIZATION

The films were characterized using a high-resolution Philips X-Pert MRD X-ray diffractometer (XRD) with a CuKα$_1$ radiation source (λ = 1.54056 Å). XPS investigations were performed in a Kratos AXIS 165 spectrometer using monochromatic AlKα radiation energy (1486.6 eV).

Raman measurements were carried out using a Horiba Jobin-Yvon LabRam Aramis Microscope with a HeNe laser (λ = 633 nm) as the excitation source with an incident power of about 0.5 mW to minimize sample heating. The morphology of films was determined by means of scanning electron microscopy (SEM; Hitachi S4700 FESEM) and atomic force microscopy (AFM) in the contact mode (Digital Instruments Nanoscope III).

3. RESULTS AND DISCUSSION

We exploit the well-known inorganic chemistry that Co(III) favors nitrogen ligands over oxygen ligands, whereas Co(II) favors oxygen ligands over nitrogen ligands. $[Co(en)_3]^{3+}$ is nearly 35 orders of magnitude more stable than $[Co(en)_3]^{2+}$. The formation constants for $[Co(en)_3]^{3+}$ and $[Co(en)_3]^{2+}$ are $10^{48.69}$ and $10^{13.94}$, respectively.[13] Co(III)

complexes are also substitutionally inert, whereas Co(II) complexes are substitutionally labile in aqueous solution.[14] Hence, $[Co(en)_3]^{3+}$ is stable in an alkaline solution, but $[Co(en)_3]^{2+}$ reacts with excess OH^- to produce $Co(OH)_2$. The formation constant of $Co(OH)_2$ is 1014.96.[15]

Figure 1a shows the cyclic voltammograms (CVs) measured on an Au electrode in the deposition solution (red) and in a solution of 45 mM $[Co(en)_3]^{3+}$ and 0.5 M ethylenediamine of pH 9 (blue). The CV measured in the solution containing excess
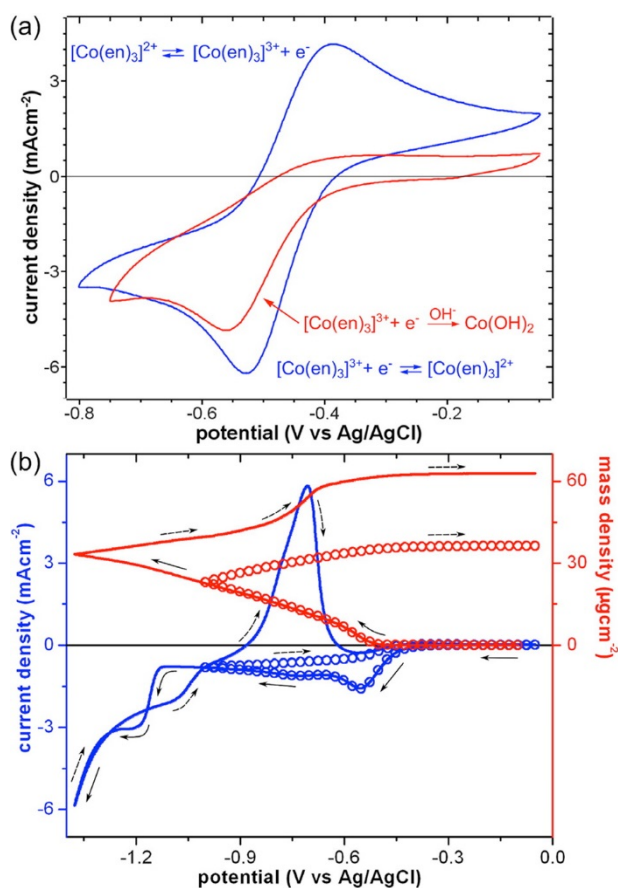
Figure 1. (a) CVs measured at an Au electrode in the $Co(OH)_2$ deposition electrolyte (red) and 45 mM $[Co(en)_3]^{3+}$ and 0.5 M ethylenediamine electrolyte of pH 9 (blue) at 100 mV s^{-1} scan rate. (b) CVs (blue) together with the corresponding mass changes (red) measured at an Au coated quartz crystal microbalance electrode in the deposition solution at 20 mV s^{-1} scan rate. The black arrows indicate the scan direction.

ethylenediamine (blue) shows quasireversible $[Co(en)_3]^{3+/2+}$ oxidation–reduction (eq 1)

with a reduction peak at -0.525 $V_{Ag/AgCl}$ and an oxidation peak at -0.39 $V_{Ag/AgCl}$. In

contrast, the CV obtained in the deposition solution (red), with a large excess of OH^-,

shows irreversible behavior. A reduction peak at -0.55 $V_{Ag/AgCl}$ is observed without the

corresponding oxidation peak. At this potential, the mass also starts to increase (Figure

1b, red), measured with an EQCM, due to the $Co(OH)_2$ formation (eq 2). The deposition

of $Co(OH)_2$ occurs in the potential range of -0.5 to -1.1 $V_{Ag/AgCl}$. At more negative

potentials Co is produced (eq 3), with a second peak in the CV at about -1.2 $V_{Ag/AgCl}$.

$$[Co(en)_3]^{3+} + e^- \rightleftarrows [Co(en)_3]^{2+} \tag{1}$$

$$[Co(en)_3]^{2+} + 2OH^- \rightleftarrows Co(OH)_2 \downarrow +3en \tag{2}$$

$$[Co(en)_3]^{3+} + 3e^- \rightarrow Co + 3en \tag{3}$$
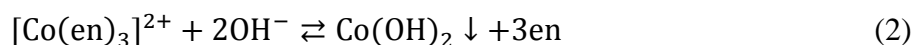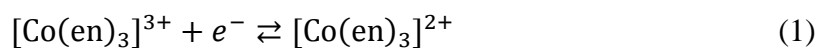
Uniform pink films were deposited potentiostatically at -1 $V_{Ag/AgCl}$ and room

temperature on Ti electrodes. The deposition proceeds with 100% current efficiency

(determined with the EQCM). Figure 2 shows the XRD pattern of the electrodeposited

film. All reflections originating from the film can be assigned as β-$Co(OH)_2$ with the

brucite $Mg(OH)_2$ layered structure with measured lattice parameters of $a = b = 3.179$ Å

and $c = 4.658$ Å in $P\bar{3}m1$ symmetry. The intensity of the (001) peak is higher than that of

the (101), suggesting a preferred [001] growth direction. Figure 3 shows the X-ray

photoemission (XPS) spectra of the as-deposited $Co(OH)_2$ film in the Co2p (a) and O1s

(b) binding energy ranges. The XPS spectrum of the film in the Co2p binding energy

range exhibits five deconvolved peaks at 780.2, 782, 790, 796.3, and 802.3 eV (Figure

3a) which match Co(OH)2.[16, 17] the O1s spectrum (Figure 3b) exhibits the main peak at

531.2 eV, which corresponds to OH bonded to Co(II),(16, 18) and two additional low

intensity peaks at 529.4 and 532.5 eV corresponding to CoO and structural water,

respectively[2, 18] The oxygen to cobalt ratio in the film was 2.05, consistent with

stoichiometric composition.
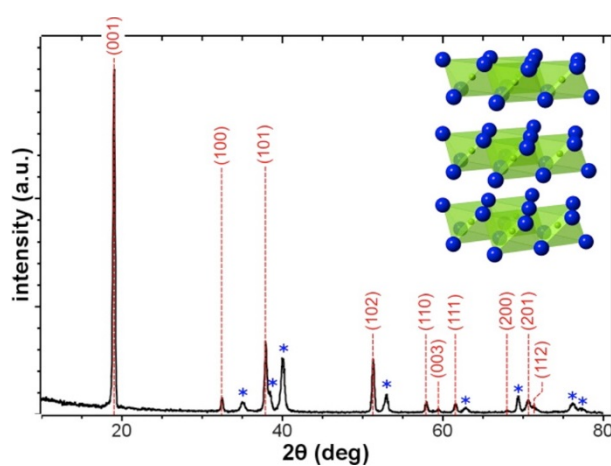
Figure 2. XRD pattern of electrodeposited Co(OH)2. Co(OH)2 reflections are indicated in red (JCPDS no. 30-0443); blue asterisks stand for the Ti substrate. The inset shows the Co(OH)2 structure.
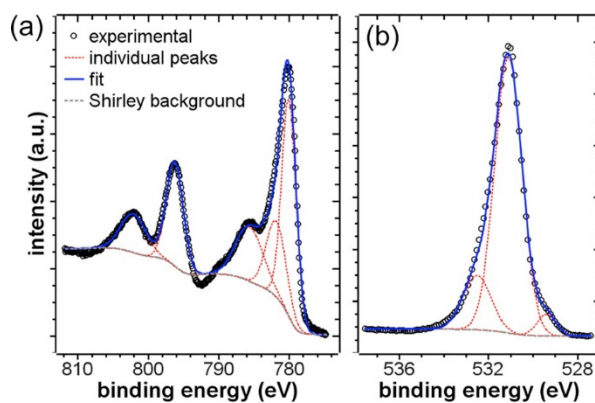
Figure 3. XPS spectra of electrodeposited Co(OH)2: (a) Co2p and (b) O1s binding energy ranges.

Figure 4a,b shows SEM images of the $Co(OH)_2$ film. The film consists of conical grains, which tend to align with the top disk surface parallel to the substrate. This morphology is very different than that of sparse, nanoplatelets electrodeposited via base generation.[3, 9-11] A closer look at the sidewalls of the cones reveals that they grow with an onionskin-like morphology (Figure 4b). The growth of different cone layers terminates at the same height forming a very smooth surface with a roughness of only 1.3 nm, as determined by AFM (Figure 4c).
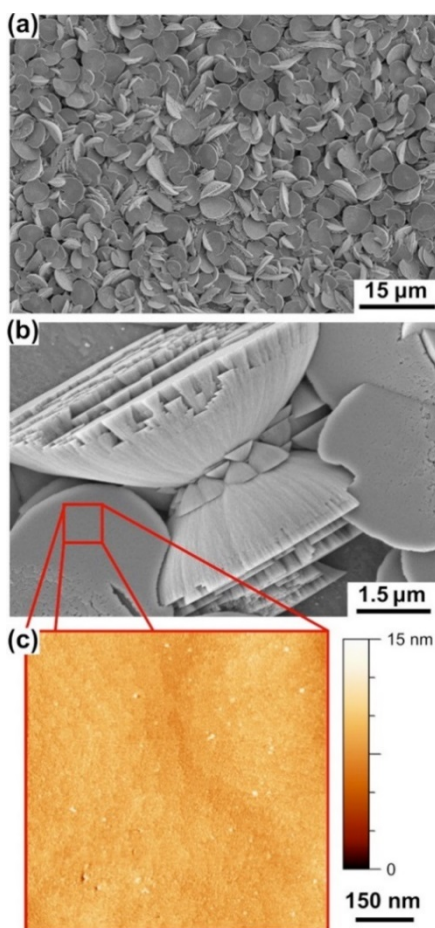
Figure 4. Morphology of $Co(OH)_2$ electrodeposited to a charge density of 0.6 C cm^{-2}: (a,b) SEM images of the film and (c) AFM image of a flat disk surface.

Electrodeposited $Co(OH)_2$ is a potent catalyst for the OER. Linear sweep voltammograms (LSVs) at a scan rate of 1 mV s^{-1} on a Ti electrode (blue) and a $Co(OH)_2$-coated Ti electrode (red) in unstirred 1 M KOH at room temperature are shown in Figure 5. The LSV measured on electrodeposited, crystalline Co_3O_4 film, which is an active OER catalyst,[19] is also shown (black) because the surface chemistry of both materials during OER is similar. From Figure 5 it is apparent that the electrodeposited $Co(OH)_2$ is an active catalyst for the OER. The onset of OER on $Co(OH)_2$ is 0.51 $V_{Ag/AgCl}$ which is about 50 mV higher than that measured on Co_3O_4. However, current densities, based on the geometry of the electrodes, are much higher on the $Co(OH)_2$ film at more positive potentials, possibly due to the roughness of $Co(OH)_2$ compared to the smooth Co_3O_4 film.[19]
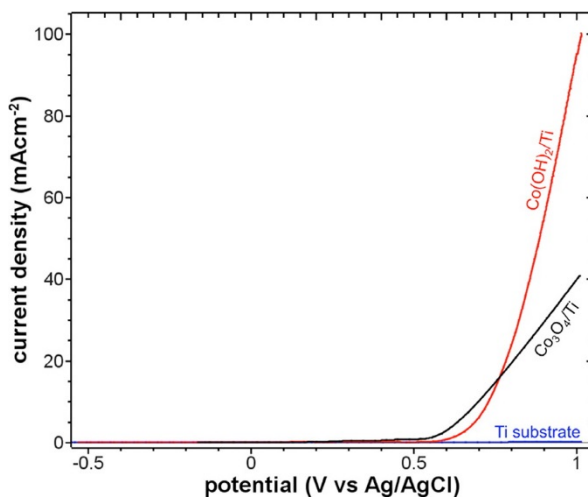
Figure 5. LSVs measured at 1 mV s^{-1} scan rate in 1 M KOH at electrodeposited $Co(OH)_2$ (red), crystalline Co_3O_4 (black), and uncoated Ti substrate (blue).

Figure 6 shows the initial CVs of the $Co(OH)_2$ film at 1 mV s^{-1} in 1 M KOH. In the first anodic scan (black), two peaks are observed. The first high current density peak

(A1) at 0.25 $V_{Ag/AgCl}$ is assigned to oxidation of $Co(OH)_2$ to CoOOH (eq 4).[2] The

second peak (A2) at about 0.4 $V_{Ag/AgCl}$ is attributed to the oxidation of CoOOH to CoO_2

(eq 5).[2] No reduction peak corresponding to A1 was observed. The A1 peak current

density reduces dramatically in the second scan and is not detected in the fifth scan

indicating that the oxidation of $Co(OH)_2$ to CoOOH is irreversible. This is in agreement

with results published by other researchers that $Co(OH)_2$ can be electrochemically

oxidized to CoOOH.[1,4] The analysis of the deposition and oxidation charges shows that

approximately 7% of the film is oxidized.
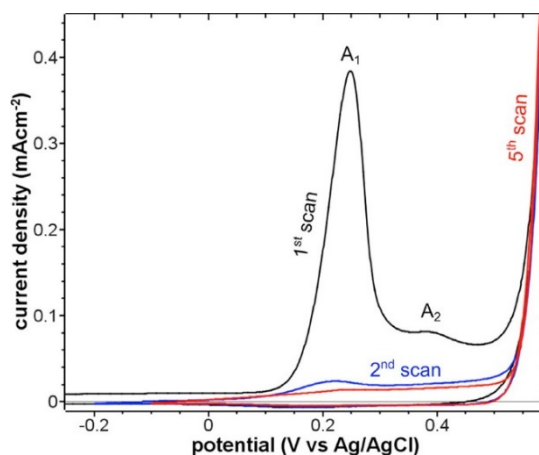
Figure 6. CVs of the $Co(OH)_2$ showing the film oxidation peaks prior to the onset of
OER. Voltammograms measured at 1 mV s^{-1} scan rate in 1 M KOH.

$$Co(OH)_2 + OH^- \rightarrow CoOOH + H_2O + e^- \tag{4}$$

$$CoOOH + OH^- \rightarrow CoO_2 + H_2O + e^- \tag{5}$$
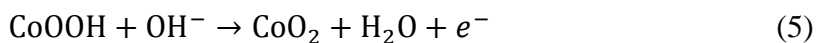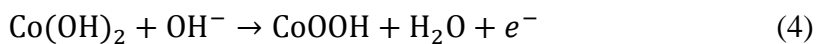
The film after OER experiments changes color from pink to black (Figure 7a).

SEM investigations (not shown) did not reveal any morphological changes caused by

film oxidation. Also the XRD pattern of the oxidized film did not show dramatic

changes. Only a shoulder to the (001) peak is observed (indicated with an arrow in Figure

7b) which could be assigned to the CoOOH(003) reflection. Figure 7c shows Raman

spectra of the as-deposited material (blue) and the film after OER experiments (red). The

as-deposited film spectrum (blue) matches that of Co(OH)2.[20] The spectrum of the

oxidized film (red) has the characteristic shape of CoOOH,[21-22] confirming the oxidation

of $Co(OH)_2$ to CoOOH.
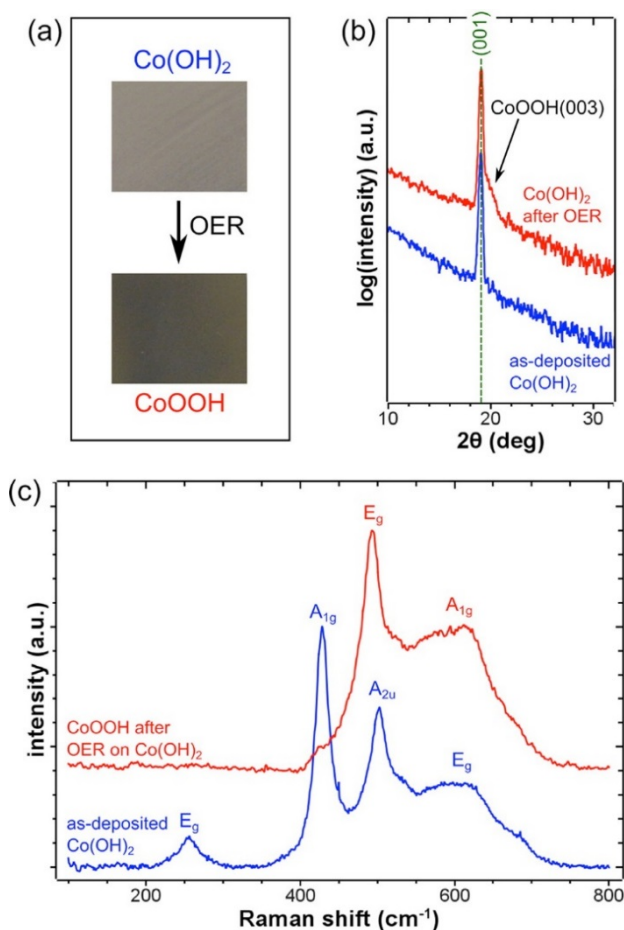
Figure 7. (a) Optical images of the $Co(OH)_2$ film prior to and after OER experiments. (b)
XRD patterns of the as-deposited $Co(OH)_2$ film (blue) and the film after the OER
experiments (red). (c) Raman spectra of as-deposited $Co(OH)_2$ (blue) and the film after
OER experiments (red).

4. CONCLUSIONS

We have shown that films of β-Co(OH)$_2$ can be deposited by electrochemical reduction of [Co(en)$_3$]$^{3+}$ in alkaline solution at room temperature. The low deposition temperature and cathodic deposition is ideal for electrodepositing Co(OH)$_2$ onto n-type semiconductor substrates. The as-deposited films are highly crystalline and do not require any further heat treatment. The β-Co(OH)$_2$ films exhibit excellent catalytic activity toward OER in 1 M KOH, comparable to Co$_3$O$_4$. During OER, the surface of the material is oxidized to CoOOH, which is a conductive material,[1] minimizing the IR drop due to the film resistivity. As only the surface of pink Co(OH)$_2$ film oxidizes to black CoOOH, the film should not adsorb light as strongly as black Co$_3$O$_4$. This could prove to be important if the material is used as an OER catalyst on n-type semiconductors in photoelectrochemical cells.

AUTHOR INFORMATION

Corresponding Author

*E-mail: jswitzer@mst.edu

Notes

The authors declare no competing financial interest.

ACKNOWLEDGEMENTS

REFERENCES

1. Pralong, V.; Delahaye-Vidal, A.; Beaudoin, B.; Leriche, J.-B.; Tarascon, J.-M. *J. Electrochem. Soc.* **2000**, 147, 1306

2. Chang, J.-K.; Wu, C.-M.; Sun, I.-W. *J. Mater. Chem.* **2010**, 20, 3729

3. Wu, J.; Zhang, D.; Wang, Y.; Wan, Y.; Hou, B. *J. Power Sources* **2012**, 198, 122

4. Subbaraman, R.; Tripkovic, D.; Chang, J. −C.; Strmcnik, D.; Paulikas, A. P.; Hirunsit, P.; Chan, M.; Greeley, J.; Stamenkovic, V.; Markovic, N. M. *Nat. Mater.* **2012**, 11, 550

5. Xu, Z. Z.; Chen, Z. C.; Joll, C.; Ben, Y.; Shen, J. M.; Tao, H. *Catal. Commun.* **2009**, 10, 1221

6. Liu, X. H.; Liu, W.; Hu, W. J.; Guo, S.; Lv, X. K.; Cui, W. B.; Zhao, X. G.; Zhang, Z. D. *Appl. Phys. Lett.* **2008**, 93, 202502

7. Garcia-Mota, M.; Bajdich, M.; Viswanathan, V.; Vojvodic, A.; Bell, A. T.; Nørskov, J. K. *J. Phys. Chem. C* **2012**, 116, 21077

8. Geng, B.; Zhan, F.; Jiang, H.; Xing, Z.; Fang, C. *Cryst. Growth Des.* **2008**, 8, 3497

9. Yarager, M. S.; Steinmiller, E. M. P.; Choi, K.-S. *Chem. Commun.* **2007**, 159

10. Zhou, W.-J.; Zhang, J.; Xue, T.; Zhao, D.-D.; Li, H. L. *J. Mater. Chem.* **2008**, 18, 905

11. Brownson, J. R. S.; Lévy-Clément, C. *Electrochim. Acta* **2009**, 54, 6637

12. Krause, R. A.; Megargle, E. A. *J. Chem. Educ.* **1976**, 53, 667

13. *Lange's Handbook of Chemistry*, 15th ed.; Dean, J. A., Ed.; McGraw-Hill, Inc.: New York, **1999**.

14. Marusak, R. A.; Doan, K.; Cummings, S. D. *Integrated Approach to Coordination Chemistry: An Inorganic Laboratory Guide*; John Wiley & Sons, Inc.: Hoboken, NJ, **2007**.

15. *CRC Handbook of Chemistry and Physics*, 74th ed.; Lide, D. R., Ed.; CRC Press, Inc.: Boca Raton, LA, **1994**.

16. Yang, J.; Liu, H.; Martens, W. N.; Frost, R. L. *J. Phys. Chem. C* **2010**, 114, 111

17. Biesinger, M. C.; Payne, B. P.; Grosvenor, A. P.; Lau, L. W. M.; Gerson, A. R.; Smart, R. St.C. *J. Appl. Surf. Sci.* **2011**, 257, 2717

18. *Handbook of X-ray Photoelectron Spectroscopy*; Chastain, J., Ed.; Perkin-Elmer Corporation: Eden Prairie, MN, **1992**.

19. Koza, J. A.; He, Z.; Miller, A. S.; Switzer, J. A. *Chem. Mater.* **2012**, 24, 3567

20. Shieh, S. R.; Duffy, T. S. *Phys. Rev. B* **2002**, 66, 134301

21. Ludvigsson, M.; Lindgren, J.; Tegenfeldt, J. *J. Mater. Chem.* **2001**, 11, 1269

22. Pauporté, T.; Mendoza, L.; Cassir, M.; Bernard, M. C.; Chivot, J. *J. Electrochem. Soc.* **2005**, 152, C49

II. ELECTRODEPOSITION OF EPITAXIAL Co(OH)₂ ON GOLD AND CONVERSION TO EPITAXIAL CoOOH AND Co₃O₄

Caleb M. Hull,[b] Jakub A. Koza,[b] and Jay A. Switzer[a]

Missouri University of Science and Technology, Department of Chemistry and Graduate Center for Materials Research, Rolla, MO 65409-1170, USA

ABSTRACT

An electrodeposition method for growing epitaxial $Co(OH)_2$ films on single crystalline gold (111), (100), and (110) substrates is described. The films were grown by electrochemical reduction of $[Co(en)_3]^{3+}$ in an alkaline electrolyte. The $Co(OH)_2$ grew with a [0001] out-of-plane orientation on all the gold crystal orientations. The in-plane orientation follows the symmetry of the gold (111), (100), and (110) substrates. The $Co(OH)_2$ can be converted to CoOOH by electrochemical oxidation in 1 M KOH at 95 °C, and after conversion remains epitaxial with a [0001] out-of-plane orientation. The CoOOH film can be further converted to epitaxial Co_3O_4 with a [111] out-of-plane orientation by decomposition of the CoOOH film in air at 300 °C. This synthesis method allows for a simple fabrication of epitaxial catalysts and could be useful to probe the catalytic activity of specific crystal planes.

1. INTRODUCTION

Replacement of precious metal catalysts with less expensive materials of similar activity is of high priority. Because cobalt is substantially less expensive, due to its relative earth abundance, much research is being conducted to replace these precious metal catalysts with cobalt derivatives.[1-6] Cobalt oxides have been shown to be catalytic toward the oxygen evolution reaction (OER),[7-10] and may be a useful substitute for the more expensive OER catalysts IrO_2, RuO_2, and PtO_2.[11-12]

Catalysis depends on the exposed surface of a material. Thus, different crystal orientations, having varied composition and morphology, have different catalytic activities toward a reaction.[13-15] For spinel cobalt oxide the {111} family of planes shows the greatest activity toward the OER,[15-17] as well as the oxygen reduction reaction.[18-19] We demonstrate a method to synthesize epitaxial Co_3O_4 with a [111] out-of-plane orientation as well as epitaxial $Co(OH)_2$ and CoOOH with [0001] out-of-plane orientations. Synthesis begins with the electrodeposition of an epitaxial $Co(OH)_2$ film. The $Co(OH)_2$ film can then be converted through electrochemical oxidation to CoOOH or through thermal decomposition to Co_3O_4. Interestingly, while each cobalt material has a different crystal structure and a large decrease in volume per cobalt atom occurs as $Co(OH)_2$ is converted into CoOOH and Co_3O_4, as shown in Figure 1, epitaxy is still maintained. To maintain epitaxy the film develops mesopores and micro-fissures within the converted films. The increased porosity could be advantageous for catalysis due to the increased surface area.[7]
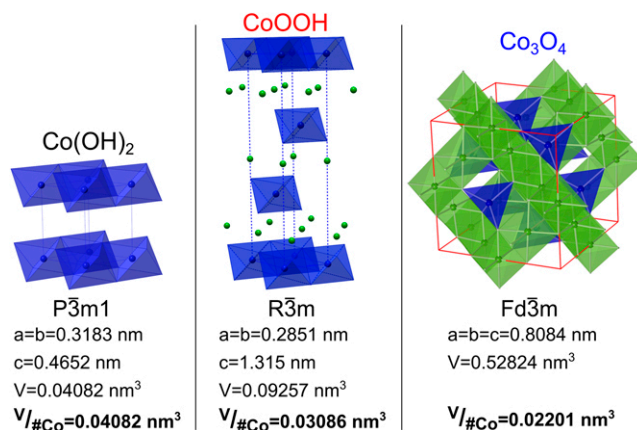
Figure 1. Unit cells of cobalt hydroxide, oxyhydroxide, and oxide with space groups, cell parameters, and volume per cobalt atom.

2. EXPERIMENTAL

2.1. ELECTRODEPOSITION OF Co(OH)$_2$

Co(OH)$_2$ films were deposited from an aqueous solution of 10 mM [Co(en)$_3$]Cl$_3$ (where, en = ethylenediamine) in 2 M NaOH similar to the procedure described previously.[20] The electrodeposition experiments were performed at room temperature in a standard three-electrode setup using a Brinkmann PGSTAT 30 Autolab potentiostat (Metrohm Autolab B.V., Utrecht, The Netherlands). Au single crystals of [111], [100], and [110] orientations were used as working electrodes. A Pt mesh served as the counter electrode. The single-crystalline Au substrates were electropolished in an electrolyte composed of 1:1:2 v/v 38% HCl:ethylene glycol:ethanol at 55 °C at an anodic current density of 1.5 A/cm^2.[21] The Co(OH)$_2$ films were deposited at −1 V versus Ag/AgCl/KCl$_{sat.}$, which served as the reference electrode. Films were deposited to a charge density of 0.5C cm^{-2}.

2.2. FILM CONVERSION

$Co(OH)_2$ films were converted to CoOOH by anodic oxidation in 1 M NaOH at 95 °C.[7] The conversion was performed through cyclic voltammetry (CV) by scanning from the open circuit potential to 0.3 $V_{Ag/AgCl}$ at a 10 mV/s scan rate for 20 cycles, similar to the procedure described previously.[7] Thermal decomposition of CoOOH films to Co_3O_4 was done by heating the films in a 300 °C oven in air for 1.5 h.[7]

2.3. CHARACTERIZATION

The films were characterized using a high-resolution Philips X'Pert MRD X-ray diffractometer (XRD; FEI Company, Eindhoven, The Netherlands) with a radiation source ($\lambda = 1.54056$ Å). The morphology of the films was studied by scanning electron microscopy (SEM; Hitachi S-4700 FESEM, Hitachi Corp., Tokyo, Japan, and Helios Nanolab 600 FIB, FEI Company).

3. RESULTS

Cobalt hydroxide was electrochemically deposited onto Au single crystal substrates. Figure 2 shows XRD patterns for $Co(OH)_2$ films deposited on Au single crystals of [111] (a), [100] (c), and [110] (e) orientations. Regardless of the substrate orientation, the films are highly textured, showing the {0001} peaks. As the substrate out-of-plane orientation does not affect the resulting out-of-plane order of the deposited film, the observed [0001] growth direction must be energetically favorable, as is also observed for electrodeposited zinc oxide.[22] Since a strong preferred out-of-plane orientation was observed for the films, the in-plane orientation was probed to determine

whether the films are epitaxial or fiber textured. We probed the in-plane orientations by measuring pole figures. If the sample were epitaxial the resulting pole figure would have high intensity spots caused by a coordinated reflection from each crystal as each crystal is aligned. Whereas a sample having fiber texture would give a high intensity ring in the pole figure, because the crystals are rotated in a random fashion. Figure 2 shows pole figures for $Co(OH)_2$ films deposited on Au(111) (b), (100) (d), and (110) (f) substrates. Irrespective of the substrate orientation, the pole figures have a spot pattern having tilt angle (ψ) of 40°. This is in agreement with the angle between the (0001) and planes ($\psi =$ 40.17°). The spot patterns indicate epitaxial growth of $Co(OH)_2$ films. The pole figure measured for the film deposited on Au(111) substrate shows 6-fold symmetry [Figure 2(b)]. While a 3-fold symmetric spot pattern is expected due to the crystal symmetry of $Co(OH)_2$, there are two equivalent in-plane orientations in which the crystals can grow on the Au(111) substrate. These two in-plane orientations are rotated 180° relative to each other which results in two sets of three spots, with each alternating spot coming from opposite orientations. Thus six spots are obtained, each rotated by 60°. We determined the epitaxial relationship on Au(111) as $Co(OH)_2(0001)$ ‖Au(111) . The pole figure measured for the film deposited on Au(100) substrate has 12-fold symmetry with spots rotated by an angle of 30° [Figure 2(d)]. Again this can be explained, because there are four equivalent in-plane orientations that $Co(OH)_2$ can grow on the Au(100) substrate, each rotated by 90°. Thus four sets of three spots are observed in the pole figure, each set rotated by 90°. The epitaxial relationship for the film deposited on Au(100) substrate was determined to be $Co(OH)2(0001)$ ‖Au(100) $\langle 011 \rangle$. The pole figure for the film deposited on Au(110) substrate [Figure 2(f)] shows six spots just as the Au(111)

substrate. Again there are two equivalent in-plane orientations rotated by 180° which the Co(OH)$_2$ can grow on the substrate. This is a result of the 2-fold symmetry of the Au(110) plane. While we observe six intense spots, there is also a low intensity ring indicative of some contribution of a fiber texture (random in-plane order of crystals). The epitaxial relationship for the film deposited on Au(110) substrate is Co(OH)$_2$(0001) ‖Au(110) 〈001〉 .
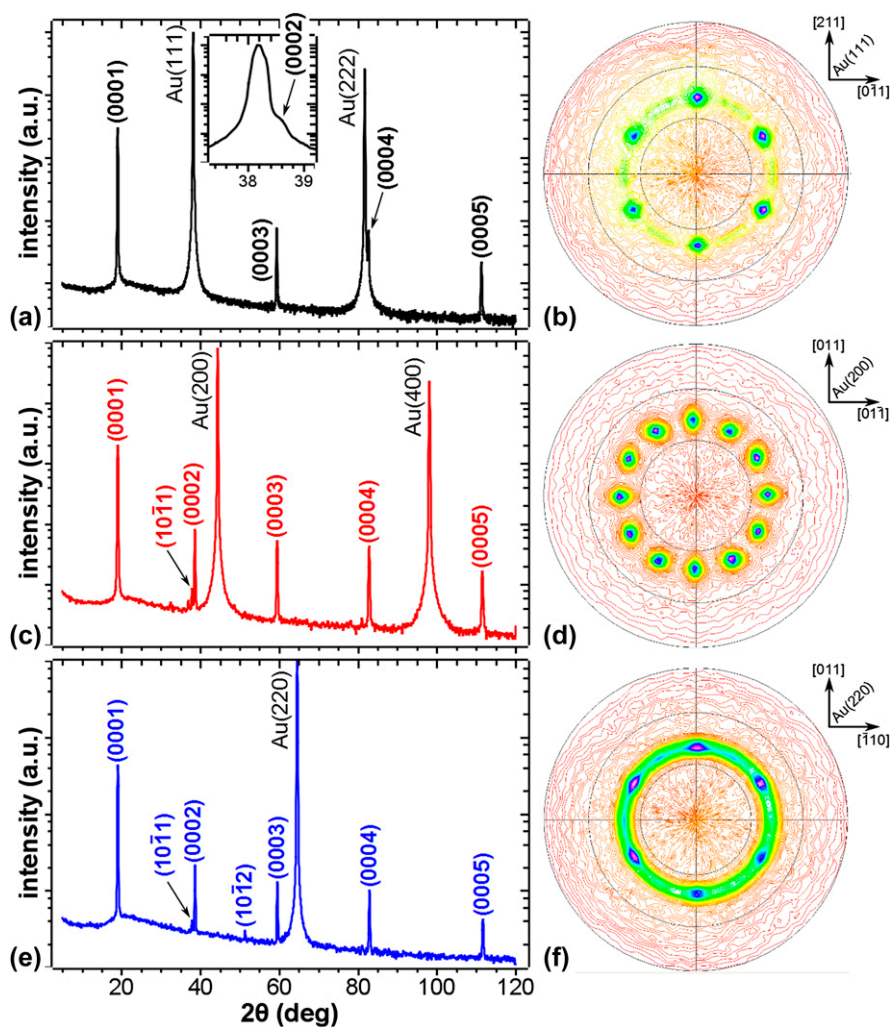
Figure 2. XRD patterns and pole figures of Co(OH)$_2$ deposited on Au(111) (a and b), Au(100) (c and d), and Au(110) (e and f) single crystals.

Figure 3 shows SEM plan view images of the $Co(OH)_2$ films deposited on Au(111) (a), Au(100) (b), and Au(110) (c) substrates. The films all have a similar morphology. As already reported for the [0001] textured films deposited on Au coated glass substrate,[7] the films consist of conical grains having flat faces exposed. The majority of grains are oriented with the flat faces parallel to the substrate. However, the film deposited on Au(110) substrate has a number of cones which are tilted [Figure 3(c)]. In all cases, the films consist of features with flat surfaces and nearly round microcones that do not show the expected faceting. This suggests that the microcones consist of smaller nanometer-scale crystallites that assemble into this microcone morphology. We note that the initial deposits of $Co(OH)_2$ show faceted hexagonal nanograins in the atomic force microscope (image not shown).
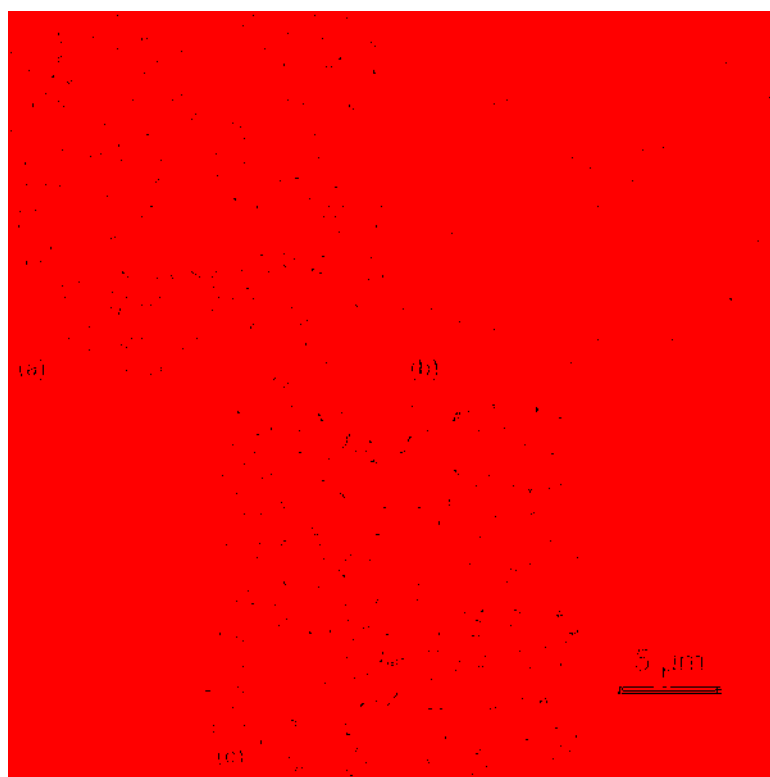
Figure 3. Plan view SEM micrographs of $Co(OH)_2$ films deposited on Au(111) (a), Au(100) (b), and Au(110) (c) single crystals.

To probe the mosaic spread of the epitaxy we measured rocking curves at the (0001) Co(OH)$_2$ peak (Figure 4). The films deposited on Au(111) (black) and Au(100) (blue) show relatively sharp peaks of full width at half maximum (FWHM) of 2.0° and 1.5°, respectively. However, the film deposited on Au(110) substrate has a FWHM of 4.0° (red in Figure 4), twice as broad as on the other substrates. This means that there is a larger mosaic spread for the film on Au(110) substrate, which is in agreement with the tilted cones observed by SEM [Figure 3(c)].
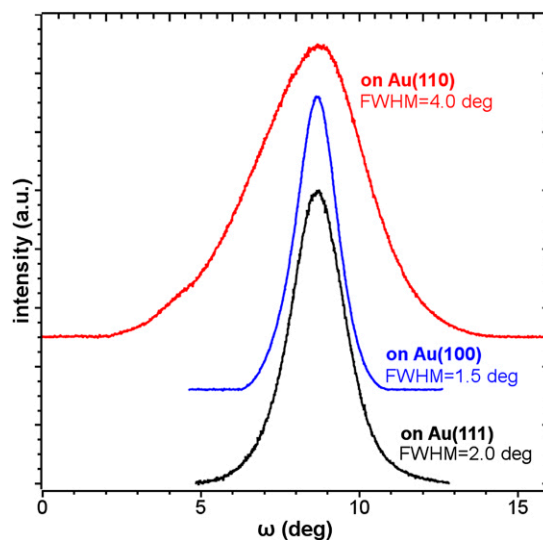
Figure 4. X-ray rocking curves measured at (0001) peak for Co(OH)$_2$ films deposited on Au(111) (black), Au(100) (blue), and Au(110) (red). The full width at half maximum (FWHM) are as indicated.

We modeled the Co(OH)$_2$/Au interfaces for the different substrate orientations. Figure 5 shows the interface model of Co(OH)$_2$(0001) on Au(111) (a), Au(100) (b), and Au(110) (c) oriented according to the epitaxial relationships determined from pole figures. A Moiré pattern in the interface model for Co(OH)$_2$(0001) on Au(111) can be seen giving a coincident site lattice (CSL) in the shape of an equilateral triangle of 11 Co

atoms along the $[11\bar{2}0]$, $[2\bar{1}\bar{1}0]$, $[\bar{1}210]$ and directions. The CSL results in a lattice

mismatch of only 0.028%. The CSL of $Co(OH)_2(0001)$ on Au(100) forms a rectangle

having again 11 cobalt atoms on each side. The lattice mismatch for the CSL is 0.3%

along the direction and 0.03% along the direction. The smallest CSL is found for

$Co(OH)_2(0001)$ on Au(110), however it had the largest mismatch. The CSL in this case

also has a rectangular shape having 4 Co atoms along direction with a mismatch of 1.07%

and 11 Co atoms along direction with a mismatch of 0.03%. The lattice mismatch of

1.07% for $Co(OH)_2(0001)$ on Au(110), highest among other substrates, could be

responsible for the increased mosaic spread observed in this system.

As we previously reported, it is possible to oxidize $Co(OH)_2$ films to either

CoOOH or Co_3O_4 by electrochemical and thermal means.[7] It has also been shown that

conversion of cobalt hydroxide to higher oxides does not always cause a change in

morphology.[23-25] Xu et al. report that conversion of β-$Co(OH)_2$ to Co_3O_4 via thermal

decomposition in air results in Co_3O_4 with morphologies dependent on the $Co(OH)_2$

starting material.[26] They further reported a decrease in crystallite size and subsequent

increase in porosity in the decomposed sample. This is not only observed in

polycrystalline samples, but in single crystals as well. Lou et al. synthesized single crystal

nano-needles of β-$Co(OH)_2$, which remained single crystalline after decomposition to

Co_3O_4, even upon development of mesopores.[27]
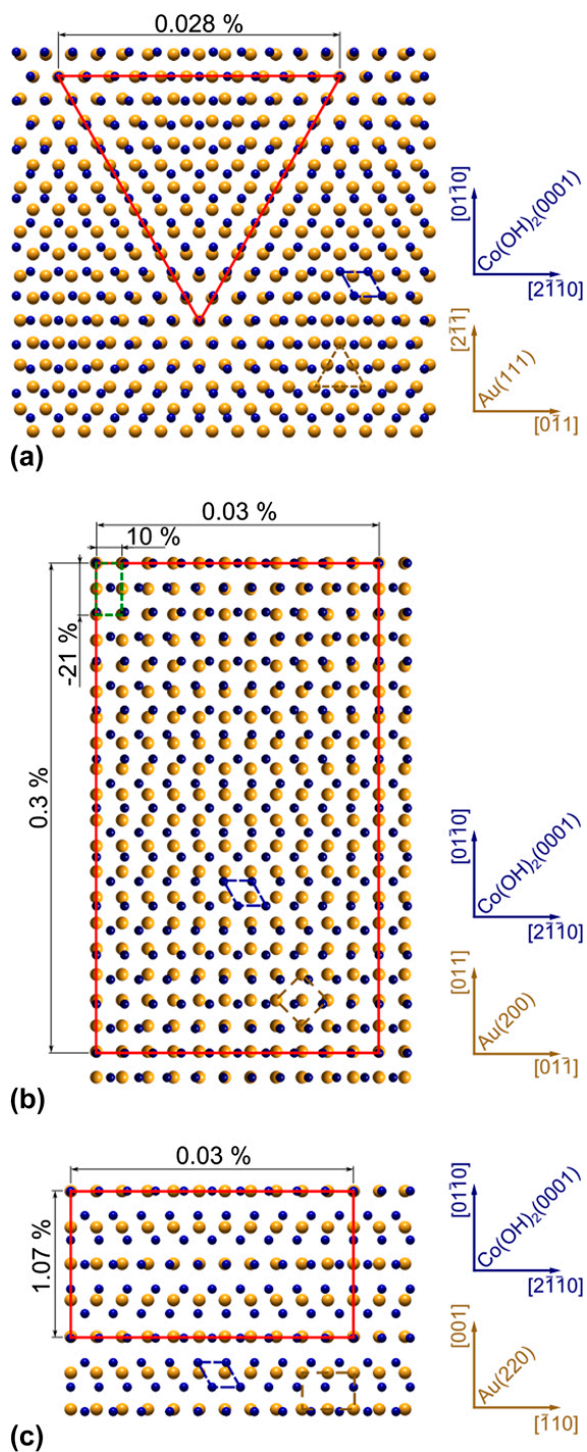
Figure 5. Interface models of Co(OH)$_2$(0001) on Au(111) (a) Au(100) (b), and Au(110) (c). Only Co atoms are shown for Co(OH)$_2$ as blue spheres. The Au atoms are shown as yellow spheres. Co(OH)$_2$(0001) unit cell is indicated in blue, and Au unit cells are highlighted in yellow. The CSLs are drawn in red. Insets show the directions in Co(OH)$_2$(0001) and Au planes.

We hypothesized that if one started with epitaxial $Co(OH)_2$ films, one could produce both epitaxial CoOOH and epitaxial Co_3O_4 films. We tested this hypothesis by oxidizing a $Co(OH)_2$ film deposited on Au(100) single crystal substrate. The film was first oxidized electrochemically. The XRD pattern of the oxidized film shown in Figure 6(a), is assigned to trigonal CoOOH with only {0001} reflections present. This once again shows the high level of out-of-plane order of the film upon oxidation. A slight broadening of the sample peaks is also observed, which could be due to a decrease in crystallite size. The CoOOH pole figure is shown in Figure 6(b). It has a spot pattern, indicating in-plane order in the film. The CoOOH pole figure shows 12 spots separated by 30° at a ψ angle of 47° in agreement with the angle between (0001) and planes of CoOOH ($\psi = 46.81°$). We have shown previously that the conversion starts at the film/electrolyte interface.[7] Thus the four orientations of $Co(OH)_2$ are maintained in the CoOOH film resulting in twelve spots just as in the pole figure for $Co(OH)_2$ on Au(100) [Figure 2(e)]. The epitaxial relationship is CoOOH(0001) ∥Au(100) $\langle 011 \rangle$. The CoOOH film was annealed in air at 300 °C. Decomposition through thermal means produced Co_3O_4, which displayed only reflections of the {111} planes in the XRD pattern [Figure 6(c)]. This shows the conversion of trigonal CoOOH to the cubic spinel structure of Co_3O_4. Again peak broadening was observed, just as with the oxidation of $Co(OH)_2$ to CoOOH. The Co_3O_4(220) pole showed a distinct 12 spot pattern with the spots separated by 30° at a ψ angle of 35° corresponding to the angle between (111) and (220) planes in the spinel structure of Co_3O_4 ($\psi = 35.26°$). Twelve spots are due to the combination of 3-fold symmetry of the Co_3O_4(111) plane with the 4-fold Au(100) substrate. The epitaxial relationship was determined as Co_3O_4(111) ∥Au(100) $\langle 001 \rangle$.

This is the same epitaxial relationship we previously reported for the directly deposited epitaxial Co_3O_4 films on Au(100).[11]
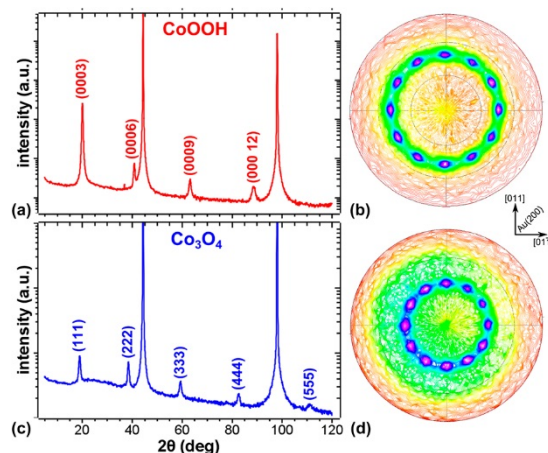
Figure 6. XRD patterns and pole figures of CoOOH converted by anodic oxidation of $Co(OH)_2$ (a and b) and Co_3O_4 thermally decomposed from CoOOH (c and d).

The interface models for the converted films are shown in Figure 7. The CoOOH and $Co(OH)_2$ both grow with the [0001] direction perpendicular to the substrate. Hence they have a hexagonal basal plane parallel to the surface, and therefore we can calculate the lattice mismatch of a single unit cell. The lattice mismatch for a single CoOOH(0001) unit cell overlaid on the $Co(OH)_2$(0001) unit cell gives a mismatch of −10.15% [Figure 7(a)]. However, if we expand the surface net a clear Moiré pattern is seen, giving a CSL in the shape of an equilateral triangle of 10 Co atoms along , , and directions. This CSL reduces the mismatch to only −0.16%. The Co_3O_4(111) on Au(100) interface model is shown in Figure 7(b). A triangular CSL is found with a mismatch of 0.1 and 0.04%.
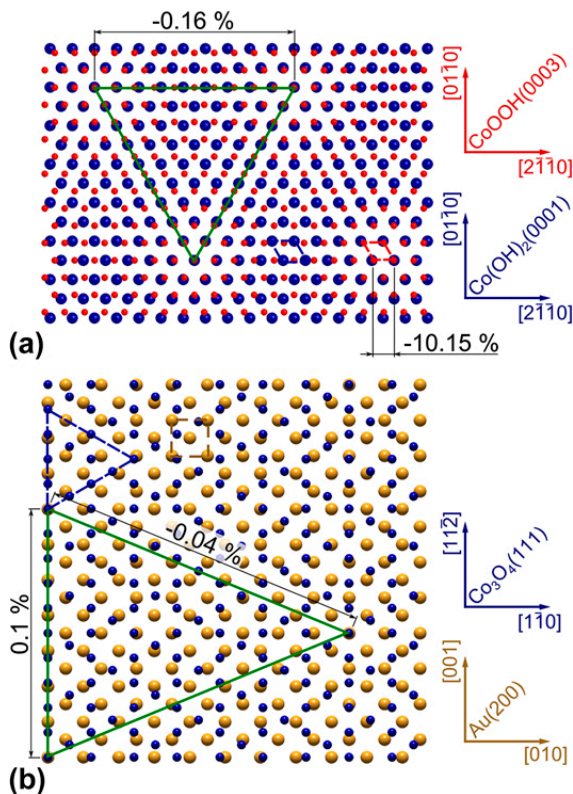
Figure 7. (a) Interface model of CoOOH(0001) on Co(OH)$_2$(0001). Small blue spheres stand for Co atoms on CoOOH(0001) plane and blue spheres represent Co atoms on the Co(OH)$_2$(0001) plane. (b) Interface model of Co$_3$O$_4$(111) on Au(100). Only Co atoms are shown for Co$_3$O$_4$ as blue spheres. The Au atoms are shown as yellow spheres. CoOOH(0001) unit cell is shown with red dashed line. Co(OH)$_2$(0001) and Co$_3$O$_4$(111) unit cells are indicated with blue dashed lines, and Au(100) unit cell is highlighted in yellow. The CSLs are drawn in green.

As previously mentioned, peak broadening was observed in the XRD patterns after each conversion, suggesting decreasing crystallite size. Using the Williamson–Hall analysis (Figure 8) the lattice strain ($\Delta d/d$) and crystallite size (t) was calculated.[28] The Williamson–Hall equation:

$$\beta_{hkl} \cos(\theta) = \frac{K\lambda}{t} + 4\left(\frac{\Delta d}{d}\right) \sin(\theta) \tag{1}$$

relates the peak broadening to the strain in the crystal, which when graphed versus , gives a slope equal to the crystal strain and a Y-intercept which is a rearrangement of the Scherrer equation (where K is the dimensionless shape factor (0.94), λ is the wave length of the x-ray). Note that the x-ray measurements probe the size and strain of the entire film on the Au single-crystal substrates. As expected, the as-deposited $Co(OH)_2$ films had little to no strain, with a $\Delta d/d = 0.0\%$. The as-deposited film also had the largest crystallite size of 42 nm. The CoOOH films exhibited the greatest strain (the steepest slope in Figure 8) with a $\Delta d/d = 0.6\%$ and a crystallite size of 31 nm. The Co_3O_4 film showed decreased strain of 0.4% compared to the CoOOH film. The crystallite size of the Co_3O_4 was the smallest with a size of 14 nm. The release of strain in Co_3O_4 is most likely observed due to the elevated temperature during decomposition (300 °C). While the temperature is well below the decomposition point of Co_3O_4 (895 °C),[29] it could be high enough to release some of the strain.
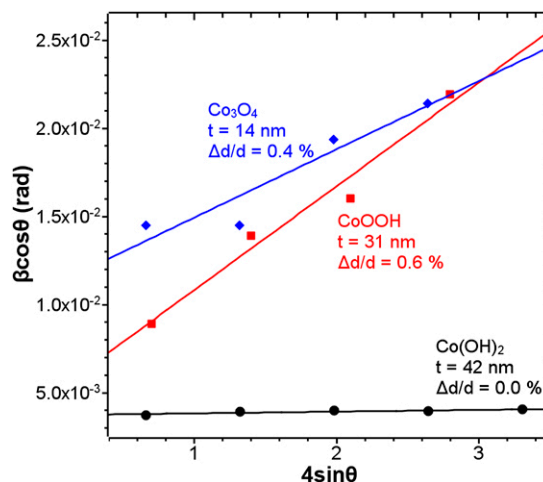
Figure 8. Williamson–Hall analysis of as-deposited $Co(OH)_2$ film (black spheres), electrochemically oxidized to CoOOH (red squares), and Co_3O_4 (blue diamonds).

Figure 9 shows the plan view (a, c, and e) and cross-sectional (b, d, and f) SEM images of the film before and after each conversion step. The films after each step of the conversion retain the conical-like grain shape, as we previously reported for the textured films.[7] The as-deposited material shows no cracks on the surface of the cones [Figure 9(a)] and no porosity in the bulk of the cones [Figure 9(b)]. However, after electrochemical conversion to CoOOH both surface cracks [Figure 9(c)] and porosity inside the cones [Figure 9(d)] develop. The size and number of surface cracks [Figure 9(e)] as well as porosity [Figure 9(f)] continue to increase after thermal decomposition to Co_3O_4. In this case a significant surface roughening is also seen [inset of Figure 9(e)]. This effect was reported for decomposition of single crystalline CoOOH nano-needles to Co_3O_4 nano-needles as well.[27] The nano-needles retained their original geometry and were still single crystalline, but a nanoporosity developed,[27] similar to the results we observed.

The nanoporosity can be explained based on the shrinkage of the film due to the structure changes. Comparing the crystal structure of $Co(OH)_2$ to that of CoOOH and Co_3O_4 reveals that, upon conversion, the volume occupied per cobalt atom decreases (Figure 1). $Co(OH)_2$, which has a trigonal space group changes to a space group of when oxidized to CoOOH. However, upon decomposition to Co_3O_4 the entire crystal system changes, adopting the cubic symmetry. This is accompanied by an almost 2-fold shrinkage of the unit cell volume calculated per Co atom. Experimentally this induces strain, increases porosity, and results in creation of micro-fissures through the crystallites. The formation of nanopores and cracks allows maintenance of the cone-like grain morphology despite the large film volume shrinkage. This is analogous to the results

reported for the single-crystalline CoOOH nano-needles.[27] Both the increased strain and increased porosity could enhance the catalytic activity of the CoOOH.
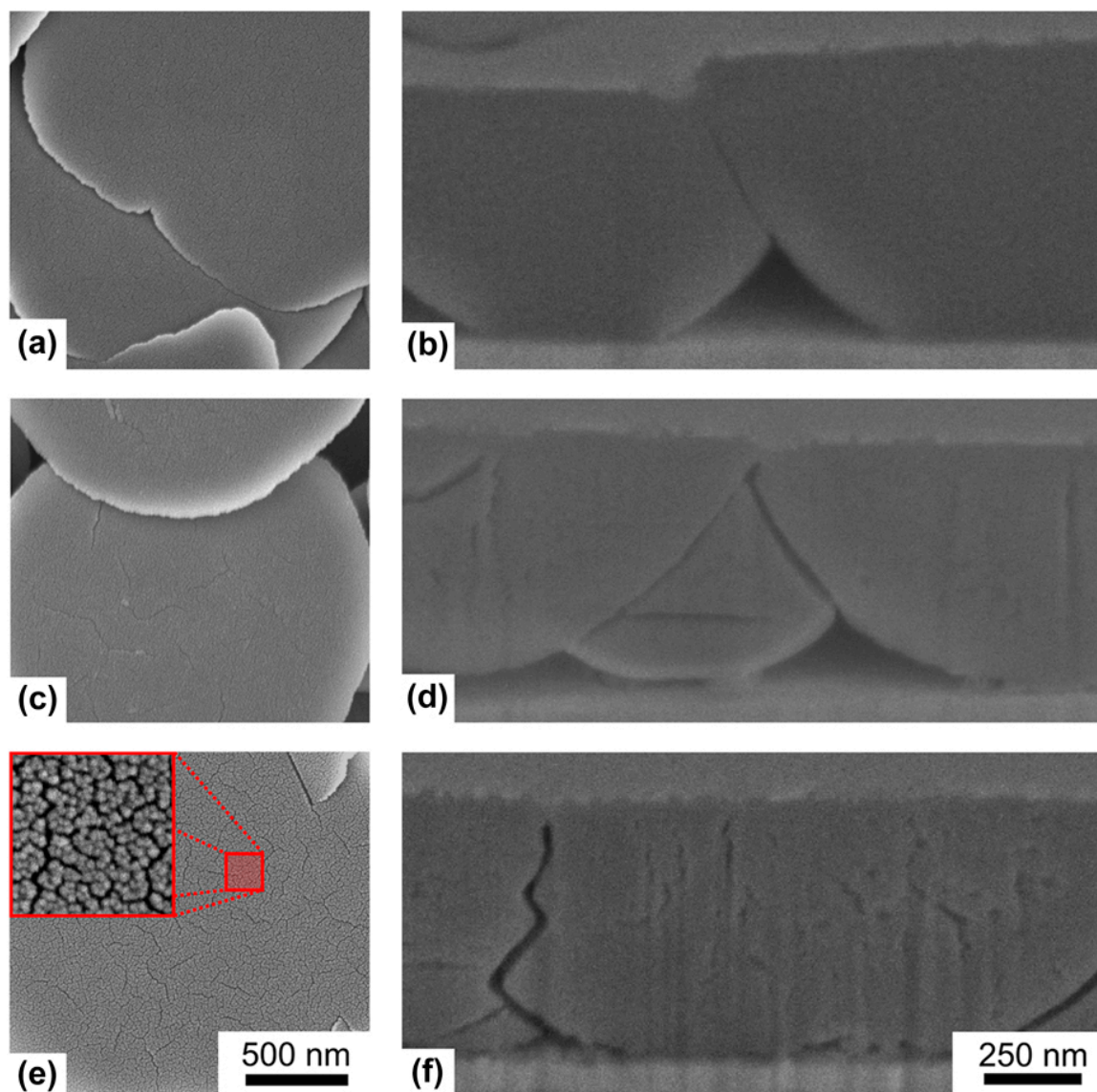
Figure 9. SEM images of the surface (left column) and cross-section (right column) of the as-deposited $Co(OH)_2$ (a and b), after electrochemical conversion to CoOOH (c and d), and CoOOH oxidized to Co_3O_4 (e and f). The inset in (e) is the magnified surface area highlighted with the red square.

4. CONCLUSION

We have shown that epitaxial $Co(OH)_2$ films can be electrodeposited on Au single crystals. Deposits grow in the [0001] out-of-plane direction independent of the substrate orientation. However, the in-plane orientation is determined by the gold crystal orientation. Films develop a cone-like microstructure and are uniform with very flat surfaces and negligible strain.

$Co(OH)_2$ can be converted to CoOOH by electrochemical oxidation, which after conversion remains epitaxial with a [0001] out-of-plane orientation. The CoOOH film can be further converted to epitaxial Co_3O_4 with a [111] out-of-plane orientation by thermal decomposition in air. Williamson–Hall analysis revealed that after electrochemical oxidation of $Co(OH)_2$ to CoOOH the strain in the film increases and the crystallite size decreases. Thermal decomposition of CoOOH to Co_3O_4 leads to a reduction of strain in the film and a further decrease in the crystallite size.

The film after each conversion step retains the micro-cone morphology despite the fact that the cell volume per cobalt atom is decreased nearly 2-fold after converting from $Co(OH)_2$ to Co_3O_4. As a result the films develop increased porosity and micro-fissures.

This method allows for a simple fabrication of epitaxial catalysts with Co oxidation states of II, III, or a mixture of II and III, depending on the catalyst need. The converted films have the added benefit of increased surface area due to the inherent porosity caused by conversion. Thanks to the epitaxial growth, the catalytic activity of separate crystal planes toward different chemical reactions could be probed. One such

reaction would be the OER, which is a critical reaction in realizing economical solar

hydrogen production.

AUTHOR INFORMATION

a) Address all correspondence to this author. E-mail: jswitzer@mst.edu

b) These authors contributed equally to this work.

ACKNOWLEDGEMENTS

REFERENCES

1. Zhang, G., Scott, B.L., and Hanson, S.K.: Mild and homogeneous cobalt-catalyzed hydrogenation of C=C, C=O, and C=N bonds. *Angew. Chem., Int. Ed.* **51**, 12102–12106 (2012).

2. Becker, R. and Jones, W.D.: Cobalt and nickel catalyzed reactions involving C–H and C–N activation reactions. *In Catalysis Without Precious Metals* (Wiley-VCH Verlag GmbH & Co. KGaA, Berlin, 2010); pp. 143–164.

3. Gibson, V.C. and Solan, G.A.: Olefin oligomerizations and polymerizations catalyzed by iron and cobalt complexes bearing bis(imino)pyridine ligands. *In Catalysis Without Precious Metals* (Wiley-VCH Verlag GmbH & Co. KGaA, Berlin, 2010); pp. 111–141.

4. Reece, S.Y., Hamel, J.A., Sung, K., Jarvi, T.D., Esswein, A.J., Pijpers, J.J.H., and Nocera, D.G.: Wireless solar water splitting using silicon-based semiconductors and earth-abundant catalysts. *Science* **334**, 645–648 (2011).

5. Tsui, L-k., Zafferoni, C., Lavacchi, A., Innocenti, M., Vizza, F., and Zangari, G.: Electrocatalytic activity and operational stability of electrodeposited Pd–Co films towards ethanol oxidation in alkaline electrolytes. *J. Power Sources* **293**, 815–822 (2015).

6. Seabold, J.A. and Choi, K-S.: Effect of a cobalt-based oxygen evolution catalyst on the stability and the selectivity of photo-oxidation reactions of a WO_3 photoanode. *Chem. Mater.* **23**, 1105–1112 (2011).

7. Liu, Y-C., Koza, J.A., and Switzer, J.A.: Conversion of electrodeposited $Co(OH)_2$ to CoOOH and Co_3O_4, and comparison of their catalytic activity for the oxygen evolution reaction. *Electrochim. Acta* **140**, 359–365 (2014).

8. Hill, J.C., Landers, A.T., and Switzer, J.A.: An electrodeposited inhomogeneous metal–insulator–semiconductor junction for efficient photoelectrochemical water oxidation. *Nat. Mater.* **14**, 1150–1155 (2015).

9. McCrory, C.C.L., Jung, S., Peters, J.C., and Jaramillo, T.F.: Benchmarking heterogeneous electrocatalysts for the oxygen evolution reaction. *J. Am. Chem. Soc.* **135**, 16977–16987 (2013).

10. Yeo, B.S. and Bell, A.T.: Enhanced activity of gold-supported cobalt oxide for the electrochemical evolution of oxygen. *J. Am. Chem. Soc.* **133**, 5587–5593 (2011).

11. Koza, J.A., He, Z., Miller, A.S., and Switzer, J.A.: Electrodeposition of crystalline Co_3O_4—A catalyst for the oxygen evolution reaction. *Chem. Mater.* **24**, 3567–3573 (2012).

12. Trasatti, S.: Electrocatalysts in the anodic evolution of oxygen and chlorine. *Electrochim. Acta* **29**, 1503–1512 (1984).

13. Zhou, Z.Y., Tian, N., Li, J.T., Broadwell, I., and Sun, S.G.: Nanomaterials of high surface energy with exceptional properties in catalysis and energy storage. *Chem. Soc. Rev.* **40**, 4167–4185 (2011).

14. Hu, L., Peng, Q., and Li, Y.: Selective synthesis of Co_3O_4 nanocrystal with different shape and crystal plane effect on catalytic property for methane combustion. *J. Am. Chem. Soc.* **130**, 16136 (2008).

15. Su, D., Dou, S., and Wang, G.: Single crystalline Co_3O_4 nanocrystals exposed with different crystal planes for $Li–O_2$ batteries. *Sci. Rep.* **4**, 5767 (2014).

16. Singh, R.N., Koenig, J.F., Poillerat, G., and Chartier, P.: Thin films of Co_3O_4 and $NiCo_2O_4$ obtained by the method of chemical spray pyrolysis for electrocatalysis III. The electrocatalysis of oxygen evolution. *J. Appl. Electrochem.* **3**, 442–446 (1990).

17. Chen, Z., Kronawitter, C., and Koel, B.: Facet-dependent activity and stability of Co_3O_4 nanocrystals towards the oxygen evolution reaction. *Phys. Chem. Chem. Phys.* **17**, 29387–29393 (2015).

18. Xie, X. and Shen, W.: Morphology control of cobalt oxide nanocrystals for promoting their catalytic performance. *Nanoscale* **1**, 50–60 (2009).

19. Xiao, J., Kuang, Q., Yang, S., Xiao, F., Wang, S., and Guo, L.: Surface structure dependent electrocatalytic activity of Co_3O_4 anchored on graphene sheets toward oxygen reduction reaction. *Sci. Rep.* **3**, 2300 (2013).

20. Koza, J.A., Hull, C.M., Liu, Y-C., and Switzer, J.A.: Deposition of β-$Co(OH)_2$ films by electrochemical reduction of tris(ethylenediamine)cobalt(III) in alkaline solution. *Chem. Mater.* **25**, 1922–1926 (2013).

21. Boonsalee, S., Gudavarthy, R.V., Bohannan, E.W., and Switzer, J.A.: Epitaxial electrodeposition of tin(II) sulfide nanodisks on single-crystal Au(100). *Chem. Mater.* **20**, 5737–5742 (2008).

22. Liu, R., Vertegel, A.A., Bohannan, E.W., Sorenson, T.A., and Switzer, J.A.: Epitaxial electrodeposition of zinc oxide nanopillars on single-crystal gold. *Chem. Mater.* **13**, 508–512 (2001).

23. Cheng, J.P., Shereef, A., Gray, K., and Wu, J.: Development of hierarchically porous cobalt oxide for enhanced photo-oxidation of indoor pollutants. *J. Nanopart. Res.* **17**, 1–9 (2015).

24. Kung, C-W., Cheng, Y-H., Tseng, C-M., Chou, L-Y., and Ho, K-C.: Low-temperature and template-free fabrication of cobalt oxide acicular nanotube arrays and their applications in supercapacitors. *J. Mater. Chem. A* **3**, 4042–4048 (2015).

25. Tan, X., Gao, H., Yang, M., Luan, Y., Dong, W., Jin, Z., Yu, J., Qi, Y., Feng, Y., and Wang, G.: Synthesize of hierarchical sisal-like cobalt hydroxide and its electrochemical applications. *J. Alloys Compd.* **608**, 278–282 (2014).

26. Xu, J.M., Zhang, J., Wang, B.B., and Liu, F.: Shape-regulated synthesis of cobalt oxide and its gas-sensing property. *J. Alloys Compd.* **619**, 361–367 (2015).

27. Lou, X.W., Deng, D., Lee, J.Y., and Archer, L.A.: Thermal formation of mesoporous single-crystal Co_3O_4 nano-needles and their lithium storage properties. *J. Mater. Chem.* **18**, 4397–4401 (2008).

28. Williamson, G.K. and Hall, W.H.: X-ray line broadening from filed aluminium and wolfram. *Acta Metall.* **1**, 22–31 (1953).

29. Haynes, W.M., Lide, D.R., and Bruno, T.J.: *CRC Handbook of Chemistry and Physics: A Ready-reference Book of Chemical and Physical Data* (CRC Press, Boca Raton, FL, 2015).

III. ELECTRODEPOSITED EPITAXIAL Cu(100) ON Si(100) AND LIFT-OFF OF SINGLE-CRYSTAL-LIKE Cu(100) FOILS

Caleb M. Hull and Jay A. Switzer*

Missouri University of Science and Technology, Department of Chemistry and Graduate Center for Materials Research, Rolla, MO 65409-1170, USA

ABSTRACT

A two potential step electrodeposition technique is described which gives epitaxial films of Cu(100) on n-Si(100). Nucleation of epitaxial seeds occurs at -1.5 $V_{Ag/AgCl}$, while the film is grown at -0.5 $V_{Ag/AgCl}$. Cu deposition occurs with an 82.0% Faradaic efficiency as determined spectrophotometrically. Epitaxy is achieved through a 45° in-plane rotation of the Cu with respect to the Si, which is shown by x-ray analysis. The 45° rotation reduces the lattice mismatch from ⁻33.43% for an unrotated film to ⁻5.86% for a 45° rotated film. Mosaicity, as determined via x-ray rocking curves, decreases with increasing thickness, going from a full width at half maximum of 3.99° for a 30 nm thick film to 1.67° for a 160 nm thick film. This translates to an increasing quality of epitaxy with increasing thickness. High resolution TEM imaging shows an
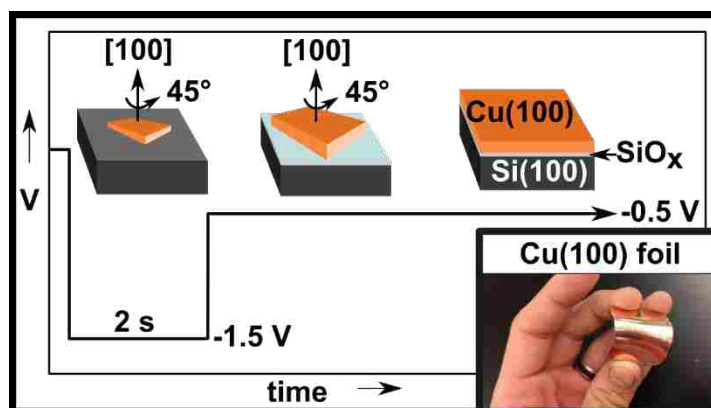
amorphous SiO_x interlayer between the Cu and Si. Etching of the SiO_x with 5% HF

allows for epitaxial lift-off of the copper film giving a single-crystal-like Cu(100) foil.

Cu(100) films and single-crystal-like foils have potential use as catalysts for CO_2

reduction, substrates for technologically important materials like spintronic multilayer

magnetic stacks and high temperature superconductors, and as active surfaces towards

galvanic replacement by platinum group elements. Additionally, the foils could be used

as single-crystal-like substrates for flexible electronics.

KEYWORDS: electrodeposition,epitaxy, copper, silicon, single-crystal, foil.

1. INTRODUCTION

Epitaxial films of copper (Cu) offer an ordered substrate at a lower cost than Cu

single crystals. To date, epitaxial films of Cu have been deposited on silicon (Si) through

vacuum techniques of thermal evaporation,[1] ion beam evaporation,[2] molecular beam

epitaxy,[3-6] and magnetron sputtering.[7-8] However, epitaxial Cu films on Si by

electrochemical means has yet to be accomplished. Electrodeposition offers a highly

scalable deposition process which gives a comparable level of control over film thickness

as vacuum deposition, but at a lower capital cost. The applied potential in

electrodeposition provides a level of control that is not available to either vapor

deposition or to other solution deposition methods. The potential can be used to select

which species will be oxidized or reduced in a multicomponent system, and to control the

rate of that redox reaction. In addition, when depositing on lithographically patterned

substrates, electrodeposition fills only the patterned area rather than covering the entire

surface. This eliminates the need for a secondary step to remove the unwanted deposited

material. However, epitaxial electrodeposition of a metal on silicon is not trivial. In fact, the only example of direct epitaxial electrodeposition of any metal film on Si is that of Au, being pioneered by Allongue and co-workers,[9-10] and further studied by Switzer et al.[11] The difficulty in epitaxial electrodeposition on Si is due to the propensity of Si to oxidize, reacting quickly with the aqueous electrolyte to form a disordered surface layer of amorphous SiO_x. Allongue and co-workers,[9-10] prevented the oxidation of Si by depositing gold at a potential more negative than the potential at which Si oxidizes. Here, we detail a two potential step electrochemical nucleation and growth method to produce epitaxial Cu(100) films on Si(100). Through a simple chemical etch and lift-off procedure, epitaxial Cu(100) films are removed from the Si substrate producing free-standing, single-crystal-like foils suitable as substrates for ordered flexible electronics.

Epitaxial films of Cu have found use as substrates for spintronic devices,[12-18] and could also be useful as substrates for high temperature superconducting materials.[19-21] Key electrochemical reactions utilizing Cu catalysts such as the reduction of CO_2 to fuels[22-24] could also benefit from epitaxial Cu(100) films, because they could provide access to the most active atomic plane. For instance, the Cu(100) surface has shown greater activity than the Cu(111) surface towards electroreduction of CO_2 to ethylene[25-27] and the direct hydrogenation of CO_2 to methanol.[28]

Epitaxial lift-off is accomplished in this work through selective etching of an interfacial amorphous SiO_x that forms during Cu growth. After etching in 5% HF the Cu film is adherent enough to facilitate rinsing, drying, and application of an adhesive. The film is removed by peeling the adhesive substrate, with the Cu foil, off of the Si. Single-crystal-like Cu foils could be useful as a highly ordered flexible substrate in much the

same way as the rolling assisted biaxially textured substrates (RABiTS) developed by

Goyal et al.[29] The vast research on RABiTS in applying buffer layers,[30-32] depositing

high temperature superconductors,[33-34] and use in photovoltaics[35] should be directly

applicable to these single-crystal-like Cu foils. The versatility and high crystalline order

could allow Cu single-crystal-like foils to pave the way to inexpensive, flexible,

advanced electronic devices.

2. EXPERIMENTAL DETAILS

2.1. ELECTROCHEMICAL METHODS

Cu was deposited from a pH 3 electrolyte containing 2 mM $CuSO_4$, 0.1 M K_2SO_4,

and 1 mM H_2SO_4. During deposition the solution was kept at room temperature and

stirred at 250 RPM with a magnetic stir bar. The n-Si(100) was prepared by first

cleaning the wafer via the RCA standard method, breaking the wafer into roughly 1 cm^2

pieces, applying GaIn eutectic to form an ohmic back contact, attaching a silver wire with

Silver Print II (GC Electronics), and then electrically isolating the back contact with

Apiezon Type W wax. Before deposition, the n-Si(100) electrode was etched in 5% HF

for 20 s to give an H-Si surface. The electrode was pre-polarized at -1.5 $V_{Ag/AgCl}$ and

plunged into the electrolyte for 2 s, after which the potential was raised to -0.5 $V_{Ag/AgCl}$

and held until the desired thickness of Cu was achieved. A three electrode setup having a

platinum wire counter electrode and a $Ag/AgCl/KCl_{sat}$ reference electrode was utilized.

Deposition was carried out using either a Princeton Applied Research PARSTAT 2273 or

a Brinkmann PGSTAT 30 Autolab potentiostat.

Linear sweep voltammetry (LSV) was acquired at a 3 mm diameter copper coated gold rotating disk electrode (Metrohm Autolab RDE-2) at a rotation rate of 1000 RPM. The potential was scanned from an open circuit potential of about 0.0 $V_{Ag/AgCl}$ to -1.6 $V_{Ag/AgCl}$ at a scan rate of 25 mV/s.

Electrochemical quartz microbalance measurements (EQCM) were acquired with a Seiko EG&G quartz crystal analyzer QCA917. The quartz crystal resonator was a platinum sputtered 9 MHz AT-cut quartz crystal electrode having an active area of 0.2 cm^2.

Spectrophotometric determination of the Faradaic efficiency for Cu electrodeposition was accomplished using an Agilent 4200 MP-AES. The Cu content was determined by dissolving the deposited film in nitric acid and analyzing the resulting solution for Cu.

2.2 CHARACTERIZATION

X-ray diffraction data was acquired by a Philips X-Pert MRD x-ray diffractometer (XRD). 2θ scans were acquired using a 2-bounce hybrid monochromator (PW3147/00) with a 0.18° parallel plate collimator (PW3098/18) attached to a proportional detector (PW3011/20). Rocking curves were acquired with the same 2-bounce hybrid monochromator using a rocking curve diffracted beam optics (PW3120/60) in conjunction with the proportional detector. Pole figures were acquired using an adjustable crossed slits collimator (PW3084/62) with a 0.27° parallel plate collimator (PW3098/27) having a flat crystal monochromator (PW3121/00) attached to a proportional detector. Interface models were constructed using VESTA 3.4.0 software.

Transmission electron microscopy (TEM) was accomplished with a FEI Tecnai F20 TEM and FEI Tecnai F30 Twin TEM. The sample was cross-sectioned for TEM analysis by ion milling in a FEI Helios Nanolab 600 DualBeam microscope.

X-ray photoelectron spectroscopy (XPS) was accomplished using a Phi 5000 Versaprobe II with argon sputtering.

3. RESULTS & DISCUSSION

The electrolyte was examined by LSV to determine the potentials to apply for electrodeposition of Cu (Figure 1). An LSV of an electrolyte with Cu was compared to an electrolyte without Cu. In both LSVs regions II and III are present. Region II is due to proton reduction followed directly by water reduction in region III. However, the reduction in region I is present solely in the Cu containing electrolyte. Region I represents the reduction of Cu^{2+} to Cu^0 beginning very close to the standard reduction potential for Cu. There is also a slight increase in cathodic current around $-0.3V_{Ag/AgCl}$ due to the reduction of dissolved oxygen, which is seen in both solutions. Epitaxial deposition utilizes a short nucleation pulse in region III at -1.5 $V_{Ag/AgCl}$ for 2 s followed by growth of the film in region I at -0.5 $V_{Ag/AgCl}$. Ideally deposition of Cu films would occur at a potential within region III. This being analogous to gold deposition, where deposition occurs at a potential more negative than the Si oxidation, thereby preventing its oxidation.[9-11] However, unlike gold, Cu does not appear to grow on Si at such high overpotentials. This is evidenced by Figure 2A, which shows the 2θ scan for a Si electrode held at -1.5 $V_{Ag/AgCl}$ for an hour. Only the peaks corresponding to Si are observed.
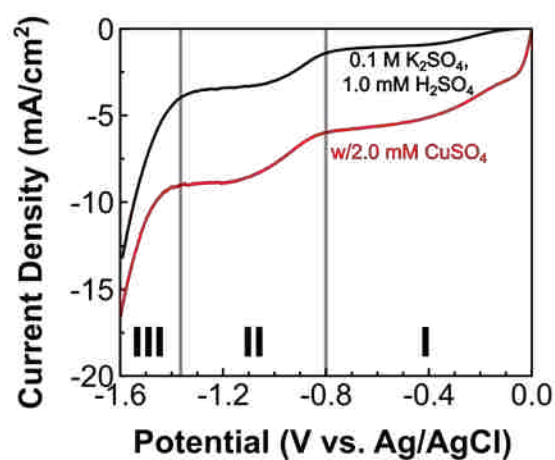
Figure 1. Linear sweep voltammagram of the electrolyte with (red) and without (black) Cu.
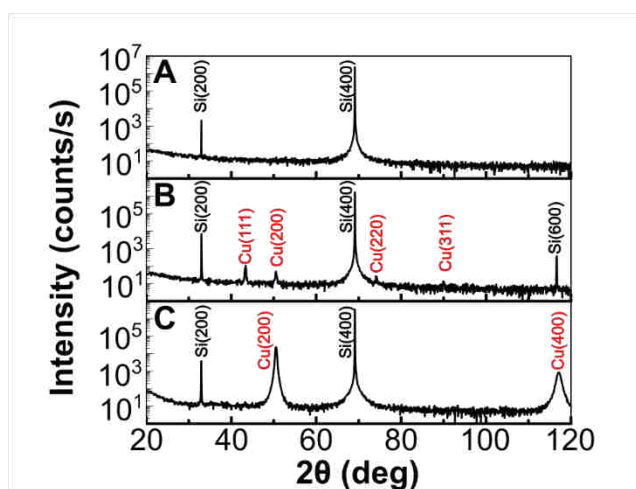
Figure 2. 2θ XRD pattern for deposition at -1.5 V for 1 hr (A), -0.5 V for 10 min (B), and stepped from -1.5 V for 2 s to -0.5 V for 10 min (C).

Epitaxial deposition was then attempted at -0.5 $V_{Ag/AgCl}$. The resulting Cu deposit was visually smooth and mirror like. However, as shown in Figure 2B, the film is polycrystalline giving all the major reflections for Cu. This was true even if the electrode

was pre-polarized before submerging into the electrolyte. Deposition at a Pt EQCM electrode gave similar results with very little deposition of Cu occurring at -1.5 $V_{Ag/AgCl}$, while significant deposition occurs at -0.5 $V_{Ag/AgCl}$ (See Figure S1 in the Supporting Information). The Cu which did deposit at -1.5$V_{Ag/AgCl}$ was powdery and adhered poorly, typical for a metal deposited at large overpotentials.[36] This phenomenon, where metal deposition is retarded or terminated at high overpotential, has been documented for Pt deposition as well. Moffat and co-workers describe this phenomenon and utilize this terminated growth to electrochemically grow Pt monolayer by monolayer.[37] They attribute the termination to a H_{UPD} blocking layer that forms on top of the deposited Pt.[37] Cu deposition may terminate in a similar manner. In addition, it is well documented that significant reconstruction occurs at a Cu electrode during H_2 evolution, due to H intercalation at the Cu surface.[38-40] Rearrangement and intercalation could also play a role in halting the further deposition of Cu. Regardless of the mechanism, deposition of Cu does not occur in region III. Finally, a two-step nucleation and growth method was developed, which gives epitaxial films of Cu(100) on Si(100). The two-step method utilizes a short 2s pulse at -1.5 $V_{Ag/AgCl}$ to nucleate the substrate, followed by growth at -0.5 $V_{Ag/AgCl}$. The epitaxial film grows with a [100] out-of-plane orientation as shown in the 2θ XRD pattern. (Figure 2C)

The Faradaic efficiency of this two-step method was measured based on the total charge passed versus the total Cu content within the film. The average Faradaic efficiency was 82.0%, giving a thickness of 300 nm of Cu for every 1 C/cm^2 of cathodic charge (see Table S1 in the Supporting Information) for a fully dense film. The in-plane ordering was probed with a (111) pole figure for both the Cu film and the Si substrate

(Figure 3). The Si(111) pole (Figure 3A) shows four intense spots at a tilt angle (χ) of

54°. This corresponds to the 4-fold symmetry of the (100) plane and the angle between

the (100) and (111) planes of 54.74°. The (111) pole figure of the Cu (Figure 3B) shows

this same 4-fold symmetric spot pattern at χ= 54° revealing that the Cu film (Figure 3B)

indeed grows epitaxially.
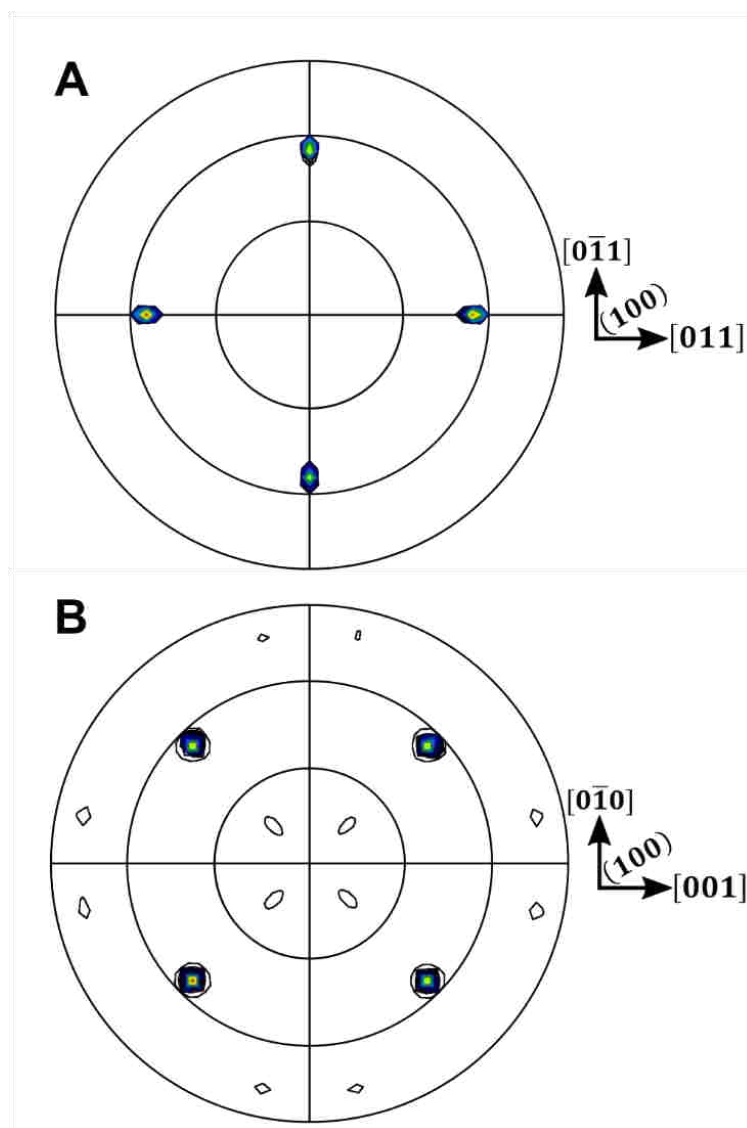
Figure 3. (111) pole figures for Si substrate (A) and Cu film (B). The concentric grid
lines on the pole figures correspond to 30° increments of the tilt angle, χ.

In addition to the 4 main intensity spots, four spots occur at $\chi = 15°$ and eight spots at $\chi = 77°$. These low intensity spots arise from a small amount of the $(\bar{1}22)$ orientation, which is the result of twinning along {111} slip planes. This type of twinning is a known phenomenon for face-centered-cubic metals,[41] and has been observed in vapor deposited Cu films as well.[1, 8] Chen et al. used the peak ratios within the pole figure to quantify the amount of twinning.[1] Following this analysis the electrochemically deposited Cu films shown here have a twinning of 0.9%, which is a nearly ten-fold reduction compared to the 8.2% twin ratio[1] found in the thermally evaporated film. Further description of twinning and its manifestation in the pole figures is described in the Supporting Information (Figure S2 in the Supporting Information)

Azimuthal scans were acquired by setting the 2θ equal to the (111) reflection for Si and Cu respectively and tilting to $\chi = 54.74°$ (Figure 4). The scans were then recorded as the sample was rotated from 0-360° azimuthally. By overlaying the Cu azimuthal with the Si azimuthal, it is clear that the Cu is rotated in-plane by 45° with respect to the Si substrate giving an epitaxial relationship of $Cu(100)[001] \parallel Si(100)[011]$. A simple graphical depiction of the 45° in-plane rotation is shown in Figure 4.

The rotational epitaxy can be explained by comparing the lattice match between an unrotated Cu lattice on a Si lattice versus that of a rotated Cu lattice (Figure 5). The mismatch between an unrotated lattice of Cu (100) and Si (100) is -33.43%, whereas for the 45° rotation the mismatch is reduced to -5.86%.
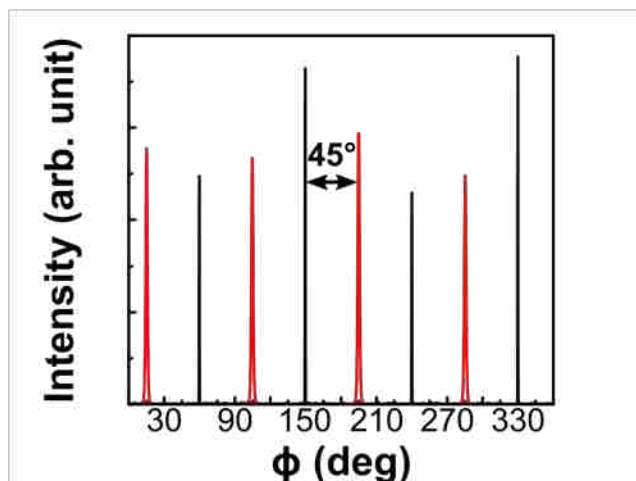
Figure 4. Azimuthal scan of Cu(111) (red) and Si(111) (black) at χ = 54.74° with graphical depiction showing the in-plane rotation.

Mismatch = -33.43%   Mismatch = -5.86%
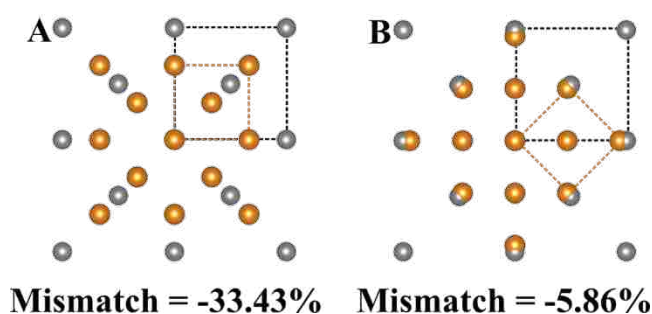
Figure 5. Interface models of Cu (100) (orange) on Si (100) (grey) with Cu rotated in plane by 0° (A) and 45° (B)6

Rocking curves on the Cu(200) were performed to quantify the mosaic spread (Figure 6). The standard deviation of the mosaic spread is related to the FWHM (full width at half maximum) of the rocking curve. For a Gaussian distributed rocking curve having $FWHM = 2\sqrt{2\ln(2)}\,\alpha$, where α is the standard deviation of the mosaic spread. Thus the sharper the peak, the lower the mosaic spread. As seen by other workers, the crystallinity improved with increasing Cu thickness.[7, 11] The FWHM for a 30 nm thick

film was 3.99°, whereas for a 160 nm thick film the FWHM was only 1.66°. While this

is much larger than the 0.018° measured FWHM (Figure S3 of Supporting Information)

for the Si substrate, it is comparable to Cu films made via vacuum techniques.[7]
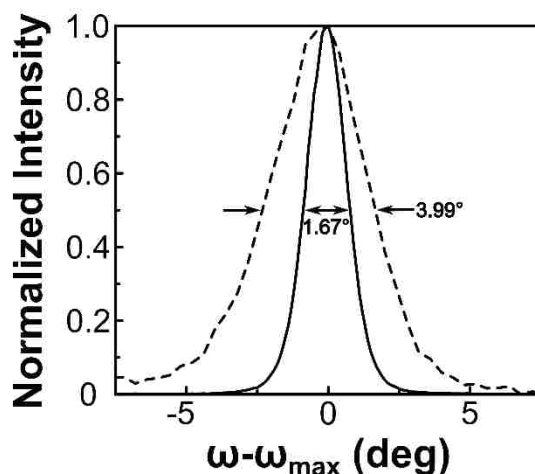
Figure 6. X-ray rocking curves of Cu(400) for a 160 nm thick film (solid) and a 30 nm
thick film (dashed).

A tilt scan from χ = 0-90° was performed at a 2θ of 43.298° (Figure S4 of

Supporting Information). As in the 2θ x-ray diffraction pattern, no discernible peak from

the Cu(111) reflection is observed. The Cu(111) reflection should manifest itself at χ =

0°. Only reflections from Cu(100) at χ = 53.9° and Cu($\bar{1}$22) at χ = 15.9° are apparent.

The FWHM of the Cu(100) reflection is 3.56°.

Cross sectional TEM was used to analyze the Cu film. The bright field image

(Figure 7A) shows a uniform film of Cu that is approximately 120 nm thick. The inset of

Figure 7A shows the combined electron diffraction patterns for the Cu film and Si

substrate. The pattern was taken by aligning the electron beam so that equal portions of

Cu and Si were probed. Figure 7B represents the convergent beam diffraction of only the

Cu film, whereas Figure 7C is the selected area diffraction pattern of the Si. A high resolution bright field image was acquired (Figure 7D), which allowed the measurement of the interplanar distance for both the deposited Cu and Si substrate. The measured values were 3.58 Å for the Cu and 5.44 Å for the Si. These values are in agreement with a [100] out-of-plane growth direction. The high resolution image also shows an approximately 2 nm thick amorphous layer separating the Cu from the Si (Figure 7D). The composition of the amorphous layer was probed using electron energy loss spectroscopy (EELS), as shown in Figure 7E. Cu is initially observed as the sample is scanned from top to bottom. As the scan crosses into the interfacial layer the Cu signal disappears, and a signal from both oxygen (O) and Si appear. As the scan continues through the interfacial layer and into the Si, the O signal disappears with Si remaining.

The presence of an oxide layer is corroborated by XPS depth profiling (Figure S5A of the Supporting Information). In addition, the XPS Si 2p spectrum (Figure S5B of the Supporting Information) shows the appearance and disappearance of a peak at a binding energy of 103.5 eV, corresponding to Si bonded with O. Thus there is definitely an interfacial SiO_x layer.

While an amorphous SiO_x interlayer is present, it is worth noting the data does not rule out the presence of a silicide. In the XPS depth profiling (Figure S5 in the Supporting Information) as well as the EELS spectrum (Figure 7E), signal from Cu appears through or at the tail end of the O signal. While this may be due to noise in the EELS spectrum or uneven milling in the XPS depth profiling, indications of a second interfacial layer between the SiO_x and the Si are also seen in the TEM micrographs.
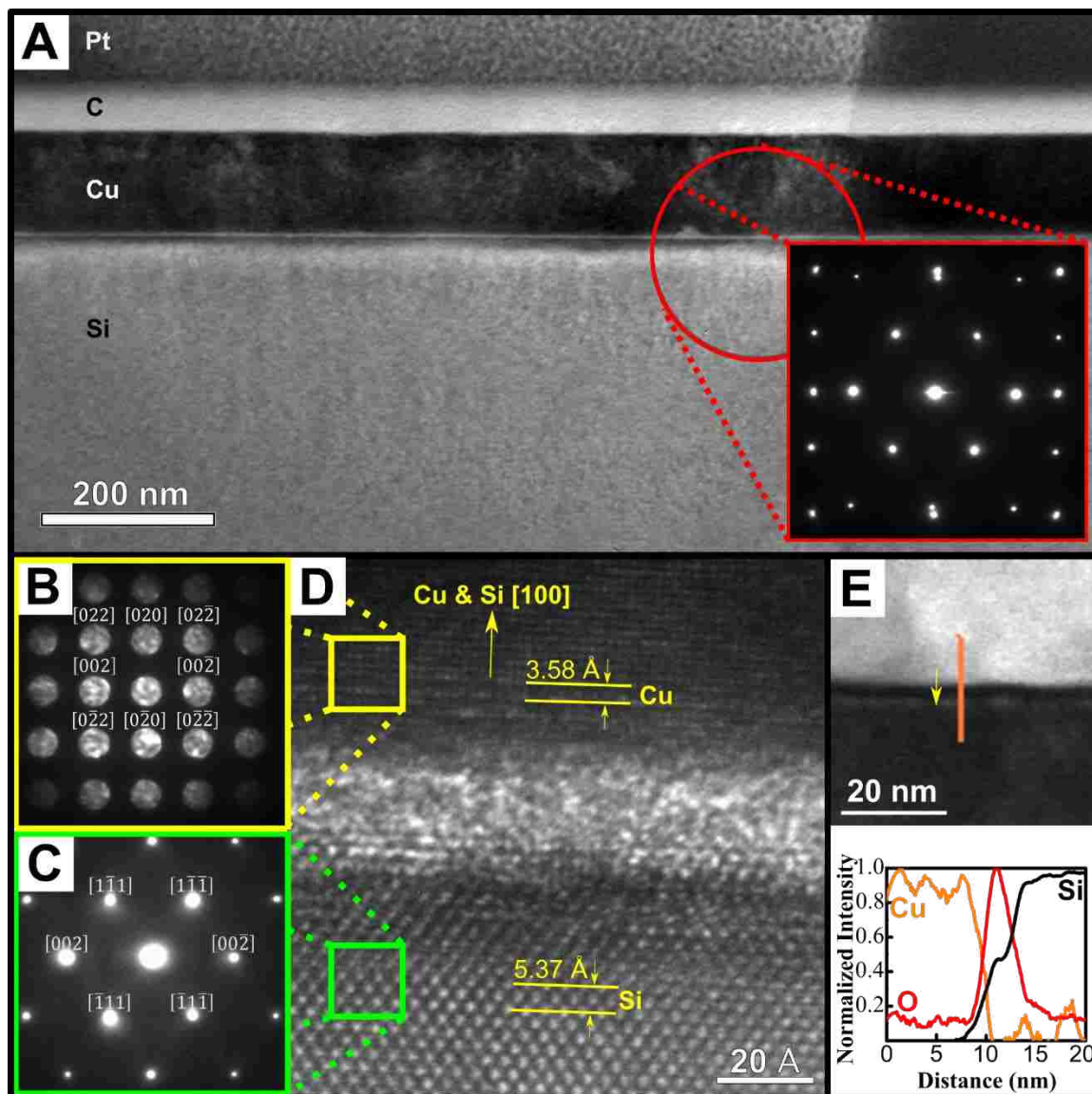
Figure 7. Bright field TEM cross-section of Cu film on Si (A) with corresponding selected area electron diffraction pattern (inset). Convergent beam diffraction pattern for Cu film along [100] zone axis (B). Selected area diffraction pattern of Si substrate along [110] zone axis (C). High resolution bright field image of the Cu and Si interface (D) HAADF STEM image of interface (top) with EELS line scan spectrum showing composition (bottom) (E).

In both the low resolution and high resolution bright field images (Figure 7A and D), as well as the HAADF image (Figure 7E) there is a region having a difference in contrast between the amorphous SiO_x layer and the bulk Si. This layer appears

crystalline in the high resolution bright field image, and may very well be a silicide, as is observed in some vacuum deposited Cu films.[2, 5, 8, 42] If it is a silicide, it is likely to have formed after deposition, as it is well known that Cu can diffuse rapidly through SiO_x and penetrate into Si.[43-45] This is why a Cu blocking layer of TiN is commonly deposited between Si and Cu in integrated circuit metallization.[46-48]

From the totality of the information presented, a proposed mechanism of epitaxial growth during this two potential step method has been developed. The mechanism is depicted in Figure 8 and described in the following. Under the initial 2 s pulse at -1.5 $V_{Ag/AgCl}$ the H-Si surface is protected from oxidation (Figure 8A and B), allowing the nucleation of epitaxial Cu seeds (Figure 8B). Growth of the seeds is quenched for a reason which necessitates further study, until the potential is raised to -0.5 V_{AgAgCl}. At this point two things occur simultaneously, the Si oxidizes forming a thin layer of SiO_x (Figure 8C), while the epitaxial Cu seeds grow (Figure 8C) eventually coalescing into an epitaxial film (Figure 8D). Growth and coalescence of the Cu film on top of the SiO_x is analogous to the epitaxial lateral overgrowth technique used in CVD[49] and liquid phase epitaxy processes.[50] Epitaxial lateral overgrowth reduces strain from lattice mismatch giving epitaxial films which have fewer number of dislocations and higher quality than those grown directly on the substrate.[50]

The interfacial oxide layer which forms during deposition is beneficial in that it allows for simple epitaxial lift-off of the Cu film to produce flexible single-crystal-like Cu foils. This is similar to our previous work on the epitaxial lift-off of gold foils.[51] Simply immersing the film in 5% HF for 30 s is sufficient to facilitate separation of the

film from the substrate, while still being adherent enough to allow rinsing, drying, and the attachment of an adhesive.
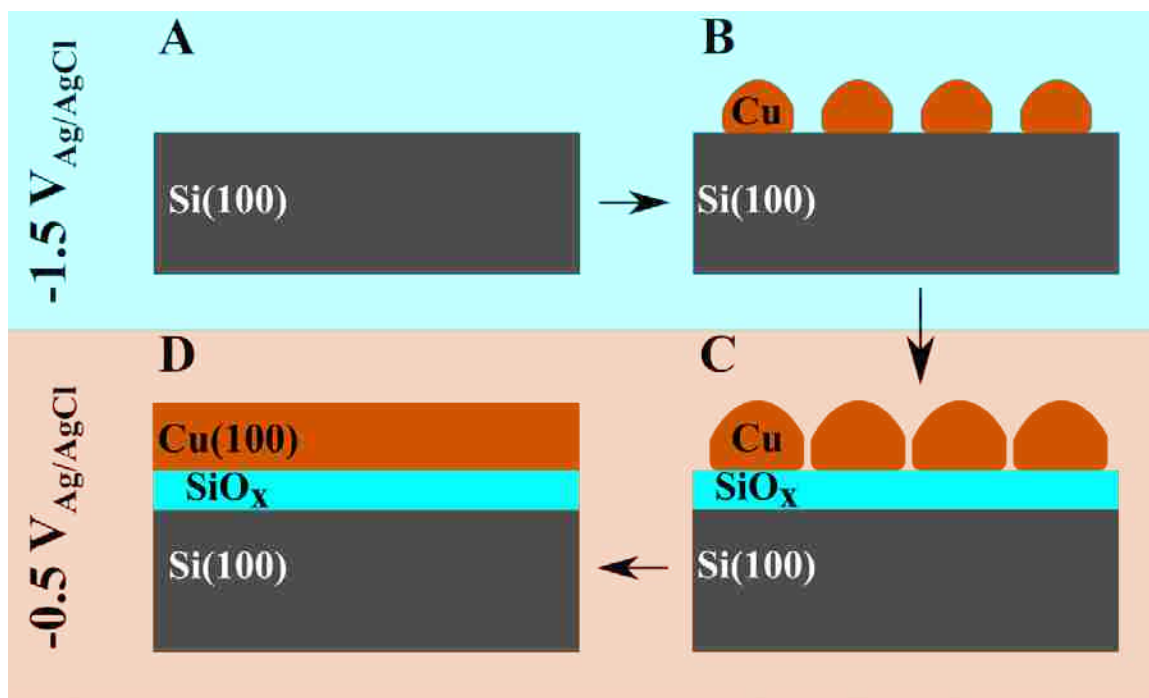
Figure 8. Schematic of proposed deposition mechanism. (A) Silicon pre-polarized at -1.5 $V_{Ag/AgCl}$ prior to deposition. (B) 2 s pulse at -1.5 $V_{Ag/AgCl}$ to deposit epitaxial Cu seeds without SiO_x formation. (C) Growth at -0.5 $V_{Ag/AgCl}$ causing rapid growth of ~2 nm thick SiO_x and lateral overgrowth of Cu. (D) Continued lateral overgrowth of Cu until coalescence and thickening of film under continued potentiostatic deposition.

The Cu film is then detached by peeling it away from the Si substrate (Figure 9A). The resultant single-crystal-like Cu foil has reflections solely from the {100} family in the 2θ diffraction pattern (Figure 9B), and the Cu(111) pole figure again shows four high intensity spots at $\chi = 54°$ from the Cu(100), each separated azimuthally by 90°. The low intensity spots at a tilt angle of $\chi = 16°$ and 78° (Figure 9C) are still observed, which

again are due to a small amount of twinning within the foil. The foils are flexible and could serve as versatile substrates, being highly ordered and electrically conductive.
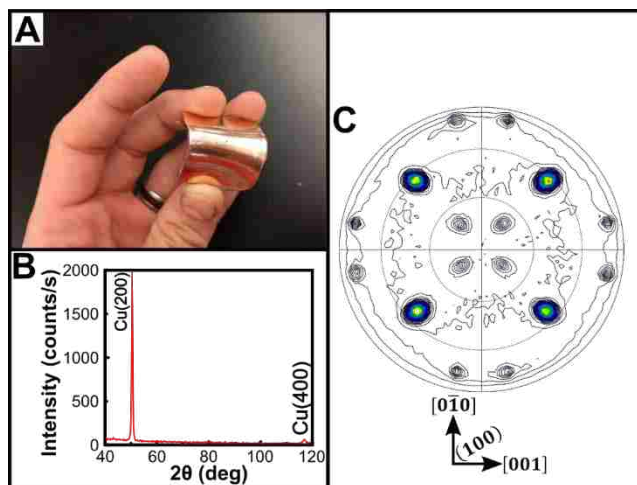
Figure 9. A 175 nm thick single-crystal-like Cu foil (A). 2Θ diffraction pattern (B) and pole figure (C) for the Cu single-crystal-like foil.

4. CONCLUSIONS

We have shown a simple two potential step electrodeposition method to produce epitaxial Cu(100) films on Si(100). Cu films grow with an epitaxial relationship of Cu(100)[001]||Si(100)[011]. Electrodeposition provides an alternative to vacuum deposition, and Cu films so produced may be used in comparable manner. In contrast to vacuum deposited films an amorphous SiO_x layer grows underneath the epitaxial film. This is beneficial in allowing Cu(100) foils to be lifted off. Foils having thicknesses from a few tens of nanometers to a half micron have been lifted off, with thickness depending solely on the charge passed during deposition. Cu(100) foils may prove to be a useful substrate for flexible electronics. Also, Cu films and foils give an active surface towards

galvanic replacement reactions.[52] In particular, platinum group elements desirable for catalysis can galvanically replace Cu yielding copper alloys or core shell type structures.[53-57] This opens interesting new avenues of research, for instance a thin film of Cu(100) on n-Si(100) could be decorated with Ir or Ru through galvanic replacement giving a highly active photoanode for water splitting. A Cu foil could also be converted giving a bimetallic foil. In addition the two-step potential method may be applicable for epitaxial electrodeposition of other metal films directly on Si, such as cobalt and nickel, which has thus far been absent in the literature.

ASSOCIATED CONTENT

EQCM measurements containing mass vs. time and current density vs. time plots, spectrophotometric determination of Cu content, stereographic projections and twin relationship, x-ray tilt scan at $2\theta = 43.298°$, Si(400) rocking curve, XPS depth profiling and Si 2p spectrum.

AUTHOR INFORMATION

Corresponding Author

*E-mail: jswitzer@mst.edu

Author Contributions

The manuscript was written through contributions of both authors. Both authors have given approval to the final version of the manuscript.

ACKNOWLEDGEMENTS

REFERENCES

1. Chen, L.; Andrea, L.; Timalsina, Y. P.; Wang, G.-C.; Lu, T.-M. Engineering Epitaxial-Nanospiral Metal Films Using Dynamic Oblique Angle Deposition. Cryst. Growth Des. **2013**, 13, 2075-2080. DOI: 10.1021/cg400142g

2. Hashim, I.; Park, B.; Atwater, H. A. Epitaxial Growth of Cu (001) on Si (001): Mechanisms of Orientation Development and Defect Morphology. Appl. Phys. Lett. **1993**, 63, 2833-2835. DOI: 10.1063/1.110302

3. Chang, C. A.; Liu, J. C.; Angilello, J. Epitaxy of (100)Cu on (100)Si by Evaporation Near Room Temperatures: In-Plane Epitaxial Relation and Channeling Analysis. Appl. Phys. Lett. **1990**, 57, 2239-2240. DOI: 10.1063/1.103902

4. Demczyk, B. G.; Naik, R.; Auner, G.; Kota, C.; Rao, U. Growth of Cu Films on Hydrogen Terminated Si(100) and Si(111) Surfaces. J. Appl. Phys. **1994**, 75, 1956-1961. DOI: 10.1063/1.356344

5. Meunier, A.; Gilles, B.; Verdier, M. Cu/Si(001) Epitaxial Growth: Role of the Epitaxial Silicide Formation in the Structure and the Morphology. J. Cryst. Growth **2005**, 275, e1059-e1065. DOI: 10.1016/j.jcrysgro.2004.11.132

6. Lukaszew, R. A.; Sheng, Y.; Uher, C.; Clarke, R. Smoothening of Cu Films Grown on Si(001). Appl. Phys. Lett. **2000**, 76, 724-726. DOI: 10.1063/1.125874

7. Jiang, H.; Klemmer, T. J.; Barnard, J. A.; Payzant, E. A. Epitaxial Growth of Cu on Si by Magnetron Sputtering. J. Vac. Sci. Technol., A **1998**, 16, 3376-3383. DOI: 10.1116/1.581489

8. Cemin, F.; Lundin, D.; Furgeaud, C.; Michel, A.; Amiard, G.; Minea, T.; Abadias, G. Epitaxial Growth of Cu(001) Thin Films onto Si(001) Using a Single-Step HiPIMS Process. Sci. Rep. **2017**, 7, 1655. DOI: 10.1038/s41598-017-01755-8

9. Warren, S.; Prod'homme, P.; Maroun, F.; Allongue, P.; Cortès, R.; Ferrero, C.; Lee, T. L.; Cowie, B. C. C.; Walker, C. J.; Ferrer, S.; Zegenhagen, J. Electrochemical Au Deposition on Stepped Si(111)-H Surfaces: 3D Versus 2D Growth Studied by AFM and X-Ray Diffraction. Surf. Sci. **2009**, 603, 1212-1220. DOI: 10.1016/j.susc.2009.03.004

10. Prod'homme, P.; Maroun, F.; Cortès, R.; Allongue, P. Electrochemical Growth of Ultraflat Au(111) Epitaxial Buffer 6Layers on H–Si(111). Appl. Phys. Lett. **2008**, 93, 171901. DOI: 10.1063/1.3006064

11. Switzer, J. A.; Hill, J. C.; Mahenderkar, N. K.; Liu, Y.-C. Nanometer-Thick Gold on Silicon as a Proxy for Single-Crystal Gold for the Electrodeposition of Epitaxial Cuprous Oxide Thin Films. ACS Appl. Mater. Interfaces **2016**, 8, 15828-15837. DOI: 10.1021/acsami.6b04552

12. Chang, C. A. Magnetocrystalline Anisotropy of (100) Face-Centered Cubic Co Structures Deposited on Cu/Si(100). Appl. Phys. Lett. **1991**, 58, 1745-1747. DOI: 10.1063/1.105127

13. Frisk, A.; Ali, H.; Svedlindh, P.; Leifer, K.; Andersson, G.; Nyberg, T. Composition, Structure and Magnetic Properties of Ultra-Thin Fe/Ni Multilayers Sputter Deposited on Epitaxial Cu/Si(001). Thin Solid Films **2018**, 646, 117-125. DOI: 10.1016/j.tsf.2017.11.023

14. Castaner, R.; Prieto, C.; Andres, A. d.; Martinez, J. L.; Martinez-Albertos, J. L.; Ocal, C.; Miranda, R. The Structural Characterization of Co-Cu(100) Superlattices by X-Ray Absorption Spectroscopy. J. Phys.: Condens. Matter **1994**, 6, 4981-4990. DOI: 10.1088/0953-8984/6/27/007

15. Cebollada, A.; Gallego, J. M.; de Miguel, J. J.; Miranda, R.; Martinez, J. L.; Ferrer, S.; Fillion, G.; Rebouillat, J. P. Epitaxial Growth of Metals: from Monolayer to Superlattice. Vacuum **1990**, 41, 482-484. DOI: 10.1016/0042-207X(90)90391-B

16. Cebollada, A.; Martnez, J. L.; Gallego, J. M.; de Miguel, J. J.; Miranda, R.; Ferrer, S.; Batallán, F.; Fillion, G.; Rebouillat, J. P. Antiferromagnetic Ordering in Co-Cu Single-Crystal Superlattices. Phys. Rev. B **1989**, 39, 9726-9729. DOI: 10.1103/PhysRevB.39.9726

17. Nabiyouni, G.; Schwarzacher, W. Dependence of GMR on Crystal Orientation in Electrodeposited Co–Ni–Cu/Cu Superlattices. J. Magn. Magn. Mater. **1996**, 156, 355-356. DOI: 10.1016/0304-8853(95)00896-9

18. Kashima, N.; Shima, K.; Doi, T.; Kubota, S.; Watanabe, T.; Inoue, M.; Kiss, T.; Nagaya, S. Development of Cu Substrate for Low Cost Coated Conductors. IEEE Trans. Appl. Supercond. **2009**, 19, 3299-3302. DOI: 10.1109/TASC.2009.2018263

19. Shima, M.; Salamanca-Riba, L. G.; McMichael, R. D.; Moffat, T. P. Correlation Between Structural Imperfection and Giant Magnetoresistance in Electrodeposited Co/Cu Multilayers. J. Electrochem. Soc. **2001**, 148, C518-C523. DOI: 10.1149/1.1379948

20. Piñol, S.; Díaz, J.; Segarra, M.; Espiell, F. Preparation of Biaxially Cube Textured Cu Substrate Tapes for HTS Coated Conductor Applications. Supercond. Sci. Technol. **2001**, 14, 11-15. DOI: 10.1088/0953-2048/14/1/303

21. Zhou, Y. X.; Sun, L.; Chen, X.; Fang, H.; Putman, P. T.; Salama, K. The Manufacturing of an Electroplated Ni Layer on Textured Cu Substrate for Cu-Based HTS Coated Conductors. Supercond. Sci. Technol. **2005**, 18, 107-111. DOI: 10.1088/0953-2048/18/1/017

22. Hori, Y.; Murata, A.; Takahashi, R. Formation of Hydrocarbons in the Electrochemical Reduction of Carbon Dioxide at a Copper Electrode in Aqueous Solution. J. Chem. Soc., Faraday Trans. 1 **1989**, 85, 2309-2326. DOI: 10.1039/F19898502309

23. Peterson, A. A.; Abild-Pedersen, F.; Studt, F.; Rossmeisl, J.; Norskov, J. K. How Copper Catalyzes the Electroreduction of Carbon Dioxide into Hydrocarbon Fuels. Energy Environ. Sci. **2010**, 3, 1311-1315. DOI: 10.1039/C0EE00071J

24. Reske, R.; Mistry, H.; Behafarid, F.; Roldan Cuenya, B.; Strasser, P. Particle Size Effects in the Catalytic Electroreduction of CO_2 on Cu Nanoparticles. J. Am. Chem. Soc. **2014**, 136, 6978-6986. DOI: 10.1021/ja500328k

25. Hahn, C.; Hatsukade, T.; Kim, Y.-G.; Vailionis, A.; Baricuatro, J. H.; Higgins, D. C.; Nitopi, S. A.; Soriaga, M. P.; Jaramillo, T. F. Engineering Cu Surfaces for the Electrocatalytic Conversion of CO_2: Controlling Selectivity Toward Oxygenates and Hydrocarbons. Proc. Natl. Acad. Sci. U. S. A. **2017**, 114, 5918-5923. DOI: 10.1073/pnas.1618935114

26. Montoya, J. H.; Shi, C.; Chan, K.; Nørskov, J. K. Theoretical Insights into a CO Dimerization Mechanism in CO_2 Electroreduction. J. Phys. Chem. Lett. **2015**, 6, 2032-2037. DOI: 10.1021/acs.jpclett.5b00722

27. Schouten, K. J. P.; Qin, Z.; Pérez Gallent, E.; Koper, M. T. M. Two Pathways for the Formation of Ethylene in CO Reduction on Single-Crystal Copper Electrodes. J. Am. Chem. Soc. **2012**, 134, 9864-9867. DOI: 10.1021/ja302668n

28. Palomino, R. M.; Ramírez, P. J.; Liu, Z.; Hamlyn, R.; Waluyo, I.; Mahapatra, M.; Orozco, I.; Hunt, A.; Simonovis, J. P.; Senanayake, S. D.; Rodriguez, J. A. Hydrogenation of CO_2 on ZnO/Cu(100) and ZnO/Cu(111) Catalysts: Role of Copper Structure and Metal–Oxide Interface in Methanol Synthesis. J. Phys. Chem. B **2018**, 122, 794-800. DOI: 10.1021/acs.jpcb.7b06901

29. Goyal, A. K.; Budai, J.D.; Kroeger, D. M.; Norton, D. P.; Specht, E. D.; Christen, D. K. Structures Having Enhanced Biaxial Texture and Method of Fabricating Same. U.S. Patent 5741377, **1998**.

30. Bhuiyan, M. S.; Paranthaman, M.; Sathyamurthy, S.; Aytug, T.; Kang, S.; Lee, D. F.; Goyal, A.; Payzant, E. A.; Salama, K. MOD Approach for the Growth of Epitaxial CeO_2 Buffer Layers on Biaxially Textured Ni–W Substrates for YBCO Coated Conductors. Supercond. Sci. Technol. **2003**, 16, 1305-1309. DOI: 10.1088/0953-2048/16/11/009

31. He, Q.; Christen, D. K.; Budai, J. D.; Specht, E. D.; Lee, D. F.; Goyal, A.; Norton, D. P.; Paranthaman, M.; List, F. A.; Kroeger, D. M. Deposition of Biaxially-Oriented Metal and Oxide Buffer-Layer Films on Textured Ni Tapes: New Substrates for High-Current, High-Temperature Superconductors. Phys. C (Amsterdam, Neth.) **1997**, 275, 155-161. DOI: 10.1016/S0921-4534(96)00705-8

32. Paranthaman, M.; Goyal, A.; List, F. A.; Specht, E. D.; Lee, D. F.; Martin, P. M.; He, Q.; Christen, D. K.; Norton, D. P.; Budai, J. D.; Kroeger, D. M. Growth of Biaxially Textured Buffer Layers on Rolled-Ni Substrates by Electron Beam Evaporation. Phys. C (Amsterdam, Neth.) **1997**, 275, 266-272. DOI: 10.1016/S0921-4534(96)00713-7

33. Norton, D. P.; Goyal, A.; Budai, J. D.; Christen, D. K.; Kroeger, D. M.; Specht, E. D.; He, Q.; Saffian, B.; Paranthaman, M.; Klabunde, C. E.; Lee, D. F.; Sales, B. C.; List, F. A. Epitaxial $YBa_2Cu_3O_7$ on Biaxially Textured Nickel (001): An Approach to Superconducting Tapes with High Critical Current Density. Science **1996**, 274, 755-757. DOI: 10.1126/science.274.5288.755

34. Kang, S.; Goyal, A.; Li, J.; Gapud, A. A.; Martin, P. M.; Heatherly, L.; Thompson, J. R.; Christen, D. K.; List, F. A.; Paranthaman, M.; Lee, D. F. High-Performance High-T_c Superconducting Wires. Science **2006**, 311, 1911-1914. DOI: 10.1126/science.1124872

35. Goyal, A.; Norton, D. P.; Paranthaman, M.; Specht, E. D.; He, Q.; List, F. A.; Kroeger, D. M.; Christen, D. K.; Budai, J. D. Low Cost, Single Crystal-Like Substrates for Practical, High Efficiency Solar Cells. AIP Conf. Proc. **1997**, 404, 377-394. DOI: 10.1063/1.53462

36. Nikolić, N. D.; Popov, K. I. Electrodeposition of Copper Powders and Their Properties. In Electrochemical Production of Metal Powders, Djokić, S. S., Ed. Springer US: Boston, MA, **2012**; pp 125-185. DOI: 10.1007/978-1-4614-2380-5_3

37. Liu, Y.; Gokcen, D.; Bertocci, U.; Moffat, T. P. Self-Terminating Growth of Platinum Films by Electrochemical Deposition. Science **2012**, 338, 1327-1330. DOI: 10.1126/science.1228925

38. Hellman, A.; Svensson, K.; Andersson, S. Hydrogen-Induced Reconstruction of Cu(100): Two-Dimensional and One-Dimensional Structures of Surface Hydride. J. Phys. Chem. C **2014**, 118, 15773-15778. DOI: 10.1021/jp5035147

39. Matsushima, H.; Taranovskyy, A.; Haak, C.; Gründer, Y.; Magnussen, O. M. Reconstruction of Cu(100) Electrode Surfaces during Hydrogen Evolution. J. Am. Chem. Soc. **2009**, 131, 10362-10363. DOI: 10.1021/ja904033t

40. Trung, H. T. M.; Peter, B. From In Situ towards In Operando Conditions: Scanning Tunneling Microscopy Study of Hydrogen Intercalation in Cu(111) during Hydrogen Evolution. ChemElectroChem **2014**, 1, 1271-1274. DOI: 10.1002/celc.201402147

41. Kibey, S.; Liu, J. B.; Johnson, D. D.; Sehitoglu, H., Predicting Twinning Stress in FCC Metals: Linking Twin-Energy Pathways to Twin Nucleation. Acta Mater. **2007**, 55 (20), 6843-6851. DOI: 10.1016/j.actamat.2007.08.042

42. Chang, C. A. Formation of Copper Silicides from Cu(100)/Si(100) and Cu(111)/Si(111) Structures. J. Appl. Phys. **1990**, 67, 566-569. DOI: 10.1063/1.345194

43. Shacham-Diamand, Y.; Dedhia, A.; Hoffstetter, D.; Oldham, W. G., Copper Transport in Thermal SiO_2. J. Electrochem. Soc. **1993**, 140 (8), 2427-2432. DOI: 10.1149/1.2220837

44. Zelený, M.; Hegedüs, J.; Foster, A. S.; Drabold, D. A.; Elliott, S. R.; Nieminen, R. M., Ab Initio Study of Cu Diffusion in α -Cristobalite. New J. Phys. **2012**, 14 (11), 113029. DOI: 10.1088/1367-2630/14/11/113029

45. Tappertzhofen, S.; Menzel, S.; Valov, I.; Waser, R., Redox Processes in Silicon Dioxide Thin Films Using Copper Microelectrodes. Appl. Phys. Lett. **2011**, 99 (20), 203103. DOI: 10.1063/1.3662013

46. Baumann, J.; Werner, T.; Ehrlich, A.; Rennau, M.; Kaufmann, C.; Gessner, T., TiN Diffusion Barriers for Copper Metallization. Microelectron. Eng. **1997**, 37-38, 221-228. DOI: 10.1016/S0167-9317(97)00115-9

47. Bochkarev, A. S.; Popov, M. N.; Razumovskiy, V. I.; Spitaler, J.; Puschnig, P., Ab Initio Study of Cu Impurity Diffusion in Bulk TiN. Phys. Rev. B **2016**, 94 (10), 104303. DOI: 10.1103/PhysRevB.94.104303

48. Kwak, M. Y.; Shin, D. H.; Kang, T. W.; Kim, K. N., Characteristics of TiN Barrier Layer Against Cu Diffusion. Thin Solid Films **1999**, 339 (1), 290-293. DOI: 10.1016/S0040-6090(98)01074-8

49. Jastrzebski, L., SOI by CVD: Epitaxial Lateral Overgrowth (ELO) Process—Review. J. Crys. Growth **1983**, 63 (3), 493-526. DOI: 10.1016/0022-0248(83)90164-1

50. Zytkiewicz, Z. R., Epitaxial Lateral Overgrowth of Semiconductors. In Springer Handbook of Crystal Growth, Dhanaraj, G.; Byrappa, K.; Prasad, V.; Dudley, M., Eds. Springer Berlin Heidelberg: Berlin, Heidelberg, **2010**; pp 999-1039. DOI: 10.1007/978-3-540-74761-1_30

51. Mahenderkar, N. K.; Chen, Q.; Liu, Y-C.; Duchild, A. R.; Hofheins, S.; Chason, E.; Switzer, J. A. Epitaxial Lift-Off of Electrodeposited Single-Crystal Gold Foils for Flexible Electronics. Science **2017**, 355, 1203-1206. DOI: 10.1126/science.aam5830

52. Xia, X.; Wang, Y.; Ruditskiy, A.; Xia, Y. 25th Anniversary Article: Galvanic Replacement: A Simple and Versatile Route to Hollow Nanostructures with Tunable and Well-Controlled Properties. Advanced Materials **2013**, 25, 6313-6333. DOI: 10.1002/adma.201302820

53. Du, C.; Chen, M.; Wang, W.; Tan, Q.; Xiong, K.; Yin, G. Platinum-Based Intermetallic Nanotubes with a Core–Shell Structure as Highly Active and Durable Catalysts for Fuel Cell Applications. J. Power Sources **2013**, 240, 630-635. DOI: 10.1016/j.jpowsour.2013.05.023

54. Gilroy, K. D.; Farzinpour, P.; Sundar, A.; Hughes, R. A.; Neretina, S. Sacrificial Templates for Galvanic Replacement Reactions: Design Criteria for the Synthesis of Pure Pt Nanoshells with a Smooth Surface Morphology. Chem. Mater. **2014**, 26, 3340-3347. DOI: 10.1021/cm501418d

55. Mohl, M.; Dobo, D.; Kukovecz, A.; Konya, Z.; Kordas, K.; Wei, J.; Vajtai, R.; Ajayan, P. M. Formation of CuPd and CuPt Bimetallic Nanotubes by Galvanic Replacement Reaction. J. Phys. Chem. C **2011**, 115, 9403-9409. DOI: 10.1021/jp112128g

56. Park, D. Y.; Jung, H. S.; Rheem, Y.; Hangarter, C. M.; Lee, Y.-I.; Ko, J. M.; Choa, Y. H.; Myung, N. V. Morphology Controlled 1D Pt Nanostructures Synthesized by Galvanic Displacement of Cu Nanowires in Chloroplatinic Acid. Electrochim. Acta **2010**, 55, 4212-4216. DOI: 10.1016/j.electacta.2010.02.054

57. Stewart, I. E.; Ye, S.; Chen, Z.; Flowers, P. F.; Wiley, B. J. Synthesis of Cu–Ag, Cu–Au, and Cu–Pt Core–Shell Nanowires and Their Use in Transparent Conducting Films. *Chem. Mater.* **2015**, 27, 7788-7794. DOI: 10.1021/acs.chemmater.5b03709

SUPPORTING INFORMATION

ELECTRODEPOSITED EPITAXIAL Cu(100) ON Si(100) AND LIFT-OFF OF SINGLE-CRYSTAL-LIKE Cu(100) FOILS

Caleb M. Hull and Jay A. Switzer*

Missouri University of Science and Technology, Department of Chemistry and Graduate Center for Materials Research, Rolla, MO 65409-1170, USA

*Corresponding author:– jswitzer@mst.edu

CONTENTS:

Figure S1: Current density vs. time for deposition of Cu on 0.2 cm^2 Pt EQCM at -1.5 V$_{Ag/AgCl}$ (black) and two potential method (red) with corresponding mass change.

The mass change versus deposition time (top) was measured using a Pt EQCM. This is compared to the current density versus time (bottom). Very little mass change is recorded at a deposition potential of -1.5 V$_{Ag/AgCl}$ (black) even though a much larger amount of current is flowing. This is contrasted with the two step nucleation and growth method (red), where there is a linear increase in mass during growth at a deposition potential of -0.5 V$_{Ag/AgCl}$.

Table S1: Spectrophotometric results for copper films grown at various deposition times and their resultant Faradaic efficiency.

Deposition Time (minutes)	Charge (C)	Cu Theoretical (g)	Cu Experimental (g)	Faradaic Efficiency
2	0.04696	1.55×10^{-5}	1.33×10^{-5}	85.8%
4	0.1138	3.75×10^{-5}	3.07×10^{-5}	81.9%
6	0.1619	5.33×10^{-5}	4.26×10^{-5}	79.9%
8	0.2910	9.58×10^{-5}	7.59×10^{-5}	79.2%
10	0.3090	1.02×10^{-4}	8.47×10^{-5}	83.0%
Average Faradaic Efficiency: 82.0% $\pm$ 2.6%				

Samples of various deposition lengths were deposited on silicon. The copper was dissolved away from the silicon using concentrated HNO_3 and weighed in a flask. The silicon electrode was quantitatively rinsed and the total mass of the resultant solution was measured. The solution was analyzed for total Cu content using a microwave plasma atomic emission spectrophotometer. The experimentally measured Cu content was compared to the mass assuming 100% efficiency of charge to Cu metal.

It is well known that FCC metals twin along the {111} slip planes. When such twinning occurs in an epitaxial film having a (100) out-of-plane orientation, the out-of-plane orientation of the twin is $(\bar{1}22)$. This can be calculated using the twinning relationship for cubic systems
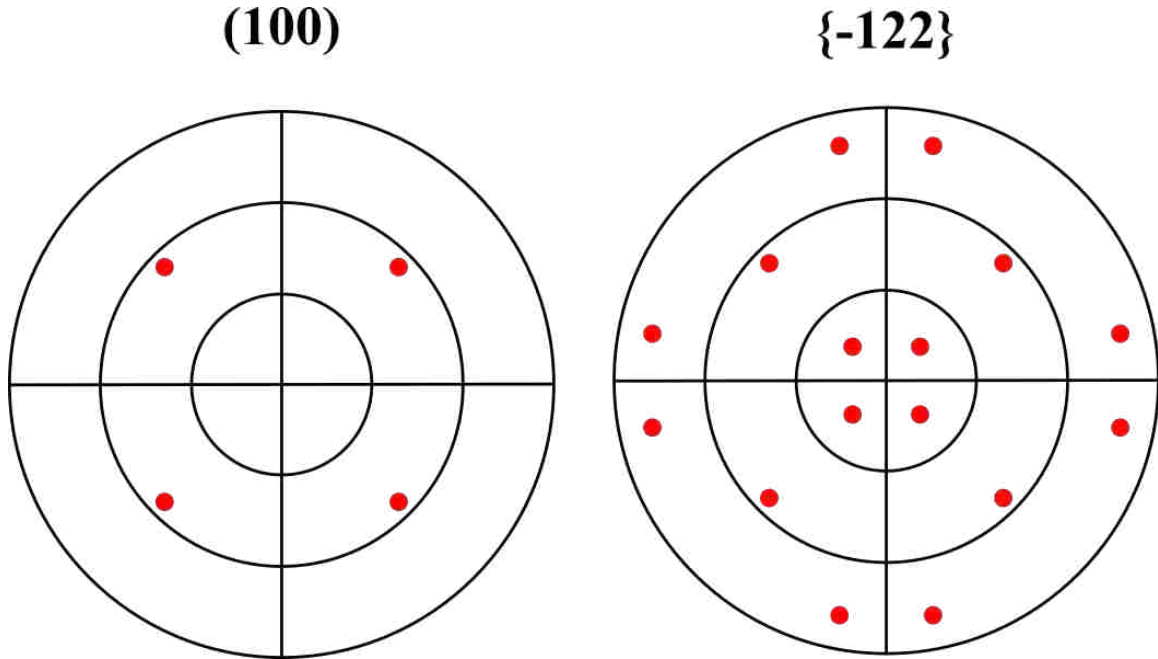
Figure S2 Stereographic Projection for (111) pole of material having (100) or ($\bar{1}$22) out-of-plane orientation.

$$(PQR) = T_{(hkl)}(pqr) \tag{1}$$

where (PQR) is a column matrix for the lattice plane in a twinned crystallite which corresponds to the lattice plane (pqr) of the original crystallite after twinning on (hkl). The general twin matrix for cubic systems is

$$T_{(hkl)} = \left(\frac{1}{h^2+k^2+l^2}\right)\begin{pmatrix} h^2 - k^2 - l^2 & 2hk & 2hl \\ 2hk & -h^2 + k^2 - l^2 & 2kl \\ 2hl & 2kl & -h^2 - k^2 + l^2 \end{pmatrix} \tag{2}$$

Applying the knowledge that twinning occurs along (111) slip planes, the twinning matrix becomes

$$T_{(111)} = \left(\frac{1}{3}\right) \begin{pmatrix} -1 & 2 & 2 \\ 2 & -1 & 2 \\ 2 & 2 & -1 \end{pmatrix} \tag{3}$$

The twin relationship then becomes

$$(pqr) = (300); (PQR) = (\bar{1}22) \tag{4}$$

The stereographic projections for a (111) pole figure of a film having an out-of-plane

orientation is shown on the left, while the ($\bar{1}$22) twin is on the right. The highest

intensity peaks in the experimental pole figure match to the (100) orientation, while the

low intensity peaks match to the twin orientation ($\bar{1}$22).
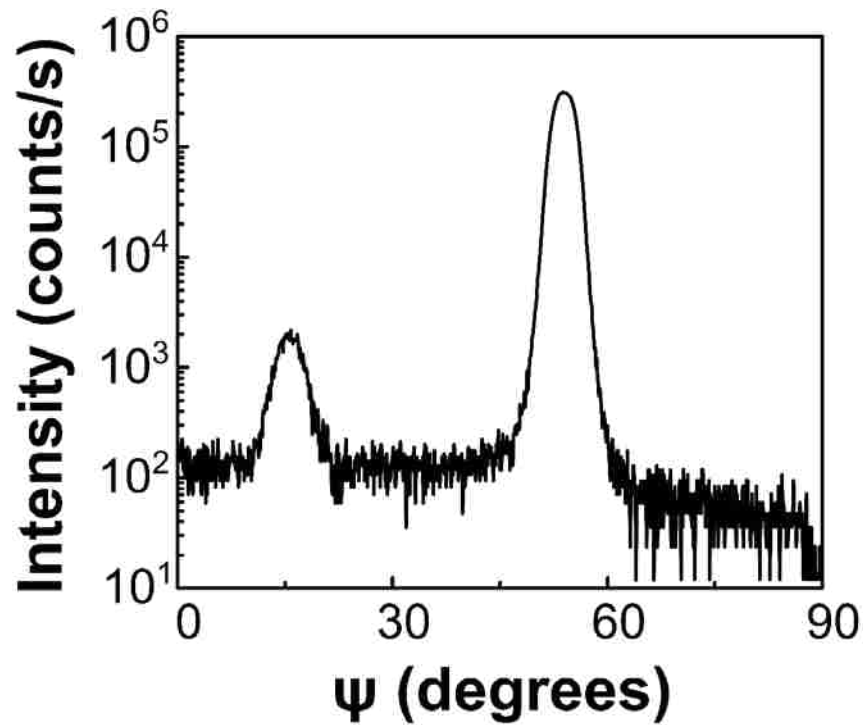
Figure S3: X-ray tilt scan of copper film at $2\theta = 43.298°$ and $\varphi = 45°$

X-ray tilt scan acquired by setting 2θ = Cu(111) reflection, φ = 45° and tilting the sample along χ from 0-90°. Two peaks are observed one at χ = 15.9° from the Cu($\bar{1}$22) twin and χ = 53.9° from the Cu(100).
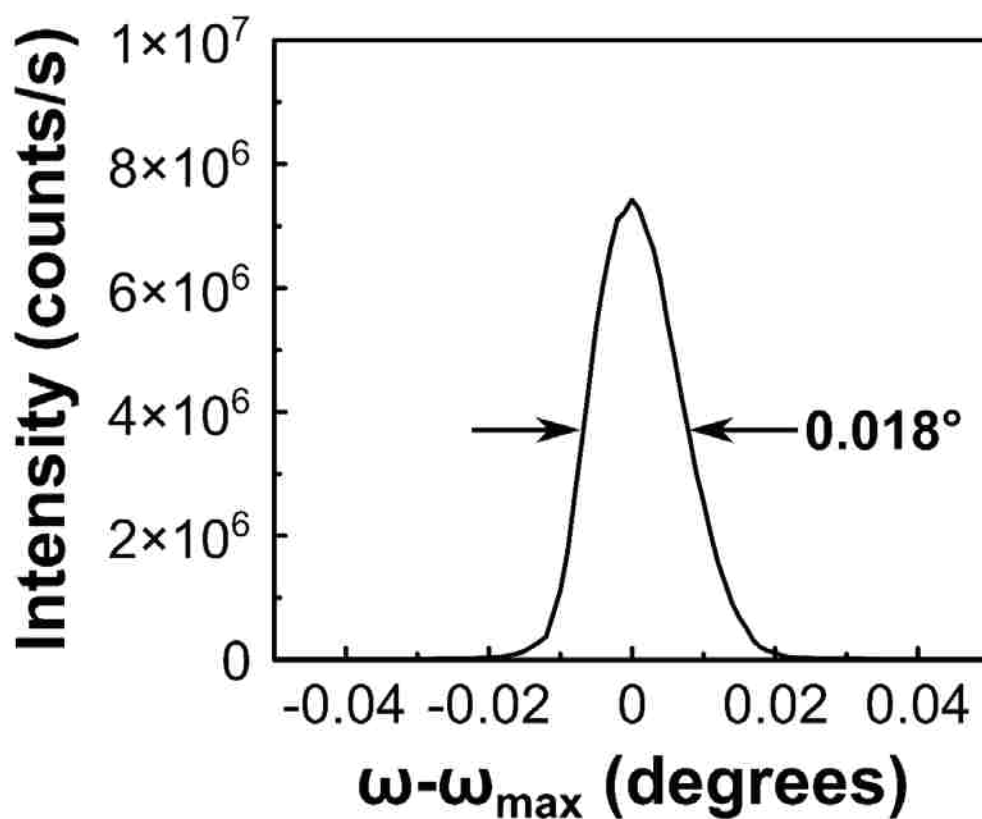
Figure S4: X-ray rocking curve of Si(400).

X-ray rocking curve for the single crystal n-Si(100) substrate. The peak is extremely sharp having a FWHM of 0.018°, determined by the instrumental broadening of the instrument due to the divergence of the x-ray beam.
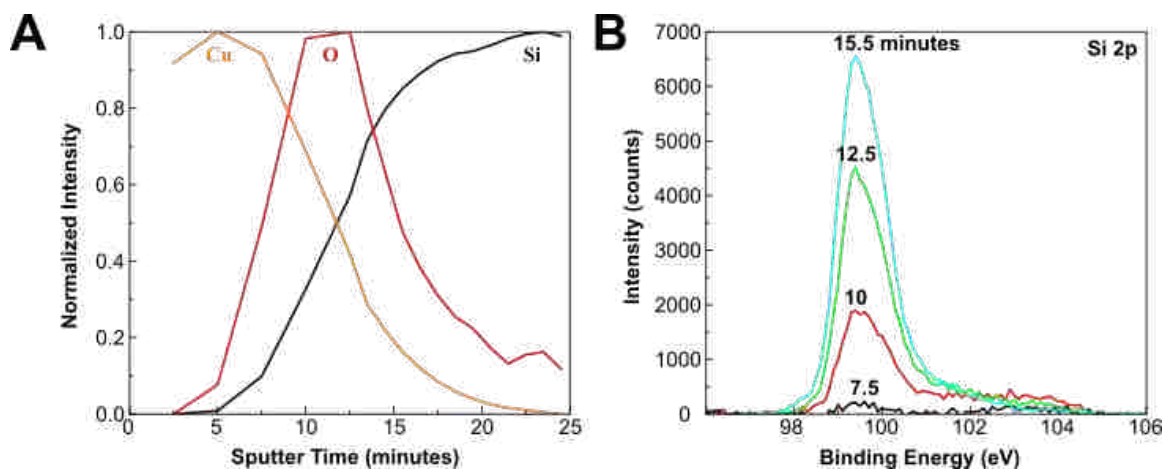
Figure S5: XPS Depth profiling of approximately 30 nm film of Cu(100) on Si(100).

XPS depth profiling was performed on an approximately 30 nm thick film of Cu on Si. The normalized intensity for Cu, O, and Si are shown in A. An obvious oxide layer is present between the Cu and bulk Si. Figure S5B shows the Si 2p spectrum as a function of sputter time. Elemental Si has a binding energy of 99.8 eV whereas SiO_2 has a binding energy of 103.8 eV. The rise and fall of intensity for the Si-O peak corresponds to the rise and fall in the presence of O. Therefore, a SiO_x interlayer is present.

SECTION

2. CONCLUSION

Electrodeposition is a powerful technique for inorganic material synthesis, particularly well suited in the deposition of conformal thin films on conductive substrates. As a standalone method, electrodeposition is shown to be useful in the deposition of thin ceramic films of $Co(OH)_2$ on Ti and Au substrates, as well as Cu metal films directly on Si . Conditions for epitaxial growth of $Co(OH)_2$ on Au(100), Au(110), and Au(111) are given as well as conditions for epitaxial growth of Cu(100) on Si(100). Epitaxial films lack grain boundaries and should have improved electron transport over polycrystalline films. Better electron transport should give increased efficiencies in electronic devices as well as catalysis. Electrodeposited epitaxial films of $Co(OH)_2$ were converted through thermal and electrochemical methods. Converted films retained their epitaxy even through large structure changes. During conversion films developed cracks and pores resulting in increased surface area. Thus, ordered materials of high surface area are obtainable through secondary processing steps.

Paper I demonstrates an electrochemical reduction procedure for deposition of β-$Co(OH)_2$. Co^{3+} is complexed with ethylenediamine to form a complex that is stable in 2M NaOH. Reduction of $[Co(en)_3]^{3+}$ to $[Co(en)_3]^{2+}$ causes the destabilization of the complex and precipitation of $Co(OH)_2$ at the electrode. $Co(OH)_2$ was deposited on Ti, demonstrating the simple synthesis of an anode suitable for water electrolysis. An anode so produced was characterized by LSVs in 1M KOH, and showed similar current-voltage

response to a Co_3O_4 on Ti electrode. During water oxidation the surface of the $Co(OH)_2$ electrochemically oxidizes to CoOOH.

Paper II expands on the deposition from Paper I, giving conditions for epitaxial growth of $Co(OH)_2$ on the low index planes of Au(111), Au(100), and Au(110). Epitaxial films grow in the [0001] out-of-plane direction with a cone-like morphology, having little strain. Epitaxial films are converted thermally to epitaxial Co_3O_4 and electrochemically to epitaxial CoOOH. Conversion results in large cracks and pores in the films due to the large volume reduction per Co atom, yet the microcone morphology and epitaxy is retained. Using the methods shown in Paper II, epitaxial Co containing catalysts having high surface areas are obtained.

Paper III presents a two potential step electrochemical method for deposition of epitaxial Cu(100) on Si(100). This represents only the second metal every to be directly electrodeposited epitaxially on Si. Electrodeposited Cu films have similar characteristics as compared to epitaxial Cu films deposited via vacuum techniques, both in epitaxial relationship showing a 45° in-plane rotation, and in mosaic spread. During growth an amorphous SiO_x layer forms which is exploited to produce single-crystal-like foils of Cu, by chemically etching the SiO_x away using 5% HF. Cu single-crystal-like foils are flexible and conductive. The Cu single-crystal-like foils have great potential as an ordered substrate for flexible electronics.

REFERENCES

1.   Bodsworth, C., *The Extraction and Refining of Metals*. Routledge: New York, 1994; p 368.

2.   Bednorz, J. G.; Müller, K. A., Possible highT_c superconductivity in the Ba−La−Cu−O system. *Z. Phys. B: Condens. Matter* **1986,** *64* (2), 189-193.

3.   Ganesh, I.; Bhattacharjee, S.; Saha, B. P.; Johnson, R.; Mahajan, Y. R., A new sintering aid for magnesium aluminate spinel. *Ceram. Int.* **2001,** *27* (7), 773-779.

4.   *Intermetallic and Ceramic Coatings*. Marcel Dekker, Inc.: New York, NY, 1999.

5.   Moats, M.; Free, M., A Bright Future for copper electrowinning. *JOM* **2007,** *59* (10), 34-36.

6.   Schlesinger, M. E.; King, M. J.; Sole, K. C.; Davenport, W. G., Chapter 17 - Electrowinning. In *Extractive Metallurgy of Copper (Fifth Edition)*, Schlesinger, M. E.; King, M. J.; Sole, K. C.; Davenport, W. G., Eds. Elsevier: Oxford, 2011; pp 349-372.

7.   Das, T. N., Saturation Concentration of Dissolved O_2 in Highly Acidic Aqueous Solutions of H_2SO_4. *Ind. Eng. Chem. Res.* **2005,** *44* (6), 1660-1664.

8.   Kazusuke, Y., Anodically Electrodeposited Iridium Oxide Films (AEIROF) from Alkaline Solutions for Electrochromic Display Devices. *Jpn. J. Appl. Phys.* **1989,** *28* (4R), 632.

9.   Petit, M. A.; Plichon, V., Anodic electrodeposition of iridium oxide films. *J. Electroanal. Chem.* **1998,** *444* (2), 247-252.

10.   Gancy, A. B., Electrodeposition of Lead Dioxide from Alkaline Solution. *J. Electrochem. Soc.* **1969,** *116* (11), 1496-1499.

11.   Hull, C. M.; Koza, J. A.; Switzer, J. A., Electrodeposition of epitaxial $Co(OH)_2$ on gold and conversion to epitaxial CoOOH and Co_3O_4. *J. Mater. Res.* **2016,** *31* (21), 3324-3331.

12.   Skyllas Kazacos, M.; Miller, B., Electrodeposition of CdSe Films from Selenosulfite Solution. *J. Electrochem. Soc.* **1980,** *127* (11), 2378-2381.

13.   Gal-Or, L.; Silberman, I.; Chaim, R., Electrolytic ZrO_2 Coatings: I. Electrochemical Aspects. *J. Electrochem. Soc.* **1991,** *138* (7), 1939-1942.

14.   Izaki, M.; Omi, T., Electrolyte Optimization for Cathodic Growth of Zinc Oxide Films. *J. Electrochem. Soc.* **1996,** *143* (3), L53-L55.

15.   Kang, D.; Lee, D.; Choi, K.-S., Electrochemical Synthesis of Highly Oriented, Transparent, and Pinhole-Free ZnO and Al-Doped ZnO Films and Their Use in Heterojunction Solar Cells. *Langmuir* **2016,** *32* (41), 10459-10466.

16.   Indira, L.; Kamath, P. V., Electrogeneration of base by cathodic reduction of anions: novel one-step route to unary and layered double hydroxides (LDHs). *J. Mater. Chem.* **1994,** *4* (9), 1487-1490.

17.   Zhitomirsky, I., Cathodic electrosynthesis of titania films and powders. *Nanostruct. Mater.* **1997,** *8* (4), 521-528.

18.   Zhou, Y.; Phillips, R. J.; Switzer, J. A., Electrochemical Synthesis and Sintering of Nanocrystalline Cerium(IV) Oxide Powders. *J. Am. Ceram. Soc.* **1995,** *78* (4), 981-985.

19.   Zhitomirsky, I.; Petric, A., Electrolytic and electrophoretic deposition of CeO_2 films. *Mater. Lett.* **1999,** *40* (6), 263-268.

20.   Park, B.-O.; Lokhande, C. D.; Park, H.-S.; Jung, K.-D.; Joo, O.-S., Cathodic electrodeposition of RuO_2 thin films from $Ru(III)Cl_3$ solution. *Mater. Chem. Phys.* **2004,** *87* (1), 59-66.

21.   Lee, G. R.; Crayston, J. A., Studies on the electrochemical deposition of niobium oxide. *J. Mater. Chem.* **1996,** *6* (2), 187-192.

22.   Zhitomirsky, I.; Gal-Or, L., Ruthenium oxide deposits prepared by cathodic electrosynthesis. *Mater. Lett.* **1997,** *31* (1), 155-159.

23.   Bi, J.; Gao, Q.; Ao, J.; Zhang, Z.; Sun, G.; Zhang, Y.; Liu, W.; Liu, F.; Sun, Y.; Xiang, D., Influence of Cu on Ga diffusion during post-selenizing the electrodeposited Cu/In/Ga metallic precursor process. *Sol. Energy Mater. Sol. Cells* **2018,** *182*, 92-97.

24.   Shao, P.-W.; Li, C.-T.; Ho, K.-C.; Cheng, K.-W., Catalytic and photoelectrochemical performances of Cu–Zn–Sn–Se thin films prepared using selenization of electrodeposited Cu–Zn–Sn metal precursors. *J. Power Sources* **2015,** *286*, 47-57.

25.   Yao, L.; Ao, J.; Jeng, M.-J.; Bi, J.; Gao, S.; Sun, G.; He, Q.; Zhou, Z.; Sun, Y.; Chang, L.-B., A CZTSe solar cell with 8.2% power conversion efficiency fabricated using electrodeposited Cu/Sn/Zn precursor and a three-step selenization process at low Se pressure. *Sol. Energy Mater. Sol. Cells* **2017,** *159*, 318-324.

26.   Hill, J. C.; Koza, J. A.; Switzer, J. A., Electrodeposition of Epitaxial Lead Iodide and Conversion to Textured Methylammonium Lead Iodide Perovskite. *ACS Appl. Mater. Interfaces* **2015,** *7* (47), 26012-26016.

27.   Siripala, W.; Jayakody, J. R. P., Observation of n-type photoconductivity in electrodeposited copper oxide film electrodes in a photoelectrochemical cell. *Sol. Energy Mater.* **1986,** *14* (1), 23-27.

28.   Garuthara, R.; Siripala, W., Photoluminescence characterization of polycrystalline n-type Cu2O films. *J. Lumin.* **2006,** *121* (1), 173-178.

29.   Wang, L.; Tao, M., Fabrication and Characterization of p-n Homojunctions in Cuprous Oxide by Electrochemical Deposition. *Electrochem. Solid-State Lett.* **2007,** *10* (9), H248-H250.

30.   Scanlon, D. O.; Watson, G. W., Undoped n-Type Cu_2O: Fact or Fiction? *J. Phys. Chem. Lett.* **2010,** *1* (17), 2582-2585.

31.   Thomas, M. A.; Cui, J. B., Electrochemical Route to p-Type Doping of ZnO Nanowires. *J. Phys. Chem. Lett.* **2010,** *1* (7), 1090-1094.

32.   Ghahramanifard, F.; Rouhollahi, A.; Fazlolahzadeh, O., Electrodeposition of Cu-doped p-type ZnO nanorods; effect of Cu doping on structural, optical and photoelectrocatalytic property of ZnO nanostructure. *Superlattices Microstruct.* **2018,** *114*, 1-14.

33.   Duffy, N. W.; Lane, D.; Özsan, M. E.; Peter, L. M.; Rogers, K. D.; Wang, R. L., Structural and spectroscopic studies of CdS/CdTe heterojunction cells fabricated by electrodeposition. *Thin Solid Films* **2000,** *361-362*, 314-320.

34.   Han, K.; Tao, M., N-Type Doping in Electrodeposited Cu_2O by Cu Diffusion. *ECS Trans.* **2010,** *25* (15), 103-109.

35.   Jong Duk, L.; Chang Young, P.; Hyeon Soo, K.; Jeoung Ju, L.; Yeon-Gyu, C., A study of conduction of ZnO film/p-Si heterojunction fabricated by photoinduced electrodeposition under illumination. *J. Phys. D: Appl. Phys.* **2010,** *43* (36), 365403.

36.   Kathalingam, A.; Kim, H.-S., Annealing induced p-type conversion and substrate dependent effect of n-ZnO/p-Si heterostructure. *Mater. Lett.* **2017,** *196*, 30-32.

37.   Rodzi, S. Z. F.; Mohd, Y., Synthesis of NiO Electrochromic Films via Two-Step Method. *Adv. Mater. Res.* **2014,** *894*, 381-385.

38. Uplane, M. M.; Mujawar, S. H.; Inamdar, A. I.; Shinde, P. S.; Sonavane, A. C.; Patil, P. S., Structural, optical and electrochromic properties of nickel oxide thin films grown from electrodeposited nickel sulphide. *Appl. Surf. Sci.* **2007,** *253* (24), 9365-9371.

39. Kim, J. Y.; Choi, J.; Kim, H. Y.; Hwang, E.; Kim, H.-J.; Ahn, S. H.; Kim, S.-K., Activity and stability of the oxygen evolution reaction on electrodeposited Ru and its thermal oxides. *Appl. Surf. Sci.* **2015,** *359*, 227-235.

40. Zeng, Q.; Bai, J.; Li, J.; Xia, L.; Huang, K.; Li, X.; Zhou, B., A novel in situ preparation method for nanostructured α-Fe$_2$O$_3$ films from electrodeposited Fe films for efficient photoelectrocatalytic water splitting and the degradation of organic pollutants. *J. Mater. Chem. A* **2015,** *3* (8), 4345-4353.

41. Zhou, F.; Izgorodin, A.; Hocking, R. K.; Armel, V.; Spiccia, L.; MacFarlane, D. R., Improvement of Catalytic Water Oxidation on MnO$_x$ Films by Heat Treatment. *ChemSusChem* **2013,** *6* (4), 643-651.

42. Zong, B.; Wu, Y.; Han, G.; Yang, B.; Luo, P.; Wang, L.; Qiu, J.; Li, K., Synthesis of Iron Oxide Nanostructures by Annealing Electrodeposited Fe-Based Films. *Chem. Mater.* **2005,** *17* (6), 1515-1520.

43. Andrukaitis, E., Lithium intercalation in electrodeposited vanadium oxide bronzes. *J. Power Sources* **2003,** *119-121*, 205-210.

44. Chemelewski, W. D.; Lee, H.-C.; Lin, J.-F.; Bard, A. J.; Mullins, C. B., Amorphous FeOOH Oxygen Evolution Reaction Catalyst for Photoelectrochemical Water Splitting. *J. Am. Chem. Soc.* **2014,** *136* (7), 2843-2850.

45. Wu, Y.; Chen, M.; Han, Y.; Luo, H.; Su, X.; Zhang, M.-T.; Lin, X.; Sun, J.; Wang, L.; Deng, L.; Zhang, W.; Cao, R., Fast and Simple Preparation of Iron-Based Thin Films as Highly Efficient Water-Oxidation Catalysts in Neutral Aqueous Solution. *Angew. Chem., Int. Ed.* **2015,** *54* (16), 4870-4875.

46. Zou, S.; Burke, M. S.; Kast, M. G.; Fan, J.; Danilovic, N.; Boettcher, S. W., Fe (Oxy)hydroxide Oxygen Evolution Reaction Electrocatalysis: Intrinsic Activity and the Roles of Electrical Conductivity, Substrate, and Dissolution. *Chem. Mater.* **2015,** *27* (23), 8011-8020.

47. Martinez, L.; Leinen, D.; Martín, F.; Gabas, M.; Ramos-Barrado, J. R.; Quagliata, E.; Dalchiele, E. A., Electrochemical Growth of Diverse Iron Oxide (Fe$_3$O$_4$, α-FeOOH , and γ-FeOOH) Thin Films by Electrodeposition Potential Tuning. *J. Electrochem. Soc.* **2007,** *154* (3), D126-D133.

48. Corrigan, D. A.; Bendert, R. M., Effect of Coprecipitated Metal Ions on the Electrochemistry of Nickel Hydroxide Thin Films: Cyclic Voltammetry in 1M KOH *J. Electrochem. Soc.* **1989,** *136* (3), 723-728.

49. Kenney, M. J.; Gong, M.; Li, Y.; Wu, J. Z.; Feng, J.; Lanza, M.; Dai, H., High-Performance Silicon Photoanodes Passivated with Ultrathin Nickel Films for Water Oxidation. *Science* **2013,** *342* (6160), 836.

50. Yan, Z.; Sun, H.; Chen, X.; Liu, H.; Zhao, Y.; Li, H.; Xie, W.; Cheng, F.; Chen, J., Anion insertion enhanced electrodeposition of robust metal hydroxide/oxide electrodes for oxygen evolution. *Nat. Commun.* **2018,** *9* (1), 2373.

51. Hill, J. C.; Landers, A. T.; Switzer, J. A., An electrodeposited inhomogeneous metal–insulator–semiconductor junction for efficient photoelectrochemical water oxidation. *Nat. Mater.* **2015,** *14*, 1150.

52. Liu, Y.-C.; Koza, J. A.; Switzer, J. A., Conversion of electrodeposited $Co(OH)_2$ to $CoOOH$ and Co_3O_4, and comparison of their catalytic activity for the oxygen evolution reaction. *Electrochim. Acta* **2014,** *140*, 359-365.

53. Dong, W. J.; Song, Y. J.; Yoon, H.; Jung, G. H.; Kim, K.; Kim, S.; Lee, J.-L., Monolithic Photoassisted Water Splitting Device Using Anodized Ni-Fe Oxygen Evolution Catalytic Substrate. *Adv. Energy Mater.* **2017,** *7* (19), 1700659.

54. Zhang, W.; Wu, Y.; Qi, J.; Chen, M.; Cao, R., A Thin NiFe Hydroxide Film Formed by Stepwise Electrodeposition Strategy with Significantly Improved Catalytic Water Oxidation Efficiency. *Adv. Energy Mater.* **2017,** *7* (9), 1602547.

55. Zhao, Z.; Wu, H.; He, H.; Xu, X.; Jin, Y., A High-Performance Binary Ni–Co Hydroxide-based Water Oxidation Electrode with Three-Dimensional Coaxial Nanotube Array Structure. *Adv. Funct. Mater.* **2014,** *24* (29), 4698-4705.

56. Han, L.; Dong, S.; Wang, E., Transition-Metal (Co, Ni, and Fe)-Based Electrocatalysts for the Water Oxidation Reaction. *Adv. Mater.* **2016,** *28* (42), 9266-9291.

57. Toda, M., Vibration of a Chain with Nonlinear Interaction. *J. Phys. Soc. Jpn.* **1967,** *22* (2), 431-436.

58. One-dimensional dislocations. I. Static theory. *Proc. R. Soc. London, Ser. A* **1949,** *198* (1053), 205.

59. One-dimensional dislocations. II. Misfitting monolayers and oriented overgrowth. *Proc. R. Soc. London, Ser. A* **1949,** *198* (1053), 216.

60. Markov, I.; Stoyanov, S., Mechanisms of epitaxial growth. *Contemp. Phys.* **1987,** *28* (3), 267-320.

61. Chen, L.; Andrea, L.; Timalsina, Y. P.; Wang, G.-C.; Lu, T.-M., Engineering Epitaxial-Nanospiral Metal Films Using Dynamic Oblique Angle Deposition. *Cryst. Growth Des.* **2013,** *13* (5), 2075-2080.

62. Hashim, I.; Park, B.; Atwater, H. A., Epitaxial growth of Cu (001) on Si (001): Mechanisms of orientation development and defect morphology. *Appl. Phys. Lett.* **1993,** *63* (20), 2833-2835.

63. Chang, C. A.; Liu, J. C.; Angilello, J., Epitaxy of (100) Cu on (100) Si by evaporation near room temperatures: In-plane epitaxial relation and channeling analysis. *Appl. Phys. Lett.* **1990,** *57* (21), 2239-2240.

64. Demczyk, B. G.; Naik, R.; Auner, G.; Kota, C.; Rao, U., Growth of Cu films on hydrogen terminated Si(100) and Si(111) surfaces. *J. Appl. Phys.* **1994,** *75* (4), 1956-1961.

65. Meunier, A.; Gilles, B.; Verdier, M., Cu/Si(001) epitaxial growth: role of the epitaxial silicide formation in the structure and the morphology. *J. Cryst. Growth* **2005,** *275* (1), e1059-e1065.

66. Lukaszew, R. A.; Sheng, Y.; Uher, C.; Clarke, R., Smoothening of Cu films grown on Si(001). *Appl. Phys. Lett.* **2000,** *76* (6), 724-726.

67. Jiang, H.; Klemmer, T. J.; Barnard, J. A.; Payzant, E. A., Epitaxial growth of Cu on Si by magnetron sputtering. *J. Vac. Sci. Technol., A* **1998,** *16* (6), 3376-3383.

68. Cemin, F.; Lundin, D.; Furgeaud, C.; Michel, A.; Amiard, G.; Minea, T.; Abadias, G., Epitaxial growth of Cu(001) thin films onto Si(001) using a single-step HiPIMS process. *Sci. Rep.* **2017,** *7* (1), 1655.

69. Myers, T. H.; Lo, Y.; Bicknell, R. N.; Schetzina, J. F., Growth of CdTe films on sapphire by molecular beam epitaxy. *Appl. Phys. Lett.* **1983,** *42* (3), 247-248.

70. Cullen, G. W., The Preparation and Properties of Heteroepitaxial Silicon. In *Heteroepitaxial Semiconductors for Electronic Devices*, Cullen, G. W.; Wang, C. C., Eds. Springer New York: New York, NY, 1978; pp 6-105.

71. Narayan, J.; Larson, B. C., Domain epitaxy: A unified paradigm for thin film growth. *J. Appl. Phys.* **2002,** *93* (1), 278-285.

72. Zheleva, T.; Jagannadham, K.; Narayan, J., Epitaxial growth in large-lattice-mismatch systems. *J. Appl. Phys.* **1994,** *75* (2), 860-871.

73.   Satoru, K.; Kensuke, A.; Takeshi, I.; Manabu, Y.; Masayasu, S.; Yasuo, H.; Hiroshi, F.; Mamoru, Y., Large Lattice Misfit on Epitaxial Thin Film: Coincidence Site Lattice Expanded on Polar Coordinate System. *Jpn. J. Appl. Phys.* **2010,** *49* (8S1), 08JE02.

74.   Yapsir, A. S.; Choi, C. H.; Lu, T. M., Observation of a new Al(111)/Si(111) orientational epitaxy. *J. Appl. Phys.* **1990,** *67* (2), 796-799.

75.   Zur, A.; McGill, T. C., Lattice match: An application to heteroepitaxy. *J. Appl. Phys.* **1984,** *55* (2), 378-386.

76.   Breyfogle, B. E.; Phillips, R. J.; Switzer, J. A., Epitaxial electrodeposition of silver oxide nitrate (Ag(Ag$_3$O$_4$)$_2$NO$_3$) onto highly-oriented conducting metal oxides in the lead-thallium-oxygen system. *Chem. Mater.* **1992,** *4* (6), 1356-1360.

77.   Vertegel, A. A.; Shumsky, M. G.; Switzer, J. A., Epitaxial electrodeposition of thallic oxide on single crystal gold. *Electrochim. Acta* **2000,** *45* (20), 3233-3239.

78.   Bohannan, E. W.; Shumsky, M. G.; Switzer, J. A., Epitaxial Electrodeposition of Copper(I) Oxide on Single-Crystal Gold(100). *Chem. Mater.* **1999,** *11* (9), 2289-2291.

79.   Barton, J. K.; Vertegel, A. A.; Bohannan, E. W.; Switzer, J. A., Epitaxial Electrodeposition of Copper(I) Oxide on Single-Crystal Copper. *Chem. Mater.* **2001,** *13* (3), 952-959.

80.   Switzer, J. A.; Liu, R.; Bohannan, E. W.; Ernst, F., Epitaxial Electrodeposition of a Crystalline Metal Oxide onto Single-Crystalline Silicon. *J. Phys. Chem. B* **2002,** *106* (48), 12369-12372.

81.   Liu, R.; Bohannan, E. W.; Switzer, J. A.; Oba, F.; Ernst, F., Epitaxial electrodeposition of Cu$_2$O films onto InP(001). *Appl. Phys. Lett.* **2003,** *83* (10), 1944-1946.

82.   Vertegel, A. A.; Shumsky, M. G.; Switzer, J. A., Epitaxial Electrodeposition of Lead Sulfide on (100)-Oriented Single-Crystal Gold. *Angew. Chem., Int. Ed.* **1999,** *38* (21), 3169-3171.

83.   Nikiforov, M. P.; Vertegel, A. A.; Shumsky, M. G.; Switzer, J. A., Epitaxial Electrodeposition of Fe$_3$O$_4$ on Single-Crystal Au(111). *Adv. Mater.* **2000,** *12* (18), 1351-1353.

84.   Sorenson, T. A.; Morton, S. A.; Waddill, G. D.; Switzer, J. A., Epitaxial Electrodeposition of Fe$_3$O$_4$ Thin Films on the Low-Index Planes of Gold. *J. Am. Chem. Soc.* **2002,** *124* (25), 7604-7609.

85. Kulp, E. A.; Kothari, H. M.; Limmer, S. J.; Yang, J.; Gudavarthy, R. V.; Bohannan, E. W.; Switzer, J. A., Electrodeposition of Epitaxial Magnetite Films and Ferrihydrite Nanoribbons on Single-Crystal Gold. *Chem. Mater.* **2009,** *21* (21), 5022-5031.

86. Gudavarthy, R. V.; Gorantla, S.; Mu, G.; Kulp, E. A.; Gemming, T.; Eckert, J.; Switzer, J. A., Epitaxial Electrodeposition of Fe_3O_4 on Single-Crystal Ni(111). *Chem. Mater.* **2011,** *23* (8), 2017-2019.

87. Liu, R.; Vertegel, A. A.; Bohannan, E. W.; Sorenson, T. A.; Switzer, J. A., Epitaxial Electrodeposition of Zinc Oxide Nanopillars on Single-Crystal Gold. *Chem. Mater.* **2001,** *13* (2), 508-512.

88. Limmer, S. J.; Kulp, E. A.; Switzer, J. A., Epitaxial Electrodeposition of ZnO on Au(111) from Alkaline Solution: Exploiting Amphoterism in Zn(II). *Langmuir* **2006,** *22* (25), 10535-10539.

89. Mu, G.; Gudavarthy, R. V.; Kulp, E. A.; Switzer, J. A., Tilted Epitaxial ZnO Nanospears on Si(001) by Chemical Bath Deposition. *Chem. Mater.* **2009,** *21* (17), 3960-3964.

90. Vertegel, A. A.; Bohannan, E. W.; Shumsky, M. G.; Switzer, J. A., Epitaxial Electrodeposition of Orthorhombic α PbO₂ on (100)-Oriented Single Crystal Au. *J. Electrochem. Soc.* **2001,** *148* (4), C253-C256.

91. Nakanishi, S.; Lu, G.; Kothari, H. M.; Bohannan, E. W.; Switzer, J. A., Epitaxial Electrodeposition of Prussian Blue Thin Films on Single-Crystal Au(110). *J. Am. Chem. Soc.* **2003,** *125* (49), 14998-14999.

92. Boonsalee, S.; Gudavarthy, R. V.; Bohannan, E. W.; Switzer, J. A., Epitaxial Electrodeposition of Tin(II) Sulfide Nanodisks on Single-Crystal Au(100). *Chem. Mater.* **2008,** *20* (18), 5737-5742.

93. Gudavarthy, R. V.; Burla, N.; Kulp, E. A.; Limmer, S. J.; Sinn, E.; Switzer, J. A., Epitaxial electrodeposition of chiral CuO films from copper(ii) complexes of malic acid on Cu(111) and Cu(110) single crystals. *J. Mater. Chem.* **2011,** *21* (17), 6209-6216.

94. Bohannan, E. W.; Jaynes, C. C.; Shumsky, M. G.; Barton, J. K.; Switzer, J. A., Low-temperature electrodeposition of the high-temperature cubic polymorph of bismuth(III) oxide. *Solid State Ionics* **2000,** *131* (1), 97-107.

95. Switzer, J. A.; Hill, J. C.; Mahenderkar, N. K.; Liu, Y.-C., Nanometer-Thick Gold on Silicon as a Proxy for Single-Crystal Gold for the Electrodeposition of Epitaxial Cuprous Oxide Thin Films. *ACS Appl. Mater. Interfaces* **2016,** *8* (24), 15828-15837.

96.   (NREL), N. R. E. L., Best Research-Cell Efficiencies. pv-efficiencies-07-17-
        2018.pdf, Ed. Golden, CO, 2018.

97.   Chang, C. A., Magnetocrystalline anisotropy of (100) face-centered cubic Co
        structures deposited on Cu/Si(100). *Appl. Phys. Lett.* **1991,** *58* (16), 1745-1747.

98.   Frisk, A.; Ali, H.; Svedlindh, P.; Leifer, K.; Andersson, G.; Nyberg, T.,
        Composition, structure and magnetic properties of ultra-thin Fe/Ni multilayers
        sputter deposited on epitaxial Cu/Si(001). *Thin Solid Films* **2018,** *646*, 117-125.

99.   Castaner, R.; Prieto, C.; Andres, A. d.; Martinez, J. L.; Martinez-Albertos, J. L.;
        Ocal, C.; Miranda, R., The structural characterization of Co-Cu(100) superlattices
        by X-ray absorption spectroscopy. *J. Phys.: Condens. Matter* **1994,** *6* (27), 4981.

100.   Cebollada, A.; Gallego, J. M.; de Miguel, J. J.; Miranda, R.; Martinez, J. L.;
        Ferrer, S.; Fillion, G.; Rebouillat, J. P., Epitaxial growth of metals: from
        monolayer to superlattice. *Vacuum* **1990,** *41* (1), 482-484.

101.   Cebollada, A.; Martnez, J. L.; Gallego, J. M.; de Miguel, J. J.; Miranda, R.;
        Ferrer, S.; Batallán, F.; Fillion, G.; Rebouillat, J. P., Antiferromagnetic ordering
        in Co-Cu single-crystal superlattices. *Phys. Rev. B* **1989,** *39* (13), 9726-9729.

102.   Nabiyouni, G.; Schwarzacher, W., Dependence of GMR on crystal orientation in
        electrodeposited Co–Ni–Cu/Cu superlattices. *J. Magn. Magn. Mater.* **1996,** *156*
        (1), 355-356.

103.   Shima, M.; Salamanca-Riba, L. G.; McMichael, R. D.; Moffat, T. P., Correlation
        Between Structural Imperfection and Giant Magnetoresistance in
        Electrodeposited Co/Cu Multilayers. *J. Electrochem. Soc.* **2001,** *148* (8), C518-
        C523.

104.   He, Z.; Koza, J. A.; Liu, Y.-C.; Chen, Q.; Switzer, J. A., Room-temperature
        electrochemical reduction of epitaxial Bi_2O_3 films to epitaxial Bi films. *RSC Adv.*
        2016, *6* (99), 96832-96836.

105.   Kern, W. P., D. A., Cleaning solutions based on hydrogen peroxide for use in
        silicon semiconductor technology. *RCA Rev.* **1970,** *31*, 187-206.

106.   Allongue, P.; Henry de Villeneuve, C.; Morin, S.; Boukherroub, R.; Wayner, D.
        D. M., The preparation of flat H–Si(111) surfaces in 40% NH_4F revisited.
        Electrochim. Acta **2000,** *45* (28), 4591-4598.

107.   Allongue, P.; Kieling, V.; Gerischer, H., Etching mechanism and atomic structure
        of H–Si(111) surfaces prepared in NH_4F. *Electrochim. Acta* **1995,** *40* (10), 1353-
        1360.

108. Dumas, P.; Chabal, Y. J.; Jakob, P., Morphology of hydrogen-terminated Si(111) and Si(100) surfaces upon etching in HF and buffered-HF solutions. *Surface Science* **1992,** *269-270*, 867-878.

109. Higashi, G. S.; Chabal, Y. J.; Trucks, G. W.; Raghavachari, K., Ideal hydrogen termination of the Si (111) surface. *Appl. Phys. Lett.* **1990,** *56* (7), 656-658.

110. Munford, M. L.; Cortes, R.; Allongue, P., The Preparation of Ideally Ordered Flat H-Si(111) Surfaces. *Sens. Mater.* **2001,** *13* (5), 259-270.

111. Gräf, D.; Grundner, M.; Schulz, R.; Mühlhoff, L., Oxidation of HF-treated Si wafer surfaces in air. *J. Appl. Phys.* **1990,** *68* (10), 5155-5161.

112. Mende, G.; Finster, J.; Flamm, D.; Schulze, D., Oxidation of etched silicon in air at room temperature; Measurements with ultrasoft X-ray photoelectron spectroscopy (ESCA) and neutron activation analysis. *Surface Science* **1983,** *128* (2), 169-175.

113. Houston, M. R.; Maboudian, R., Stability of ammonium fluoride-treated Si(100). *J. Appl. Phys.* **1995,** *78* (6), 3801-3808.

114. Gibson, J. M.; Batstone, J. L.; Tung, R. T., In situ study of the molecular beam epitaxy of $CoSi_2$ on (111) Si by transmission electron microscopy and diffraction. *Appl. Phys. Lett.* **1987,** *51* (1), 45-47.

115. McKee, R. A.; Walker, F. J.; Conner, J. R.; Specht, E. D.; Zelmon, D. E., Molecular beam epitaxy growth of epitaxial barium silicide, barium oxide, and barium titanate on silicon. *Appl. Phys. Lett.* **1991,** *59* (7), 782-784.

116. Nikishin, S. A.; Faleev, N. N.; Antipov, V. G.; Francoeur, S.; Grave de Peralta, L.; Seryogin, G. A.; Temkin, H.; Prokofyeva, T. I.; Holtz, M.; Chu, S. N. G., High quality GaN grown on Si(111) by gas source molecular beam epitaxy with ammonia. *Appl. Phys. Lett.* **1999,** *75* (14), 2073-2075.

117. Stevens, K. S.; Ohtani, A.; Kinniburgh, M.; Beresford, R., Microstructure of AlN on Si (111) grown by plasma-assisted molecular beam epitaxy. *Appl. Phys. Lett.* **1994,** *65* (3), 321-323.

118. Lei, T.; Fanciulli, M.; Molnar, R. J.; Moustakas, T. D.; Graham, R. J.; Scanlon, J., Epitaxial growth of zinc blende and wurtzitic gallium nitride thin films on (001) silicon. *Appl. Phys. Lett.* **1991,** *59* (8), 944-946.

119. Takahashi, N.; Huminiuc, T.; Yamamoto, Y.; Yanase, T.; Shimada, T.; Hirohata, A.; Nagahama, T., Fabrication of Epitaxial Fe_3O_4 Film on a Si(111) Substrate. *Sci. Rep.* **2017,** *7* (1), 7009.

120. Song, N.; Young, M.; Liu, F.; Erslev, P.; Wilson, S.; Harvey, S. P.; Teeter, G.; Huang, Y.; Hao, X.; Green, M. A., Epitaxial Cu_2ZnSnS_4 thin film on Si (111) 4° substrate. *Appl. Phys. Lett.* **2015,** *106* (25), 252102.

121. Park, K. H.; Smith, G. A.; Rajan, K.; Wang, G. C., Interface characterization of epitaxial Ag Films on Si(100) and Si(111) grown by molecular beam epitaxy. *Metall. Trans. A* **1990,** *21* (9), 2323-2332.

122. McClean, I. P.; Spink, D. M.; Thomas, C. B.; Tsakonas, K., Low temperature epitaxial deposition of ZnS onto (100) Si by RF magnetron sputtering and molecular beam epitaxy. *J. Cryst. Growth* **1994,** *143* (3), 172-175.

123. Lo, Y.; Bicknell, R. N.; Myers, T. H.; Schetzina, J. F.; Stadelmaier, H. H., Growth of CdTe films on silicon by molecular beam epitaxy. *J. Appl. Phys.* **1983,** *54* (7), 4238-4240.

124. Mante, N.; Rennesson, S.; Frayssinet, E.; Largeau, L.; Semond, F.; Rouvière, J. L.; Feuillet, G.; Vennéguès, P., Proposition of a model elucidating the AlN-on-Si (111) microstructure. *J. Appl. Phys.* **2018,** *123* (21), 215701.

125. Kukushkin, S. A.; Mizerov, A. M.; Osipov, A. V.; Redkov, A. V.; Timoshnev, S. N., Plasma assisted molecular beam epitaxy of thin GaN films on Si(111) and SiC/Si(111) substrates: Effect of SiC and polarity issues. *Thin Solid Films* **2018,** *646*, 158-162.

126. Hiroyuki, M.; Hiroshi, I., Epitaxial Growth of $SrTiO_3$ Films on Si(100) Substrates Using a Focused Electron Beam Evaporation Method. *Jpn. J. Appl. Phys.* **1991,** *30* (8A), L1415.

127. Wu, H. Z.; He, K. M.; Qiu, D. J.; Huang, D. M., Low-temperature epitaxy of ZnO films on Si(001) and silica by reactive e-beam evaporation. *J. Cryst. Growth* **2000,** *217* (1), 131-137.

128. Shi, J.; Irie, T.; Takahashi, F.; Hashimoto, M., Growth of $CoSi_2$ films on Si (100) substrates by a two-step method. *Thin Solid Films* **2000,** *375* (1), 37-41.

129. Mattoso, N.; Mosca, D. H.; Mazzaro, I.; Teixeira, S. R.; Schreiner, W. H., The epitaxial growth of evaporated Cu/CaF_2 bilayers on Si(111). *J. Appl. Phys.* **1995,** *77* (6), 2831-2833.

130. Shin, B.; Zhu, Y.; Gershon, T.; Bojarczuk, N. A.; Guha, S., Epitaxial growth of kesterite Cu_2ZnSnS_4 on a Si(001) substrate by thermal co-evaporation. *Thin Solid Films* **2014,** *556*, 9-12.

131.   Tompa, G. S.; Li, Y. B.; Agassi, D.; Kim, S. I.; Hong, S. K., Mg$_2$Si buffer layers on Si(100) prepared by a simple evaporation method. *J. Electron. Mater.* **1996,** *25* (6), 925-929.

132.   Sosnowski, M.; Ramac, S.; Brown, W. L.; Kim, Y. O., Importance of steps in heteroepitaxy: The case of aluminum on silicon. *Appl. Phys. Lett.* **1994,** *65* (23), 2943-2945.

133.   Yang, H.; Wang, W.; Liu, Z.; Yang, W.; Li, G., Epitaxial growth mechanism of pulsed laser deposited AlN films on Si (111) substrates. *CrystEngComm* **2014,** *16* (15), 3148-3154.

134.   Tsang, W. S.; Mak, C. L.; Wong, K. H., Epitaxial lithium fluoride films grown by pulsed laser deposition. *Appl. Phys. A* **2003,** *77* (5), 693-696.

135.   Diaz-Fernandez, D.; Spreitzer, M.; Parkelj, T.; Suvorov, D., Multi-stage pulsed laser deposition of high quality epitaxial ultra-thin SrTiO$_3$ on Si substrates. *Appl. Surf. Sci.* **2018,** *455*, 227-235.

136.   Wakiya, N.; Azuma, T.; Shinozaki, K.; Mizutani, N., Low-temperature epitaxial growth of conductive LaNiO$_3$ thin films by RF magnetron sputtering. *Thin Solid Films* **2002,** *410* (1), 114-120.

137.   Yoshitake, T.; Inokuchi, Y.; Yuri, A.; Nagayama, K., Direct epitaxial growth of semiconducting β-FeSi$_2$ thin films on Si(111) by facing targets direct-current sputtering. *Appl. Phys. Lett.* **2006,** *88* (18), 182104.

138.   Yoshitake, T.; Nakagauchi, D.; Ogawa, T.; Itakura, M.; Kuwano, N.; Tomokiyo, Y.; Kajiwara, T.; Nagayama, K., Room-temperature epitaxial growth of ferromagnetic Fe$_3$Si films on Si(111) by facing target direct-current sputtering. *Appl. Phys. Lett.* **2005,** *86* (26), 262505.

139.   Gräf, D.; Grundner, M.; Schulz, R., Reaction of water with hydrofluoric acid treated silicon(111) and (100) surfaces. *J. Vac. Sci. Technol., A* **1989,** *7* (3), 808-813.

140.   Yang, S. K.; Peter, S.; Takoudis, C. G., Fundamentals of two-step etching techniques for ideal silicon-hydrogen termination of silicon(111). *J. Appl. Phys.* **1994,** *76* (7), 4107-4112.

141.   Prod'homme, P.; Maroun, F.; Cortès, R.; Allongue, P., Electrochemical growth of ultraflat Au(111) epitaxial buffer layers on H–Si(111). *Appl. Phys. Lett.* **2008,** *93* (17), 171901.

142. Prodhomme, P.; Warren, S.; Cortès, R.; Jurca, H. F.; Maroun, F.; Allongue, P., Epitaxial Growth of Gold on H–Si(111): The Determining Role of Hydrogen Evolution. *ChemPhysChem* **2010,** *11* (13), 2992-3001.

143. Ernst, F.; Switzer, J. A., Microstructure of Cu_2O/Si Interfaces, Made by Epitaxial Electrodeposition. *Z. Metallkd.* **2003,** *94* (3), 259-265.

144. Oba, F.; Liu, R.; Yu, Y.; Bohannan, E. W.; Ernst, F.; Switzer, J., TEM Studies of Cu_2O-Si and Cu_2O-InP Interfaces Made by Epitaxial Electrodeposition. *Microsc. Microanal.* **2004,** *10* (S02), 292-293.

145. Goyal, A. K., TN), Budai, John D. (Oak Ridge, TN), Kroeger, Donald M. (Knoxville, TN), Norton, David P. (Knoxville, TN), Specht, Eliot D. (Knoxville, TN), Christen, David K. (Oak Ridge, TN) Structures having enhanced biaxial texture and method of fabricating same. 5741377, 1998.

146. Paranthaman, M.; Goyal, A.; List, F. A.; Specht, E. D.; Lee, D. F.; Martin, P. M.; He, Q.; Christen, D. K.; Norton, D. P.; Budai, J. D.; Kroeger, D. M., Growth of biaxially textured buffer layers on rolled-Ni substrates by electron beam evaporation. *Phys. C (Amsterdam, Neth.)* **1997,** *275* (3), 266-272.

147. Goyal, A.; Norton, D. P.; Paranthaman, M.; Specht, E. D.; He, Q.; List, F. A.; Kroeger, D. M.; Christen, D. K.; Budai, J. D., Low cost, single crystal-like substrates for practical, high efficiency solar cells. *AIP Conf. Proc.* **1997,** *404* (1), 377-394.

148. Shin, J. W.; Standley, A.; Chason, E., Epitaxial electrodeposition of freestanding large area single crystal substrates. *Appl. Phys. Lett.* **2007,** *90* (26), 261909.

149. Mahenderkar, N. K.; Chen, Q.; Liu, Y.-C.; Duchild, A. R.; Hofheins, S.; Chason, E.; Switzer, J. A., Epitaxial lift-off of electrodeposited single-crystal gold foils for flexible electronics. *Science* **2017,** *355* (6330), 1203.

VITA

Caleb Michael Hull was born on November 7, 1990 in St. Charles, MO 63301. He received his Bachelor's of Science in Chemistry with a Minor in Explosives Engineering from Missouri University of Science and Technology in May 2013. Caleb joined Dr. Switzer's research group at Missouri University of Science and Technology as a PhD candidate in June of 2013. Between 2013 and 2018 Caleb was a Chancellor's Fellow at the Missouri University of Science and Technology. His research has focused on the use of electrodeposition to produce epitaxial thin films of metals and metal oxides towards higher efficiency photovoltaics, catalysis, and electronics. He received his PhD in Chemistry from Missouri University of Science and Technology in December 2018.